

Utah State University

DigitalCommons@USU

All Graduate Theses and Dissertations

Graduate Studies

5-2013

Fault Seal Analysis for CO₂ Storage: Fault Zone Architecture, Fault Permeability, and Fluid Migration Pathways in Exposed Analogs in Southeastern Utah

David J. Richey

Follow this and additional works at: <https://digitalcommons.usu.edu/etd>



Part of the [Geology Commons](#)

Recommended Citation

Richey, David J., "Fault Seal Analysis for CO₂ Storage: Fault Zone Architecture, Fault Permeability, and Fluid Migration Pathways in Exposed Analogs in Southeastern Utah" (2013). *All Graduate Theses and Dissertations*. 6060.

<https://digitalcommons.usu.edu/etd/6060>

This Thesis is brought to you for free and open access by the Graduate Studies at DigitalCommons@USU. It has been accepted for inclusion in All Graduate Theses and Dissertations by an authorized administrator of DigitalCommons@USU. For more information, please contact digitalcommons@usu.edu.



FAULT SEAL ANALYSIS FOR CO₂ STORAGE: FAULT ZONE ARCHITECTURE,
FAULT PERMEABILITY, AND FLUID MIGRATION PATHWAYS IN EXPOSED
ANALOGS IN SOUTHEASTERN UTAH

by

David J. Richey

A thesis submitted in partial fulfillment
of the requirement for the degree

of

MASTER OF SCIENCE

in

Geology

Approved:

Dr. James P. Evans
Major Professor

Dr. Alvar Braathen
Committee Member

Dr. Susanne U. Janecke
Committee Member

Dr. Mark R. McLellan
Vice President for Research and
Dean of the School of Graduate Studies

UTAH STATE UNIVERSITY
Logan, Utah

2013

Copyright © David J. Richey 2013

All Rights Reserved

ABSTRACT

Fault Seal Analysis for CO₂ Storage: Fault Zone Architecture, Fault Permeability, and
Fluid Migration Pathways in Exposed Analogs in Southeastern Utah

by

David J. Richey, Master of Science

Utah State University, 2013

Major Professor: Dr. James P. Evans
Department: Geology

Geologic storage of anthropogenic carbon dioxide (CO₂) by injection into underground porous sandstone reservoirs has been proposed as a method for the reduction of anthropogenic greenhouse gas emissions. Upwards migration and leakage of injected fluids along natural fault and fracture networks is a key risk factor for potential injection locations. We examine exposed natural analogs to evaluate the impacts of faulting and fracturing on reservoir and top-seal pairs and to evaluate evidence for paleo-migration of fluids along the fault zone.

We examine the Iron Wash fault, a 25-km long normal fault which cuts Jurassic sedimentary rocks and has throws that range from 20-120 m, to examine how a fault may affect seal integrity. Field mapping, kinematic analysis, petrographic analysis, characterization of the fault zone facies and fault architecture, analysis of altered and mineralized rocks in and around the fault zone, and modeling of fault seal capacity was

conducted to provide an understanding of the Iron Wash fault zone. Field data and observations were combined with well log and borehole data to produce three types of models for the Iron Wash fault: 1) geometric model of the fault in the subsurface, 2) predictive models of fault zone behavior and fault seal analysis, and 3) predictive geomechanical models of the response of the fault zone to an imposed stress field and increasing the effective stress on the fault.

We conclude that the Iron Wash fault zone has low sealing capacity and will likely not behave as a seal for fluids against the fault zone due primarily to modest throw on the fault and high frequency of fractures associated with the fault zone. Analysis of fluid alteration and mineralization around the fault zone indicates that the fault zone was conduit for paleo-fluids. We conclude that the fault is not likely to develop a sealing membrane and therefore will most likely fail as a seal to fluids moving through the reservoirs modeled here. Modeling results indicate that a reduction in the effective normal stress on fault surfaces may induce failure of faults resulting in earthquakes or increased hydraulic conductivity of fractures.

PUBLIC ABSTRACT

Fault Seal Analysis for CO₂ Storage: Fault Zone Architecture, Fault Permeability, and
Fluid Migration Pathways in Exposed Analogs in Southeastern Utah

by

David J. Richey, Master of Science

Utah State University, 2013

Major Professor: Dr. James P. Evans
Department: Geology

Anthropogenic carbon dioxide (CO₂) primarily resulting from the combustion of fossil fuels can be captured and stored by injection into underground porous sandstone reservoirs. This process has been proposed as a method for reducing greenhouse gas emissions that contribute to global warming. Two of the major risks associated with this technology include: 1) upwards migration and leakage of injected fluids along natural fault and fracture networks, and 2) possible induced seismicity (earthquakes) resulting from increasing the pressure in reservoirs and along existing faults.

We use geologic field mapping, petrographic analysis, characterization of the fault zone, analysis of altered and mineralized rocks in and around the fault zone, and computer-based modeling to better understand of the Iron Wash fault zone. We use studies of exposed natural analogs of subsurface geology to evaluate the impacts of faulting and fracturing on reservoir and top-seals. We examine the Iron Wash fault, a 25-

km long normal fault which cuts Jurassic sedimentary rocks and has throws that range from 20-120 m, to examine how a fault may affect seal integrity. We incorporate field data and observations with subsurface data derived from oil and gas exploration boreholes to produce three types of models for the Iron Wash fault: 1) geometric model of the fault in the subsurface, 2) predictive models of fault zone behavior and fault seal analysis, and 3) predictive models of the response of the fault zone to an imposed stress field and increasing reservoir pressures.

We conclude that the Iron Wash fault zone has low sealing capacity and would likely fail to behave as a lateral barrier to fluid flow. Analysis of fluid alteration and mineralization around the fault zone indicates that the fault zone was conduit for paleo-fluids. Modeling results indicate that increases in reservoir pressure against the Iron Wash fault in the current stress field could potentially result in the failure of the fault resulting in earthquakes or increased hydraulic conductivity of fractures. It is impossible to predict the magnitude of potentially induced earthquakes or how much fluid may leak along faults that have failed, but this study provides insight into the potential risks associated with injection of large volumes of fluid into the subsurface.

ACKNOWLEDGMENTS

This thesis was funded by the following sources: U.S. Department of Energy, Grant # DE-FC26-0xNT4FE0001786 awarded to Dr. James P. Evans, ExxonMobil Geoscience Recruiting Grant, American Association of Petroleum Geologists Duncan A. McNaughton Memorial Grant, and numerous grants from Utah State University.

Data from drilling in central and southeastern Utah were provided by the Utah Division of Oil, Gas, and Mining. Geologic maps used in this study were provided by the Utah Geological Survey. Shapefiles used for the development and modification of geologic maps in this study were provided by the Utah Automated Geographic Reference Center and the Utah Geological Survey.

I would like to thank my graduate advisor, Dr. James P. Evans, for his guidance, support, and friendship throughout my time at Utah State University. I would also like to thank my committee members, Dr. Susanne U. Janecke and Dr. Alvar Braathen for their support and contributions to my work. Additional thanks goes to the Department of Geology at Utah State University and all they have done for me and the many opportunities I was given in my time here. I would like to thank my many colleagues that have helped, guided and provided adequate distraction when needed along the way, including Elizabeth Petrie, Mitch Prante, Ryan Sonntag, Kelly Bradbury, Santiago Flores, Corey Barton, Dawn Hayes, Robin Nagy, Xiaofei Ma, and David Parslow.

Finally, none of this could have been possible without the love and support of my family, friends, and my wife, Shaun, who along with our dog Forest were the best field assistants that anyone could ask for.

DISCLAIMER

This report was prepared as an account of work sponsored by an agency of the United States Government. Neither the United States Government nor any agency thereof, nor any of their employees, makes any warranty, express or implied, or assumes any legal liability or responsibility for the accuracy, completeness, or usefulness of any information, apparatus, product, or process disclosed, or represents that its use would not infringe privately owned rights. Reference herein to any specific commercial product, process, or service by trade name, trademark, manufacturer, or otherwise does not necessarily constitute or imply its endorsement, recommendation, or favoring by the United States Government or any agency thereof. The views and opinions of authors expressed herein do not necessarily state or reflect those of the United States Government or any agency thereof.

All flaws and mistakes made in this thesis are my own, but for better or worse, I enjoyed making them.

CONTENTS

ABSTRACT	iii
PUBLIC ABSTRACT	v
ACKNOWLEDGMENTS	vii
DISCLAIMER	viii
LIST OF FIGURES	xi
INTRODUCTION	1
Motivation	6
Objectives	9
Geologic and Structural Setting	14
Iron Wash Fault	21
Terminology and Definitions	25
Characterization of Fault Zones	30
METHODS	31
Field Mapping	32
Structural Petrology	35
X-Ray Diffraction Analysis	36
Subsurface Modeling	36
Geophysical Surveys	37
RESULTS	38
Overview	38
Strain Distribution	44
Fault Throw	47
Fault Zone Thickness	51
Relay Zone and Fault Lens Structure	55
General Structure	55
Strain Distribution	58
Fracture Distribution	60
Fault-related Folding	63
Fault Zone Architecture	66
Evidence for Fluid Migration	69
X-Ray Diffraction Analysis of Fault-Related Rocks	77

Petrographic Analysis of Fault Rocks 80

ANALYSIS 89

 Fault Zone Behavior and Geomechanical Modeling 89

 Model Inputs and Design 90

 Subsurface Contouring 91

 Fault Permeability Modeling 98

 Geomechanical Models 111

DISCUSSION 116

 Fault Architecture, Facies and Damage Zone 117

 Strain Analysis 125

 Implications for CO₂ Injection 126

CONCLUSIONS 132

 Recommendations 136

REFERENCES 138

APPENDICES 154

 Appendix A: Borehole Data 155

 Appendix B: Geophysical Data 157

LIST OF FIGURES

Figure		Page
1	Overview of proposed CO ₂ stabilization wedges.	2
2	Schematic overview of geological storage types used in geologic sequestration of CO ₂	3
3	Schematic overview of potential escape mechanisms of geologically sequestered CO ₂ out of injection reservoirs.....	4
4	Location map and annual CO ₂ emissions of power plants in the Four Corners region	6
5	Geologic map of the San Rafael Swell and San Rafael Desert areas with a box showing the Iron Wash fault study area.....	10
6	Annotated aerial photo of the Iron Wash fault with boxes showing locations of detailed maps of the Iron Wash fault zone.....	15
7	Generalized stratigraphic column for Jurassic and Triassic rocks in San Rafael Desert	16
8	Burial history, thermal model and key geologic events of the area near the town of Green River, Utah.....	19
9	Schematic model of extensional fault geometry.....	26
10	Schematic of structures associated with fault linkage and development.....	27
11	Geologic map of the Iron Wash fault zone (Area A) at the intersection of the San Rafael monocline	40
12	Geologic map of the Iron Wash fault zone (Area B) showing hard- and soft-linked relay zones	41
13	Geologic map of the Iron Wash fault zone (Area C) showing hard-linked relay and fault lenses.....	42
14	Geologic map of the Iron Wash fault zone (Area D) showing the eastern tip of the fault.....	43

15	Equal-area, lower hemisphere stereonet projections of faults in the western section of the study area (Area A)	45
16	Equal-area, lower hemisphere stereonet projections of planes, poles to planes and lineations of the Iron Wash fault zone.....	46
17	Fault throw profile of the Iron Wash fault zone	48
18	Fault throw and thickness profiles for the Iron Wash fault zone.....	49
19	Plot of fault thickness and displacement for the Iron Wash fault zone..	53
20	Fracture density scanlines in hanging wall and footwall damage zones of the Iron Wash fault zone.....	54
21	Annotated field photos of the fault core of the Iron Wash fault zone.....	57
22	Summary of data and interpretation of small-throw fault (~4 m throw) adjacent to the main slip surface of the Iron Wash fault zone	59
23	Summary of soft-linked relay zone (Area B).....	61
24	Summary of hard-linked relay zone (Area B).....	62
25	Equal-area, lower hemisphere stereonet projections with Kamb contour of poles to planes of fractures in the Iron Wash fault zone	63
26	Annotated field photo and schematic cross-section of fault-related fold illustrating displacement accommodated by the flexure of bedding (Area D).	65
27	Annotated field photo and schematic cross-section of fault-related fold illustrating displacement accommodated by the flexure of bedding (Area B).....	66
28	Annotated field photos of expressions of the fault core and damage zone.....	68
29	Annotated field photos of expressions of the architecture of the fault zone.....	70
30	Multiple schematic cross-sections designed to illustrate fault architecture along strike.....	71
31	Annotated field photo of large fault blocks within the fault core adjacent to fault related monocline.....	72
32	Annotated field photos of evidence for fluid migration within the fault zone.....	74

33	Rose diagrams showing strike of fractures with different morphologies along the Iron Wash fault	75
34	Annotated field photos of examples of evidence for fluid migration within the fault zone in Area C within a fault lens	76
35	X-Ray diffraction analysis for host rocks and fault-related rocks	78
36	X-Ray diffraction analysis for a sample transect across a fault gouge zone	79
37	Photomicrographs of deformation structures in the Iron Wash fault zone	81
38	Photomicrographs of mineralization in the Iron Wash fault zone.....	84
39	Photomicrographs of fracture mineralization in the Iron Wash fault zone.....	85
40	Photomicrographs of calcite growth and mineralization in fractures in the Iron Wash fault zone.....	86
41	Photomicrographs of oil-stained and mineralized deformation bands in the Iron Wash fault zone.....	88
42	Photomicrographs of mineralized fractures and fracture margins in Iron Wash fault zone.....	89
43	Generalized type log for the San Rafael Desert from exploration drill-hole API# 43-015-10019.....	92
44	Structure contour map of the top of the Navajo Formation.....	94
45	Well log correlation across the Nequoia Arch.....	95
46	Oil and gas exploration map of the San Rafael Swell and Desert showing the Nequoia Arch.....	96
47	Structure contour map of the top of the Moenkopi Formation outline of the approximate extent of bleaching in the Moenkopi Formation.....	97
48	Overview of Iron Wash fault model design in TrapTester.....	99
49	Triangle diagram of shale juxtaposition for the Iron Wash fault model.....	100
50	Triangle diagram of shale gouge ratio for the Iron Wash fault model.....	102
51	Triangle diagram of shale smear factor for the Iron Wash fault model.....	104

52	Triangle diagram of fault zone permeability for the Iron Wash fault model.....	106
53	Triangle diagram of fault zone capillary entry pressure for the Iron Wash fault model.....	108
54	Triangle diagram of predicted maximum CO ₂ column height for the Iron Wash fault model.....	110
55	Stress field map of eastern Utah and western Colorado.....	112
56	Geomechanical plots with components used in predicting fault failure along the Iron Wash fault for cohesionless faults.....	114
57	Geomechanical plots with components used in predicting fault failure along the Iron Wash fault for faults with cohesion of 5 MPa.....	115
58	Summary of the Iron Wash fault zone with location of major structural components and location of areas with evidence for fluid migration.....	118
59	Summary of the two fault relay systems studied at the Iron Wash fault zone....	119
60	Summary of fault facies observed along the Iron Wash fault zone with interpreted shale gouge ratio and seal effectiveness	123
61	Modeling results showing gas saturation from injected CO ₂ into the White Rim Sandstone	127
62	Modeling results showing gas saturation from injected CO ₂ interacting with a fault	127
63	Perspective view of modeled fault surface of the Iron Wash fault contoured with fault zone characteristics.....	128
64	Perspective view of modeled fault surface of the Iron Wash fault contoured with fault zone characteristics.....	130

INTRODUCTION

This thesis assesses a fault zone as a potential fluid pathway for carbon dioxide (CO₂) stored in a saline formation underground. This approach is motivated by the fact that anthropogenic CO₂ resulting from the combustion of fossil fuels is a significant contributor to increasing levels of greenhouse gases in the atmosphere (Figure 1; Intergovernmental Panel on Climate Change, 1990, 1992, 2001, 2005; Carbon Mitigation Initiative, 2013). Globally, annual CO₂ emissions were estimated to be 24 gigatonnes (Gt) in the year 2000 and increased to an estimated 31.6 Gt in 2011 (Figure 1; Intergovernmental Panel on Climate Change, 2005; National Energy Technology Laboratory, 2012; International Energy Agency, 2012; Carbon Mitigation Initiative, 2013). Of the total global emissions in 2011, approximately 60% of emitted CO₂ was derived from stationary sources such as power plants and industrial operations, with coal accounting for about 45%, oil for 35% and natural gas for 20% of the total emissions (Intergovernmental Panel on Climate Change, 2005; National Energy Technology Laboratory, 2012; International Energy Agency, 2012). Various technologies for carbon management and mitigation are currently under development (Figures 1 and 2) including the geologic storage of CO₂, or, carbon capture and storage (CCS) (Intergovernmental Panel on Climate Change, 2005; Carbon Mitigation Initiative 2013). The process of CCS involves sequestration large volumes of CO₂ into deep, underground geologic formations, or used in the process of secondary recovery of oil and/or gas (Figure 2; Halloway, 2001; Intergovernmental Panel on Climate Change, 2005; Carbon Mitigation Initiative 2013). Studies have shown that CCS is a viable option for the management of greenhouse gas

emissions and that the technology could play a significant role in emissions mitigation in the U.S. and elsewhere (Intergovernmental Panel on Climate Change, 2005).

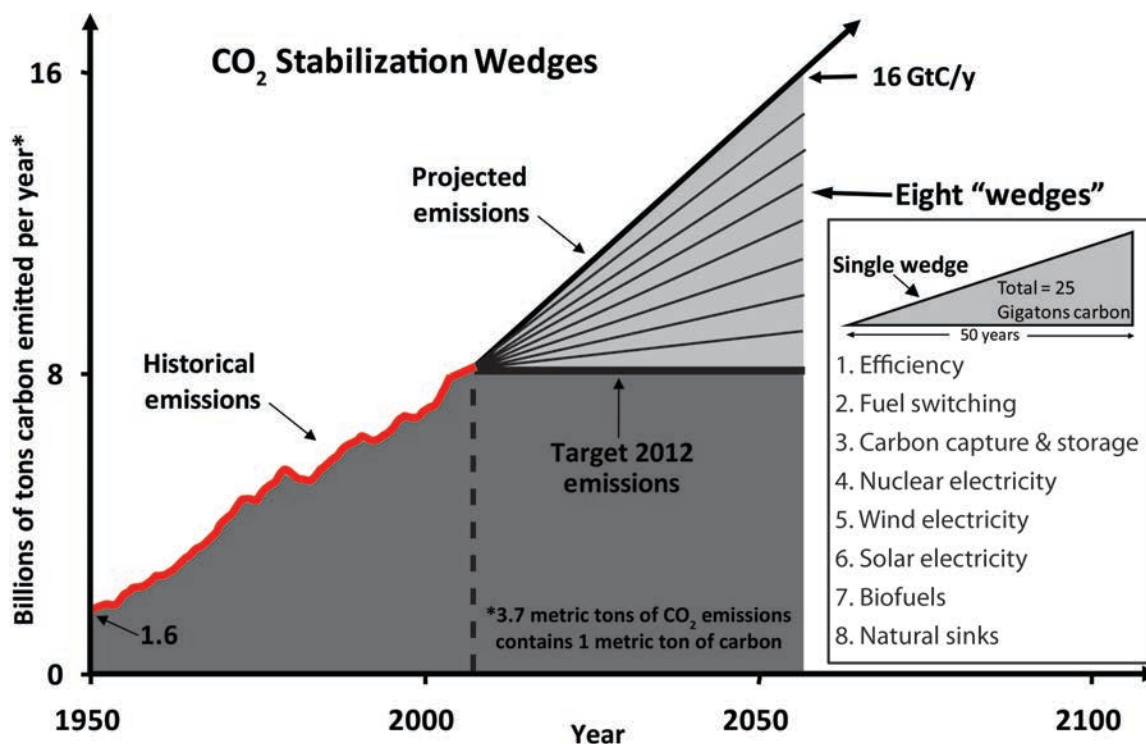


Figure 1. Overview of proposed CO₂ stabilization wedges. Plot of historical and projected future carbon emissions with proposed CO₂ stabilization strategies divided into eight wedges and an example target emissions based on 2012 emissions level (modified from Carbon Mitigation Initiative, 2013).

Geologic storage of CO₂ is accomplished by injecting CO₂ at depth into depleted oil and gas reservoirs or stacked geologic formations identified as saline aquifers that possess the ability to keep CO₂ from returning to the surface (Figure 2). As of 2005, there were three active CCS programs in the world operation at an industrial scale (injection of >1MtCO₂yr⁻¹): the Sleipner project in the North Sea, the Weyburn project in Canada and the In Salah project in Algeria (Intergovernmental Panel on Climate Change, 2005). In

the United States, potential sites for sequestration have been identified on the Colorado Plateau (Allis et al., 2001) and other locations throughout the country. Currently, a major concern for the viability of potential storage sites is the ability of underground reservoirs to adequately store injected CO₂ for reasonable amounts of time (National Energy Technology Laboratory, 2012), as well as having clear policy guidelines to define reasonable volumes that must remain sequestered on different time scales (Intergovernmental Panel on Climate Change, 2005).

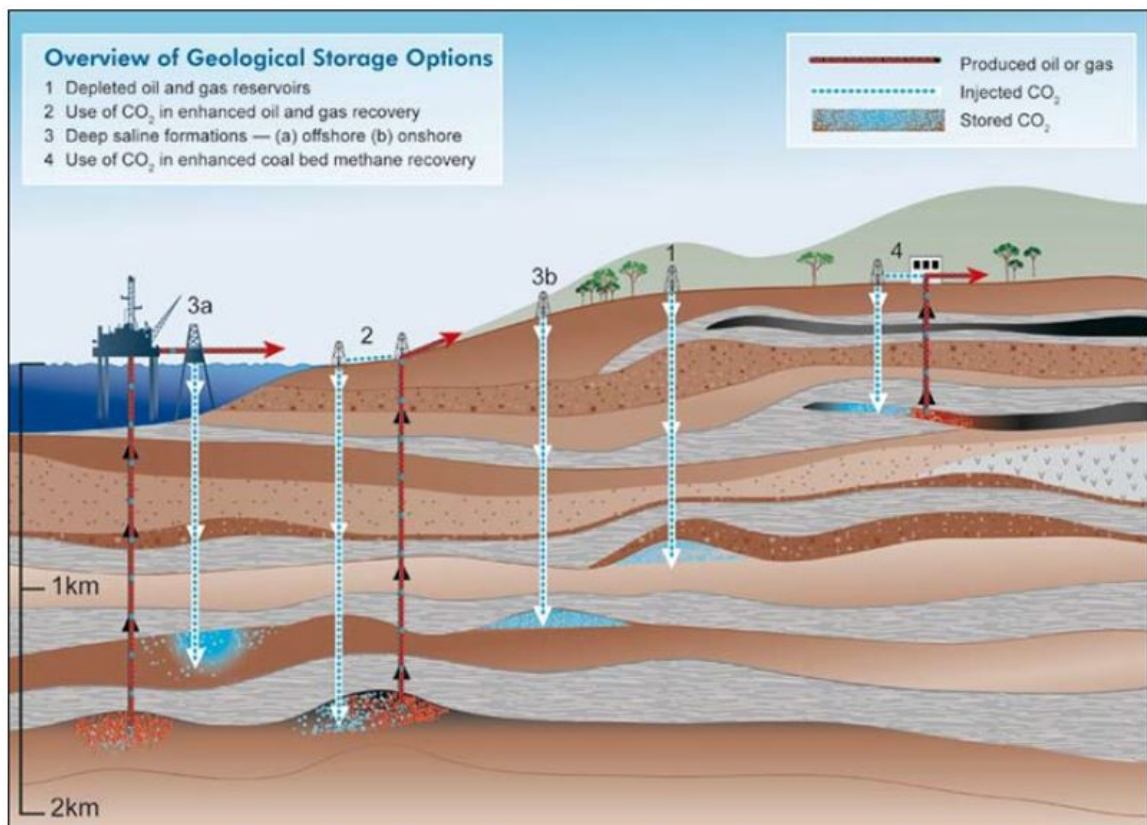


Figure 2. Schematic overview of geological storage types used in geologic sequestration of CO₂ (modified from Intergovernmental Panel on Climate Change, 2005).

Technological shortcomings for CCS have been identified by the Intergovernmental Panel on Climate Change and others (Zoback and Gorelick, 2012) and are one reason that the proliferation of this potential carbon mitigation technique has not occurred at large-scales world-wide. One of these technological shortcomings is the uncertainty associated with potential escape mechanisms from storage sites (Figure 3). Leakage of CO₂ through natural pathways within geologic seals such as fault and fracture networks represents a major concern when assessing the leakage risk of a potential storage site. This scenario can be studied at naturally occurring CO₂ leakage sites with numerous examples available in southern and central Utah (Evans et al., 2004). Furthermore, faults and their associated damage zones represent additional uncertainty when assessing these natural leakage pathways.

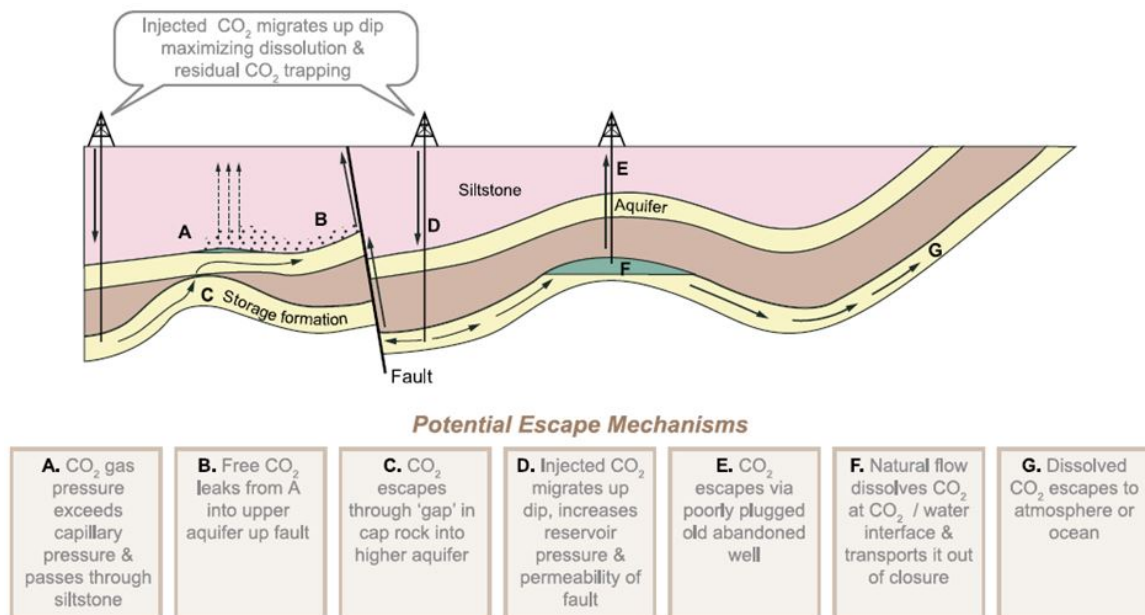


Figure 3. Schematic overview of potential escape mechanisms of geologically sequestered CO₂ out of injection reservoirs (modified from Intergovernmental Panel on Climate Change, 2005).

The Southwest Regional Partnership on Carbon Sequestration has identified a preliminary test injection site at the Gordon Creek field in Carbon County, Utah (Figure 4; McPherson and Grigg, 2010). This site will serve as a test location for a possible future large scale injection of CO₂ that could be sourced from the local Hunter and Huntington coal-fired power plants (Figure 4; Allis et al., 2003; McPherson and Grigg, 2010). The primary reservoir for injection at this site is the Navajo Sandstone with the overlying Carmel Formation acting as a first-order seal to prevent upward migration of the injected CO₂ (Allis et al., 2003).

Previous work has been done in the central San Rafael Swell specifically examining the structure as an analog for CO₂ storage sites (Barton, 2011). Structure contour maps developed by Barton (2011) for key intervals within the Mesozoic rock in the San Rafael Swell show the geometry of the top of the Carmel Formation and are projected over the eroded core of the San Rafael Swell to show what the restored geometry of the monocline may have been. Structures consistent with leakage of fluids from reservoirs through overlying seals in migration pathways such as faults and fractures have been identified within faults in the region (Shipton et al., 2004; Barton, 2011; Petrie and Evans, in review). Previous workers have used fault linkage potential maps and stratigraphic restoration maps to quantify fault interaction and leakage potential (Barton, 2011).

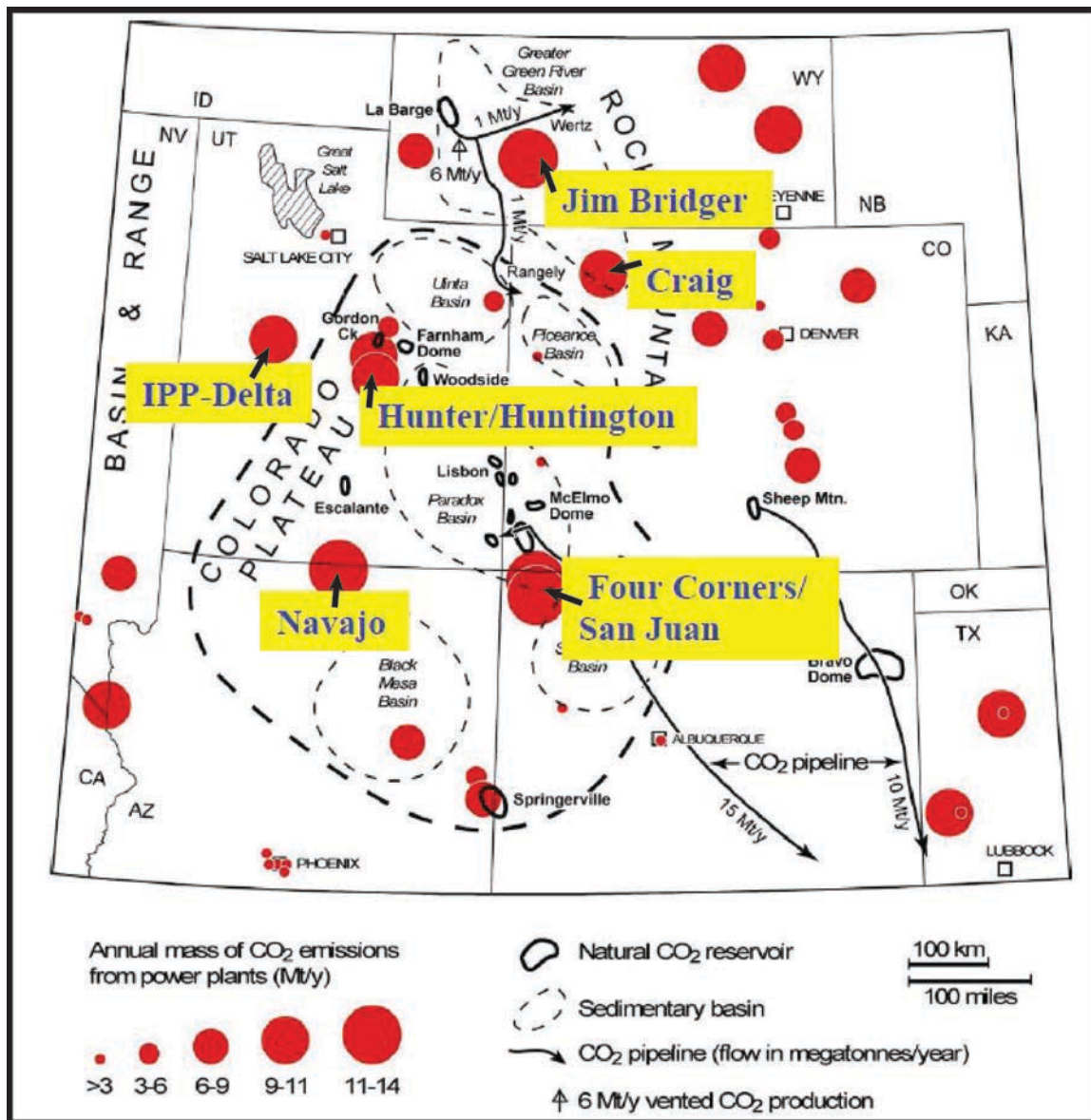


Figure 4. Location map and annual CO₂ emitted from point sources in the Four Corners region. Names of largest power plants in the region are provided for reference (modified from Allis et al., 2003).

Motivation

The sealing nature of faults with respect to upwards or lateral migration of fluids in the subsurface is a source of uncertainty when proposing injection projects for geologic storage of CO₂ and is still much debated (Evans et al., 2004; Intergovernmental

Panel on Climate Change, 2005; Dockrill and Shipton, 2010; Zoback and Gorelick, 2012). For example, disposal of wastewater, CO₂ or other fluids by injection into underground reservoirs may contribute to or result in the triggering of earthquakes (Wessen and Nicholson, 1987; Nicholson et al., 1988; Horton, 2012; Zoback and Gorelick, 2012; Rubenstein et al., 2013; Virgas et al., 2013; Karenen et al., 2013). The sealing and/or leaking nature of faults in the subsurface as well as their internal architecture, hydrologic characteristics, associated structures and damage zones is also of interest to the petroleum industry in a variety of applications in the exploration and exploitation of hydrocarbons (Hesthammer and Fossen, 2000; Fisher et al., 2001; Ligtenberg, 2005).

Fault and fluid interactions are extremely complex and often difficult to predict. Faults commonly exhibit very different structures and flow properties along strike, acting as conduits for fluids in some locations and baffles or barriers to fluids in other locations (Berg and Skar, 2005; Fisher et al. 2001; Braathen et al., 2009). Fluid overpressures at depth, or as a result of the injection of CO₂ into underground reservoirs presents an additional complexity that still needs more study (Gudmundsson, 2001; Phillip, 2012). Evidence for fluid migration along faults at outcrop analogs is a key factor in an analysis of a fault system with respect to sealing characteristics. Detailed characterization of fault zones is required prior to making an assessment of the fault in question, and in some cases, even a fault that would be suspected to be sealing may still leak (Shipton et al., 2004).

Current guidelines on permissible leakage rates of sequestered CO₂ out of geologic formations at depth are not clearly defined, but various studies have proposed

that the economic threshold for viability is somewhere between 0.1%/year and 1%/year (Ha-Duong and Keith, 2003; Intergovernmental Panel on Climate Change, 2005). With this benchmark in place, the nature of subsurface fluid flow and potential leakage pathways must be well understood prior to any injection occurs. Accordingly, a detailed understanding of the nature of faults and the associated damage zones is crucial to making an analysis of potential storage sites. Furthermore, much of the understanding of subsurface fluid flow is based on knowledge from the petroleum industry, where the extraction of fluids and a resulting reservoir pressure drop is the end result. Additional data has been gathered where CO₂ is only used in enhanced oil recovery operations in some petroleum fields. In contrast, injection of supercritical CO₂ fluid will increase reservoir pressures of fluids with different capillary entry pressure properties and densities. This may result in a completely different interaction of fluids, faults, damage zones and fracture networks. Having additional data on the geometry of faults and associated damage zones will enable a better analysis of these areas potentially acting as leaking pathways for injected fluids.

Subsurface monitoring and modeling has shown that CO₂ injected at depth as a supercritical fluid migrates both laterally and vertically controlled by the permeability and hydraulic gradient within the reservoir (Chang and Bryant, 2007; Arts et al., 2008; Zhou et al., 2009). Injected CO₂ acts as a buoyant plume when injected into reservoirs containing saline water and preferentially migrates upwards until a top seal such as a low-permeability rock formation, hydraulic barrier, or a sealing fault is encountered (Chang and Bryant, 2007; Arts et al., 2008; Zhou et al., 2009). As CO₂ plumes migrate upwards and pressure in the reservoir increases, the chance of seal failure increases. The increase

in reservoir pressure could potentially result in the reactivation of faults within reservoirs in CO₂ injection locations increasing the risk for CO₂ leakage. Understanding internal fault structure and associated fracture networks and their hydraulic conductivity will help in the planning of the rate of injection and storage capability of specific reservoirs.

Significant portions of today's unconventional hydrocarbon production is from naturally fractured reservoirs or reservoirs in which fractures are induced and/or fault seal analysis plays a role in the risk analysis of prospective petroleum plays (Nelson, 1985; Aydin, 2000). This project has implications for reservoir management, reservoir performance, fluid entrapment in naturally fractured systems, fluid leakage along high permeability pathways, and detection and prediction of fracture zones related to faulted systems (Nelson, 1985). Fault-seal analysis is crucial to the petroleum and other industries in understanding the nature of migration or entrapment of fluids in the subsurface and in the risk analysis for leakage of reservoirs prior to and during drilling operations (Nelson, 1985; Moretti, 1998).

Objectives

We examine the nature of faulted seal-reservoir analogs above the Nequoa Arch and adjacent to the San Rafael monocline along the Iron Wash fault zone in central Utah (Figure 5). The work characterizes the geometry and architecture of the Iron Wash fault zone and develop computer-based models of the fault zone that are used to predict the characteristics and behavior of the fault at depth.

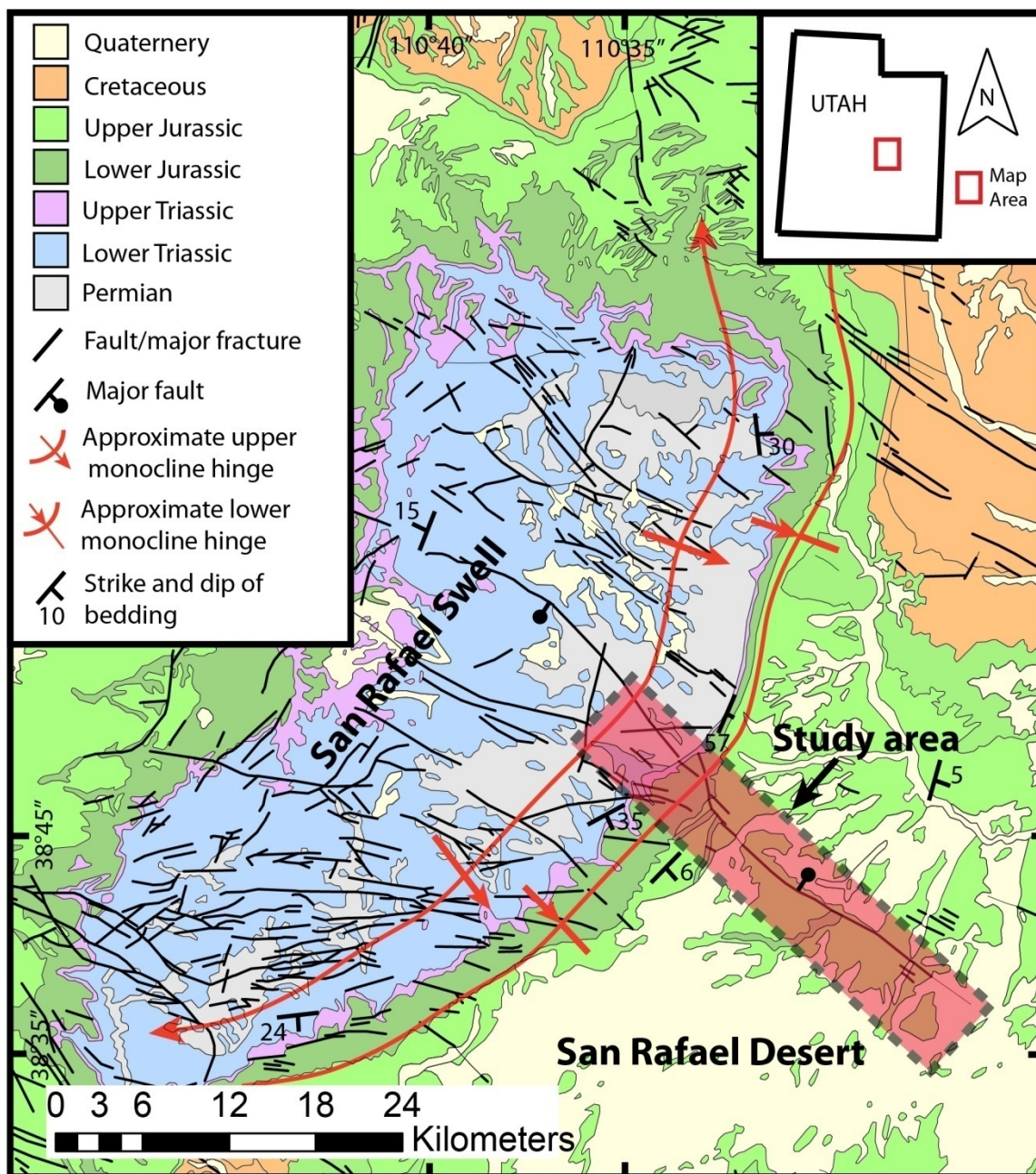


Figure 5. Geologic map of the San Rafael Swell and San Rafael Desert areas with a box showing the Iron Wash fault study area (modified from Hintze et al., 2000; Doelling, 2002).

This study has three overarching goals: 1) we use outcrop data to establish the nature of fault zone architecture with importance for fluid migration predictions, 2) incorporate field observations and data with subsurface data into a simple model of the fault zone to help assess the sealing behavior of faults in the subsurface, and 3) use fault kinematic data to determine how strain is distributed along a fault in different structural settings along the fault.

The specific objectives of this project are to:

1. Map the surface expression of the Iron Wash fault zone and determine throw profiles of all major fault strands.
2. Characterize the fault damage zone in different structural settings and within different rock types.
3. Conduct strain analysis along the fault on major stands of the fault and within fault linkage structures.
4. Perform petrographic and mineralogical analysis of microstructures, deformation features, altered and mineralized faults and fractures related to fluid migration.
5. Apply surface geophysical detection methods to imaging the fault zone in the shallow subsurface and use surface data to help interpret these results.
6. Combine well and borehole data with field data to construct subsurface models of the region surrounding the fault zone and models of the fault zone focusing on fault seal characteristics.

The Iron Wash fault field area was studied because it contains evidence for multiple generations of deformation and the resulting overprinting of younger faulting on older folding in reservoir/caprock analogs. Exposures of the fault core and preserved slip-

vector data allow for kinematic analysis of the distribution of strain along the length of the fault and within fault linkage structures. The area contains well-exposed examples of fault relay zones at different stages of fault linkage and at different structural levels. Fault relays expose areas of the fault where the contact between an analog target injection reservoir and the top seal can be seen. This allows for the investigation of the impacts of these fault relays on the seal integrity and possible structures related to seal bypass. Many examples of mineralized faults and fractures within the fault zone preserve a history of fluid migration along the fault with evidence of multiple fluid types and several generations of precipitation and mineralization.

Hypotheses that are tested in this thesis include:

1. The Iron Wash fault zone experienced an episode of extensional deformation that was structurally influenced by the pre-existing San Rafael monocline near its midpoint. We test the hypothesis that the geometry of the fault zone will reflect this structural overprinting in its width, orientation and intensity of deformation.
2. The southeast segment of the fault has formed in the Colorado Plateau stress field and therefore has experienced plane-strain with north-northeast-south-southwest extension. The western segments have experienced three-dimensional strain resulting from the stress transition zone between the Basin and Range stress field and the Colorado Plateau stress field (Reches, 1978; Aydin and Reches, 1982; Krantz, 1988). We test the hypothesis that the western parts of the fault have undergone three-dimensional strain due to both Basin and Range-related deformation and Colorado Plateau extension.

3. In the process of multiple segments of non-linked faults becoming increasingly structurally connected, the net length has increased, the Iron Wash fault zone has produced several relay zones that are both hard- and soft-linked. We test the hypothesis that these two distinct relay styles will have different internal structure, fault and fracture distribution and orientation, and strain transfer mechanisms.
4. Fault zone width is proportional to throw on the fault and will have higher average fault throw to fault zone width ratio in structurally complex areas of the fault zone such as fault tips, relays zones and structural intersections (e.g. Robertson, 1983; Scholz, 1987; Hull, 1988; Walsh and Waterson, 1988; Evans, 1990; Childs et al., 2009; Faulker et al., 2011).
5. Relay zones will have increased deformation intensity relative to damage zones surrounding discrete fault planes and that damage zone volume in the hanging wall of the fault is more extensive than in the footwall (Wilkins et al. 2001, Davatzes et al., 2003; Berg and Skar, 2005; Savage and Brodsky, 2011; Faulkner et al., 2011; Schueller et al., 2013).
6. Individual segments of the Iron Wash fault produced fault propagation folds that are both continuous and/or segmented across fault relays and accommodate a significant portion of the throw across the fault.
7. Fractures surrounding the fault have acted as conduits for several types of fluids during multiple phases of fluid flow.
8. Due to the relatively modest throw on the Iron Wash fault and the nature of the sedimentary units being faulted, the fault will fail to behave as a lateral or vertical seal to fluid migration.

The Iron Wash fault field area (Figure 6) was selected as a study site due to the presence of a fault that formed at depth, has been subsequently exhumed, contains carbonate alteration and mineralization along and near the fault and allows for analysis of the fault core, damage zone and fault-related structures. The Iron Wash fault is analogous to faults found in the subsurface provides insight into the influence of faulting on seal and reservoir lithologies and the mechanics of fault linkage and propagation. The fault juxtaposes of numerous reservoir/caprock lithologies (Figure 7) and this provides an opportunity to characterize the fault-zone geometries and architectures within different rock types and structural levels. Well and borehole data from oil and gas exploration drilling within the area also provide the ability to constrain the subsurface geometry of the rocks cut by the fault in the San Rafael Swell and San Rafael Desert.

Geologic and Structural Setting

The Colorado Plateau consists of Cambrian through Tertiary sedimentary rocks that lie unconformably on Proterozoic metamorphic and metasedimentary basement (Pipiringos and O'Sullivan, 1978; Sprinkle, 1994; Nuccio and Condon, 1996; Sprinkle et al., 2011). Permian through Jurassic sedimentary rocks are exposed in the San Rafael Desert and San Rafael Swell (Figures 5 and 7; Doelling, 2002). During the Cambrian through Mississippian the region was tectonically stable and primarily carbonate rocks were deposited on a cratonic shelf in a shallow-marine environment (Kelly, 1955; Poole and Sandberg, 1991; Poole et al., 1992; Sprinkle, 1994). In the Pennsylvanian and Permian, collision of the super-continent Laurentia and Gondwana resulted in regional uplift and the development of localized basins (Kelly, 1955; Nuccio and Condon, 1996)

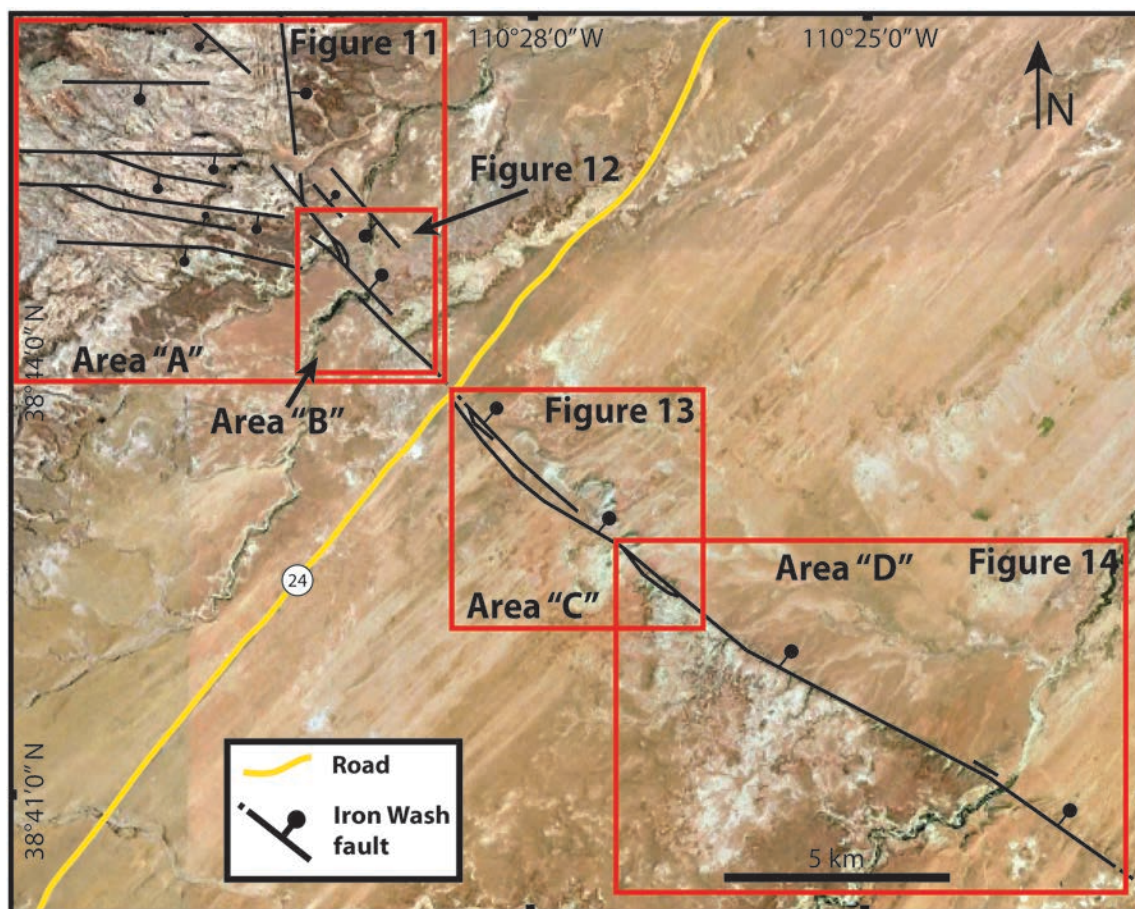


Figure 6. Annotated aerial photo of the Iron Wash fault with boxes showing locations of detailed maps of the Iron Wash fault zone. Areas A through D are referenced throughout the text to clarify field localities (modified from Googleearth.com).

where sediments were deposited into warm, shallow waters within fairly restricted basins. These units consist of marine limestone, dolostone, shale, anhydrite, halite, sandstone and mudstone (Hintze, 1993; Sprinkle, 1994; Hintze and Kowallis, 2009). The tectonically important Pennsylvanian Paradox Formation was deposited during this time and consists of up to 500 m of halite, gypsum, shale and mudstone (Foxford et al., 1996; Nuccio and Condon, 1996; Hintze and Kowallis, 2009). Magmatic arc development during the Triassic and Jurassic provided increased clastic sediment input to regional basins due to

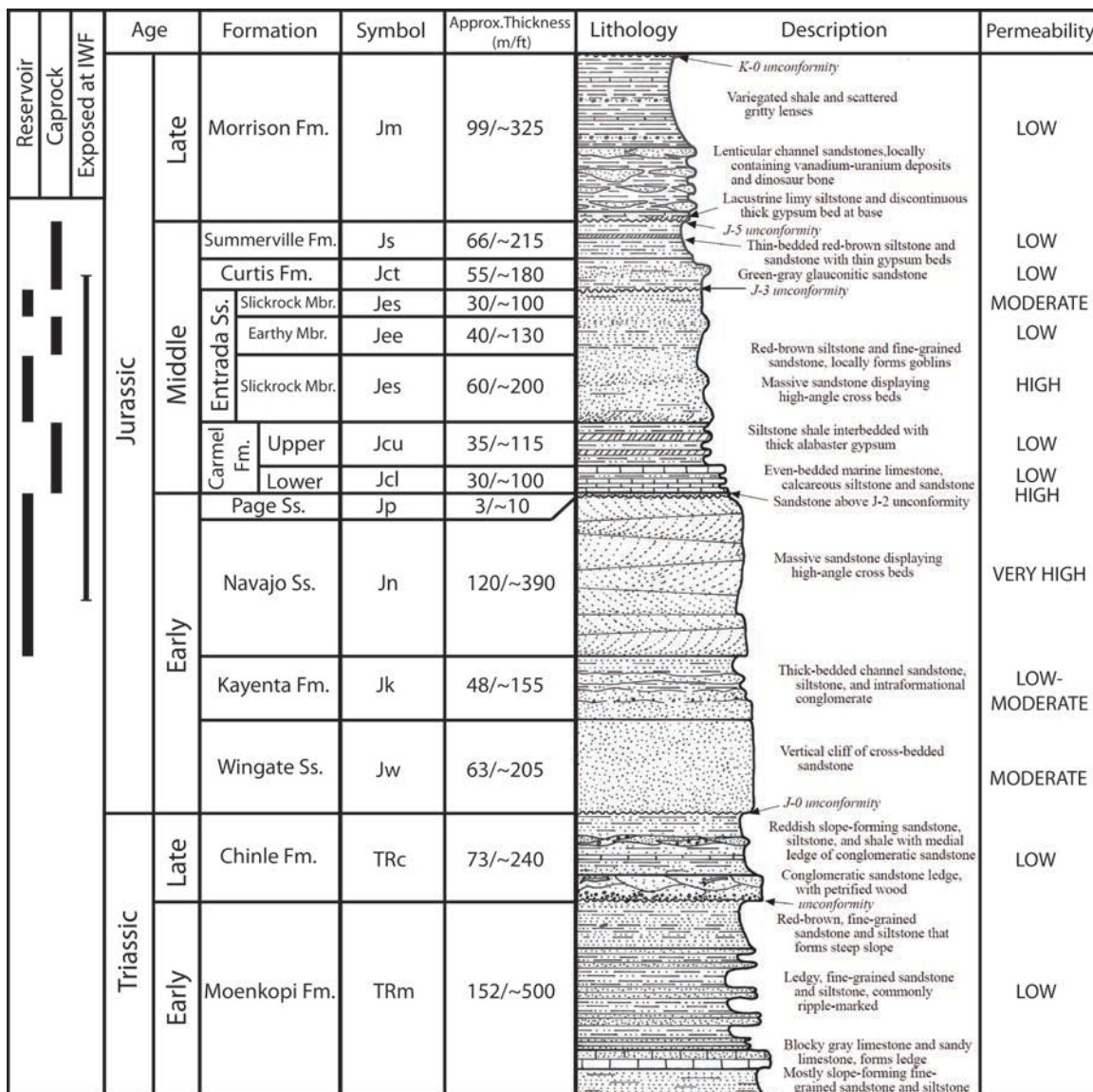


Figure 7. Generalized stratigraphic column for Jurassic and Triassic rocks in San Rafael Desert. Reservoir/caprock pairs characterized in this study are noted along with rocks exposed in the field area (modified from Chan et al., 2000; Doelling, 2002; Barton, 2011).

periodic uplift of source terrain (Dickinson et al. 1988; Dickinson, 2004; Hintze and Kowallis, 2009). Sedimentation during this time was characterized by dominantly continental environments with periodic marine incursion (Stewart et al., 1972; Sprinkle,

1994; Hintze and Kowallis, 2009). Triassic sedimentary environments include fluvial, lacustrine, sabkha, and eolian, as reflected in sandstones, mudstones and limestones of the Moenkopi and Chinle Formations (Hintze, 1993; Hintze and Kowallis, 2009). Early Jurassic sedimentary rocks are dominated by eolian erg deposits when widespread sand sheets covered much of the western United States and is represented by the enigmatic cross-stratified eolian sandstones of the Glen Canyon Group and the lower San Rafael Group (Sprinkle, 1994; Verlander, 1995; Kocurek, 2003; Sprinkle et al., 2011). In the middle Jurassic, a marine incursion began to inundate the eolian system and deposit the fossil-bearing marine limestones, mudstones and shales of the Carmel Formation (Kocurek and Dott, 1983; Hintze, 1993; Sprinkle et al., 2011). Sprinkel et al. (2011) subdivide the Carmel Formation into four distinct members: the Windsor Member, the Paria Member, the Crystal Creek Member, and the Co-op Creek Limestone Member. For simplification in this study, we have decided to maintain a simple nomenclature of lower Carmel and upper Carmel Formations. This shallow seaway eventually retreated, allowing deposition of the sandstones and mudstones of the Entrada Formation in a system of widespread mudflats, fluvial and eolian deposition (Hintze, 1993; Sprinkle et al., 2011). An additional marine incursion is recorded in the marine limestones, shales and mudstones of the Curtis Formation (Hintze, 1993; Nuccio and Condon, 1996; Currie, 1997). Middle Jurassic rocks are the primary units exposed at the surface within the field area. Older rocks are investigated primarily using well data to constrain the subsurface geometry and petrophysical properties of these formations.

The sedimentary package that comprises the Colorado Plateau (Figure 7) was deformed during the late Mesozoic and into the Cenozoic producing many of the

enigmatic features of central Utah (Figure 8; Dickinson et al., 1988; Bump and Davis, 2003; Dickinson, 2004). The San Rafael Swell is a broad, north-northeast trending, doubly-plunging, highly asymmetrical anticline (Dickinson et al., 1988; Bird, 2002; Bump and Davis, 2003) commonly referred to here as a the San Rafael monocline due to its asymmetry. This structure related to Late-Cretaceous to Early Tertiary deformation of the Laramide Orogeny as characterized by regional thrusting (reverse faulting) involving deep crystalline basement (Dickinson et al., 1988; Jones et al., 1998; Bird, 2002; Bump and Davis, 2003; DeCelles, 2004; Saleeby, 2003; Jones et al., 2011) with the maximum compressive stress in a northeast-southwest orientation (Bird, 1998; Jones et al., 2011). Laramide deformation resulted from the subduction of the Farallon slab under continental North America and shallowing of the subducting slab angle resulted in deformation within the continental interior (e.g. Saleeby, 2003; Jones et al., 2011). Some disagreement about the exact mechanisms by which slab-continent interactions resulted in regional orogenesis still remains (Bird, 1984; Jones et al., 2011). Laramide basement faulting produced the broad anticlines and monoclines observed along the western margin of the Cordillera, including many of the anticlines and monoclines of central and southern Utah (Huntoon and Sears, 1975; Dickinson et al., 1988; Hintze, 1993; Bird, 1998; Bump and Davis, 2003; Jones et al., 2011). The Colorado Plateau province was uplifted as a relatively rigid and intact region that experienced far less internal deformation than surrounding provinces (Bird, 1998; Sonder and Jones, 1999; Jones et al., 2011). Timing of the onset of extension in the eastern Basin & Range province on the Sevier Desert Detachment fault has been estimated to be ~19 Ma based on thermochronologic data (Stockli et al., 2001). Extensive work has been conducted on the Moab Fault, located in

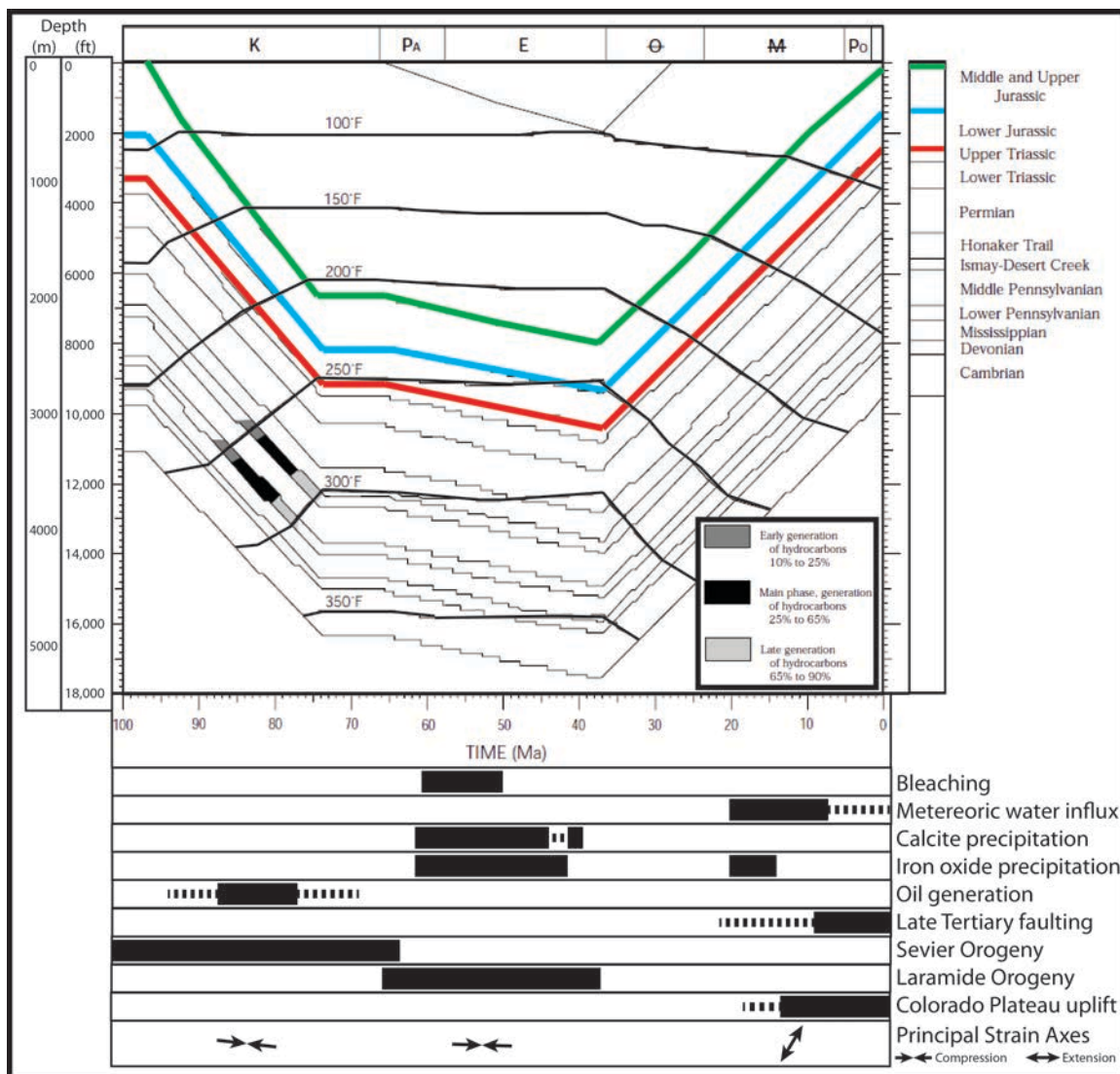


Figure 8. Burial history, thermal model and key geologic events of the area near Green River, Utah (modified from Nunccio and Condon, 2000; Bird, 2002; Davatzes, 2003 and references therein).

east central Utah, where a long and complex history of activity has been described starting as early as the Triassic due to salt tectonism with reactivation during the Tertiary (Solum et al., 2005). The interpreted regional timing of regional tectonic events have been examined by previous workers (e.g. Dickinson et al., 1988; Hintze, 1993; Nuccio

and Condon, 1996; Peaver et al., 1997; Chan et al., 2001; Stockli et al., 2001; Davatzes, 2003; Solumn et al., 2005) and are summarized in Figure 8.

Uplift of the San Rafael Swell most likely involved the slip along one or more major reverse faults within the Precambrian basement (Maerten et al., 2001). The Consortium for Continental Reflection Profiling conducted a regional two-dimensional seismic survey that transected the core of the San Rafael Swell, however, it was inconclusive as to the existence of the reverse fault (Allmendinger et al., 1987), and other hypotheses regarding the mechanisms of formation of the fold have been proposed such as warming of heterogeneous lithosphere (Roy et al., 2009). Halokinesis, resulting from the movement of the thick salt deposits within the Paradox Basin, occurred regionally during the Permian through the Early Jurassic and again during the Late Cretaceous through the Tertiary (Doelling, 1988; Hintze, 1993; Foxford et al. 1996). Salt diapirism and dissolution is associated with the development of large salt anticlines and salt-cored faults in the region resulting from the collapse of overlying strata (Doelling, 1988). Salt movement has been shown to be active in the region by the presence of deformed Quaternary deposits (Oviatt, 1988). Paradox salt deposits thin dramatically or are completely gone adjacent to the San Rafael Swell (Nuccio and Condon, 1996) and minimal salt is believed to underlay the Iron Wash fault study area due to the proximity to the edge of deposition of salt in the Paradox Basin (Friedman et al., 1994).

Multiple generations of fluid movement and mineral precipitation have been documented within the Colorado Plateau region for a variety of different fluids and oxidation-reduction conditions (Figure 8; Foxford et al., 1996; Nuccio and Condon, 1996; Huntoon et al., 1999; Chan et al., 2000). The geochemical conditions during alteration are

generally categorized as an oxidizing environment, resulting in the precipitation of oxides, or a reducing environment, resulting in removal of oxides from the system (Foxford et al., 1996). Hematite, a ferric (Fe^{3+}) iron oxide, is the most common oxide that is observed in the Iron Wash field area and is interpreted to be the result of oxidizing conditions (Foxford et al., 1996; Chan et al., 2000). Bleaching resulting from removal hematite and manganese oxides from localized areas or regionally is interpreted to be the result of reducing conditions (Foxford et al., 1996; Chan et al., 2000).

Localized bleaching, primarily in the form of bleached fractures and bleached faults, is observed in the field commonly as elongate halos of lightly colored rock relative to the surrounding host rock that are off-white to yellow. Bleaching is most apparent in the red to brown rocks of the Earthy Member of the Entrada Formation and the Carmel Formation. Regional bleaching (bleaching of the entire formation) is seen in the Navajo Formation and the Slickrock Member of the Entrada Formation (Foxford et al., 1996; Chan et al., 2000). Hematite is found in the Iron Wash field area as hematite coated grains, hematite concretions, hematite stained fractures, and as hematite staining calcite within faults. The interpreted regional timing of oil migration, fluid migration, bleaching, iron oxide and calcite precipitation have been examined by previous workers (e.g. Foxford et al., 1996; Nuccio and Condon, 1996; Peaver et al., 1997; Huntoon et al., 1999; Chan et al., 2000; Davatzes, 2003) and their relative timing is summarized in Figure 8.

Iron Wash Fault

The Iron Wash fault zone, the focus of this study, is a Late Cenozoic northwest-striking normal fault that extends approximately 25 km along the eastern edge of the San

Rafael Swell in central Utah (Aydin and Reches, 1982; Doelling, 1988, 2002; Friedman et al., 1994). It is approximately perpendicular to the primary structural trend of the larger San Rafael monocline (Figure 5). Overall, the fault strikes about 315° , dips steeply between $67-84^\circ$ northeast and accommodates normal slip with a small amount of left-lateral oblique motion. Maximum throw on the fault is about 120 m. The fault is broadly divided into three areas in this study: 1) the San Rafael Desert area to the southeast of the San Rafael monocline, 2) the area along the steep limb of the San Rafael monocline, and 3) the interior area west of the monocline (Figure 5). Mapping and field work focuses on the study area defined by the area within the steeply dipping beds of the monocline and in the San Rafael Desert (Figure 5). Mapped areas are shown in Figure 6 and will serve as reference throughout this thesis as to localities of specific field sites or sections of the fault zone and will be referred to as Areas A through D. The four areas of the fault zone (Figure 6) have different structural geometries and perhaps different structural histories associated with the development and linkage of multiple fault segments. This structural history may be represented by the kinematic indicators and geometries of the fault. The segments are investigated separately to understand the mechanics of structural linkage and propagation of the fault zone and characterize how both the intersection of structures and mechanical stratigraphy influence fault development.

The fault is well exposed in the San Rafael Desert east of the San Rafael Swell, where the fault offset shows that the northeast side is down and the surrounding units lay sub-horizontal (Figure 6; Aydin and Reches, 1982; Doelling, 2002). The fault strikes about 300° in the far eastern segments (Figure 6, Areas C and D), changing strike towards

the San Rafael Swell where they are more north-south oriented and nearly parallel to the axis of the monocline. The far western segments (west of the monocline) of the fault are more impacted by preferential erosion and weathering, with poorer exposures of the fault core and damage zone. Here, the fault strikes about 325° and has an opposite sense of slip, showing offset with the southwest side down-faulted (Doelling, 2002). Scissoring offset along the fault, or the reversal in relative motion of the fault, occurs in the steep limb of the San Rafael monocline and is associated with a wide damage zone within the steeply dipping beds in the fold limb.

The Iron Wash fault has a similar strike, length and throw to the northwest striking Late Cenozoic to Quaternary normal faults to the northeast and southwest, and its geometries suggest that it is likely an extensional normal fault within the uplifting Colorado Plateau (Wong and Humphrey, 1989; Flesch and Kreemer, 2010; Berglund et al., 2012; Ostenna, 2012; USGS, 2012). Age constraints on timing of slip on the Iron Wash fault are poor but studies on timing of regional events (Figure 8) suggest that faults of this nature were possible forming as early as the Oligocene (Chan et al., 2001; Davatzes, 2003). Salt-cored faults within the region, such as the Moab fault, began forming as early as the Triassic due to salt movement in the subsurface and have experienced several episodes of reactivation in the Mesozoic and Tertiary (Doelling, 1988; Foxford et al., 1996). Faults with similar orientation to the Iron Wash fault cut Quaternary deposits throughout the Colorado Plateau (e.g. Oviatt, 1988; Friedman et al., 1994; Ostenna, 2012; USGS, 2012) and a summary of the ages of movement on some of the similarly oriented fault can be found in Friedman et al. (1994).

Recent work on the Iron Wash fault by Fugro World Wide Inc. (www.fugro.com) geologists, working in a consulting role for Blue Castle Holdings in the process to site a nuclear power plant north of the town of Green River, UT (Dean Ostenna and Ozgur Kozaci, personal communication, 2012; Ostenna, 2012), investigated fault seismic hazard potential in the area as part of the federal regulatory framework to approve construction of new nuclear power facilities (Ostenna, 2012). No Quaternary fault scarps have been identified along the Iron Wash fault based on field work in this study (Dean Ostenna and Ozgur Kozaci, personal communication, 2012; Ostenna, 2012). Based on fault trenching and Quaternary geochronology of deposits overlying the fault, the minimum time since the last slip event is ~80,000 years using optically stimulated luminescence (OSL) dating technique (Joel Pederson, personal communication, 2013). Based on U-series dating of soil carbonates, an minimum age of ~300,000 years since the last slip event was determined by Fugro consultants (Joel Pederson, personal communication, 2013, for Fugro, Inc.). These ages may reflect a low event reoccurrence on the fault, a relatively small total offset on the last slip or the fact that Quaternary deposits do not record the last slip event or even the problem that deposits sampled do not record the last slip event. The simplest explanation is that the fault truly has had no significant slip in the last ~300,000 years. We conducted subsurface mapping of salt deposits using well data which supported results from other work that the Iron Wash fault study area is not underlain by salt either because salt moved out of the area to the east or because salt was never deposited in the area. Based on burial history and thermal models (Figure 8), it appears that the current exposure of the fault formed at no greater than about 2.5 km depth and < 90°C (Nuccio and Condon, 1996).

The Iron Wash fault cuts Jurassic rocks in San Rafael Desert (Figure 7) and Permian rocks in the core of the San Rafael Swell (Aydin and Reches, 1982; Doelling, 2002). The fault potentially represents the surface expression of a deep, reactivated pre-existing structure within the crystalline basement rocks and therefore existing structural fabrics may have influenced the formation and development of the fault (Huntoon and Sears, 1975). We see the intersection of two major structural grains: the northwest-striking Iron Wash fault zone and the older, northeast-trending San Rafael Swell. The Iron Wash field area allows for investigation of structural interaction of these two structural grains. The fault exposes many fault relays, step-over zones and fault propagation features with the fault zone becoming particularly complex at the intersection of the San Rafael monocline, where it develops a horst and graben complex east of the frontal monocline.

Terminology and Definitions

Fault zones can be described as containing an outer damage zone, an inner damage zone and a fault core (Figure 9; Aydin and Johnson, 1983; Chester and Logan, 1986; Caine et al., 1996; Micarelli et al., 2003). Protolith (host rock or country rock) represents the pre-faulting condition of the rock prior to initiation, coalescing and slip on a fault (Caine et al., 1996). A fault zone is a volume of deformed rock is unique to the fault creating the deformation and its architecture is highly dependent on the processes during the formation of the fault (McGrath and Davidson, 1995; Evans et al., 1997, Wibberley et al., 2008). Numerous factors control the nature of the fault core and damage zone including lithology, fault scale, fault type, deformation style and history, fluid

interactions with the fault, burial history and depth of faulting, et al. (Caine et al., 1996, Steen and Anderson, 1999).

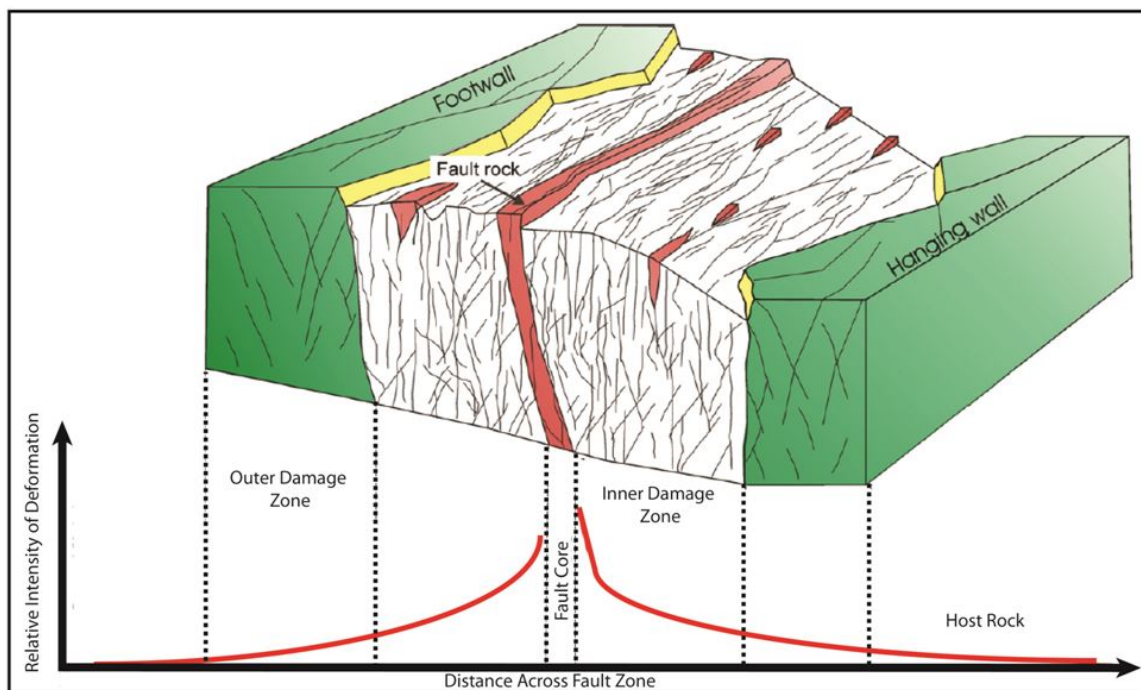


Figure 9. Schematic model of extensional fault geometry. Block diagram illustrating the associated inner and outer damage zones and the fault core that have resulted by deformation of the host rock (modified from Ganerod et al., 2008).

Due to differences in fault zone terminology and field practices used by various studies, comparison to previous work can be problematic (Evans, 1990; Childs et al., 2009). We use the term *fault core* to describe a central zone containing primary slip surfaces, cataclasite, fault breccia, and gouge material (Figure 10; Caine et al., 1996; Braathen et al., 2009). A *damage zone* (divided here into *inner* and *outer* damage zones) surrounds the fault core and consists of a network of deformed rock and subsidiary structures (Caine et al., 1996; Braathen et al., 2009). A damage zone is a volume of rock

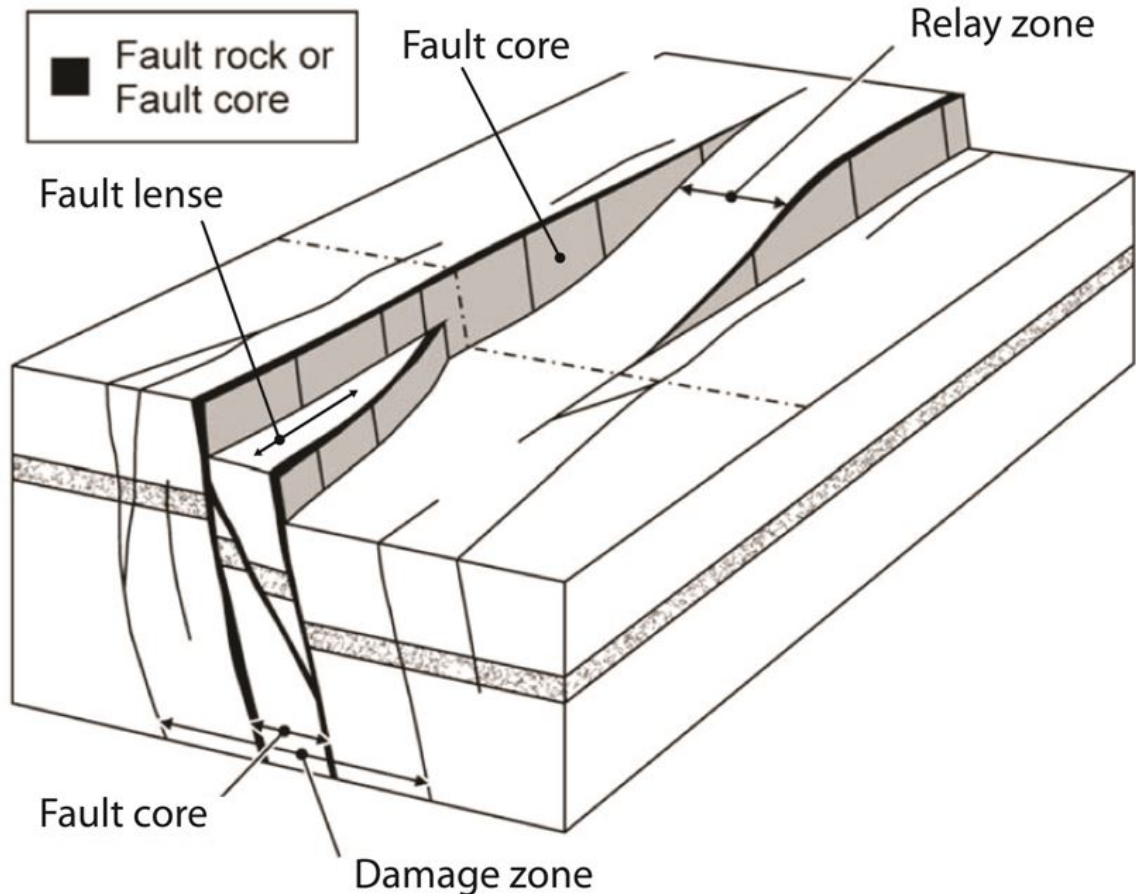


Figure 10. Schematic of structures associated with fault linkage and development. Key structures include fault lenses, fault relay zones, and fault damage zone surrounding a discrete fault core (modified from Childs et al., 2009).

surrounding a fault core that is characterized by a increased amount of deformation (small faults, fractures, veins, folds) relative to the surrounding host rock (Figure 9; McGrath and Davidson, 1995; Caine et al., 1996; Ganerød et al., 2008). All deformation related to the primary fault segments, related faults, fault splays, relay zones, fault lenses, fault-related folds and fault core, are collectively termed *fault zone* in this study (e.g., Sibson, 1977; Caine et al., 1996). We discuss individual *fault segments* that are part of the fault zone and structurally interact and link. Many studies use the term *fault displacement*

when comparing fault zone thickness to displacement (e.g., Kim et al., 2004; Childs et al., 2009). We use the term *fault throw* in this study because we have measured fault throw defined as the vertical component of displacement on a dip-slip fault by measuring the stratigraphic offset of the fault (we use the term displacement when comparing our results to prior studies). *Fault relay zones* accommodate the transfer of throw from one strand of a fault to another, with either complete or partial transfer of throw (Figure 10; Peacock and Sanderson, 1991; Childs et al., 2009). Strain that is concentrated in the primary slip surfaces of the fault strands must also be transferred either completely or partially (Peacock, 2002). Fault strands that surround relay zones exert stress on the relay zone and strain is dispersed across many secondary structures within the relay zone to accommodate the transfer of throw from one strand to the next (Peacock and Sanderson, 1991; Peacock, 2002). We use the term *fault architecture* to describe the spatial and geometric relationship between elements of the fault zone (e.g., Braathen et al., 2009). We measure *fault zone thickness* as the width (perpendicular to the fault zone) of a system of related fault segments and fault-related structures (Peacock et al., 2000).

A positive correlation of fault zone thickness and throw has been established by other workers (Robertson, 1983; Hull, 1988). Evans (1990) strongly disputes this assessment, suggesting that D:T relationships for fault thickness oversimplify the complex nature of fault zones. Fault cores may indeed thicken with displacement (e.g. Evans, 1990; Shipton et al., 2006), but overall fault zone thickness is a function of the number of fractures and fault and is therefore dependent on where it is measured along the fault zone in relationship to the nature of the fault (i.e. at relay zones or near dip changes in the bedding being faulted) (Evans, 1990; Shipton et al., 2006). For the

purposes of this section of the study, measurements were made in the field and using aerial photography of *fault zone* thickness as defined by Peacock et al. (2000) as a system of related fault segments that interact and link and by Childs et al. (2009) as an anastomosing network of through-going synthetic slip surfaces and associated fault rock. For clarification, fault zone is a more encompassing term than damage zone, which is used here to reference a zone surround the fault which has increased fracture intensity relative to the surrounding host rock.

Several distinct types of discrete structures are present in and around fault zones and are defined by the presence of discontinuities or mechanical defects in the rock that are typically cohesionless at the time of development (Schultz and Fossen, 2008; Braathen et al., 2009). Several types of fractures have been identified by previous workers: 1) dilatational fractures or open-mode fractures such as joints or veins, 2) compaction fractures such as compaction bands, and 3) shear fractures such as faults (Schultz and Fossen, 2008). Deformation bands are also commonly found within porous sandstones and have been described as thin zones of shear strain (Schultz and Fossen, 2008). Fossen et al. (2007) provides a more robust discussion of deformation bands types and the related impacts on reservoir properties.

Here, we use the fault zone compiled architecture model to guide our examination of the Iron Wash fault in order to differentiate data collected from various components of the fault and to allow for comparison to previous studies. We will also use the fault relay zone compiled architecture model guide our examination of the fault relays and lenses located within the Iron Wash fault zone.

Characterization of Fault Zones

Fault zone thickness, composition and internal architecture are key aspects of fault zone characteristics that help constrain fault mechanisms and their relationship to fluid flow (Caine et al., 1996). Empirical relationships for fault thickness and throw have been examined and discussed by many previous studies (Robertson, 1983; Scholz, 1987; Hull, 1988; Walsh and Waterson, 1988; Evans, 1990; Shipton et al., 2006; Childs et al., 2009; Faulker et al., 2011). Previous work has constrained the architecture of faults and damage zones (McGrath and Davidson, 1995; Rawling et al., 2001; Davatzes, 2003; Kim et al., 2004; Braathen et al., 2009; Faulkner et al., 2010), the permeability structure of faults (Sibson, 1996; Evans et al., 1997; Gudmundsson et al., 2001; Shipton et al., 2002; Hammond and Evans, 2003; Caine et al., 2010), the types of deformation that occur in various faults (Fossen and Hesthammer, 1997; Ogilvie and Glover, 2001; Vrolijk and van der Pluijm, 1999; Fossen et al., 2007; Rotevatn et al., 2008;), and the evolution by which these structures occur (Shipton and Cowie, 2001, 2003; Sammis and Ben-Zion, 2008). However, detailed case studies of fault zones are still highly in demand.

Various studies have utilized synthetic and model-driven fault analyses to look at the interaction of fluids and faults, using data derived primarily from outcrop studies (Hestir et al. 2001; Tveranger et al., 2005; Fredman et al., 2007, Zhang et al., 2009; Manzocchi et al., 2010; Fachri et al., 2013;). Detailed work on the asymmetry of damage zones both along strike and in the hanging wall and footwall of fault has shown significant spatial variations (Berg and Skar, 2005; Schueller et al., 2013). Mechanical overprinting is observed in many locations, for instance in Utah, and represent important information in inferring tectonic histories for fault activity (Bump and Davis, 2003;

Davatzes et al., 2003; Davatzes et al., 2005). Fault activity plays into significant uncertainties that are associated with predicting the sealing (or leaking) nature of a fault based either on outcrop analogs or subsurface data (Hammerhest and Fossen, 2000; Shipton et al., 2004; Dockrill and Shipton, 2010; Tueckmantel et al., 2010).

Damage zone width has been demonstrated to be asymmetric, generally wider in the hanging wall than in the footwall of a fault and has been shown to have spatial variations along strike (Berg and Skar, 2005). Damage zones are unique to the fault creating the deformation and the fault architecture is highly dependent on the processes during the formation of the fault (McGrath and Davidson, 1995; Evans et al., 1997, Wibberley et al., 2008).

Fault zones contain a wealth of small structures of various types, such as, deformation bands and fractures. In the continuation, we assume that such structures are well known to the reader. Otherwise, some of the many papers on the subject include: Sibson (1977), Narr and Suppe (1991), Caine et al. (1996), Evans (1997), Hammond and Evans (2003), Kim et al. (2004), Johansen et al. (2005), Rotevatn et al. (2008), Schueller et al. (2013), Torabi et al. (2013).

METHODS

This study uses qualitative as well as quantitative and semi-quantitative methods to constrain the geometry and intensity of deformation and mineralization within the fault core and damage zone. Various datasets examine different scales of deformation and alteration along the fault zone, from regional analysis of the impact of the fault to mesoscale fault segments and fault relay zones (100's of meters between fault segments)

to fracture networks and damage zones (meter to centimeter scale), to microscopic features of deformation (decimeter scale).

In this study, fault zone geometry, fault linkage structures and fault propagation structures are the primary focus. Data collected also characterize the density, aperture, and connectivity of fractures in the damage zone surrounding the fault. These data are derived from detailed mapping at scales of 1:6,000 to 1:60,000 which was used to characterize relay zones, fault lenses and fault propagation folding. Understanding fault relays, fault jogs and large fault lenses will help to better constrain the potential fluid flow pathways and high-permeability zones. Detailed mapping was undertaken in key outcrops where well-developed fault sealing features such as clay smear, re-cemented fault core and fault gouge may support considerations around fault behavior as a barrier or baffle to fluid flow for the Iron Wash fault. A three-dimensional characterization of the fault zone was constructed to constrain the geometry of the fault zone down dip into the subsurface (to the extent possible), along strike, and away from the fault core.

Field Mapping

Geologic field mapping was performed at a scale of approximately 1:6000 to 1:60,000 along the Iron Wash Fault zone, incorporating an area of ~100 km² to identify all geologic units affected by the fault and structures associated with the fault. Fault width was determined from field observations and fault maps. Fault throw was calculated from stratigraphic offset at sites where offset could be determined along the fault and was compiled into a detailed throw profile for the fault. Drill hole data was used to supplement field mapping and calculations of fault throw when possible.

Characterization of the damage zone was accomplished by quantifying the fracture density away from the fault core by using scanlines and stereo image analysis. Field photographs (stereo pair photographs) were rendered in three-dimension using Sirovision™ software package where pseudo-scanlines can be performed to characterize fractures. Field-based scanlines 30 to 400 m long, or fracture density characterizations within individual beds away from the fault, provided data on the density and orientation of fractures away from the fault core. A total of 17 scanlines were conducted for multiple purposes including for the characterization of the relay zones and to understand the changes in fracture density in different lithologies in the hanging wall and footwall. Starting in the inner damage zone or fault core, scanlines perpendicular to strike were used to characterize the amount of decay in fracture density from a region of high fracture density (low fracture spacing) near the fault core, to low fracture density (high fracture spacing) away from the fault core. In various locations along the fault, scanlines parallel to strike were used to examine fracture density variations along strike. Because of the nature of the exposures of the Iron Wash fault, more strike-perpendicular scanlines were acquired than strike-parallel scanlines.

Scanline data were collected in different lithologies in an attempt to attain a complete picture of the damage zone and to characterize a segmented fault as it cuts multiple lithologies with differing mechanical properties. A total of 9 scanlines were conducted in five different formations: Navajo Sandstone, lower Carmel Formation, upper Carmel Formation, Slickrock and Earthy Members of the Entrada Formation. For each of the units a fracture density scanline was conducted in the hanging wall and footwall of the fault. Because of the nature of the exposures scanlines within the same

formation were not at the same location for the hanging wall and footwall. There is no accessible location on the fault where the Navajo was exposed in the hanging wall where the fault had >10 m of throw, so no scanline was acquired. At various locations along the fault, specific localities are identified where the fault juxtaposes different mechanical stratigraphies and comparisons were made about the stratigraphy involved and the resulting fault expression. These data are used to characterize statistical relationships and better understand the influence of mechanical stratigraphy and lithofacies on fracture distribution and fault architecture propagation.

Detailed mapping at scales of 1:100 to 1:1,000 of the architecture of the fault core was performed along strike to document spatial variations in geometry along a single fault. Characterization of the fault core at various locations was conducted utilizing a classification of the expression of the core with schemes similar to those used in previous studies (McGrath and Davidson, 1995; Kim et al, 2004; Shipton et al, 2006), specifically focusing on characterization of fault facies (Braathen et al., 2009). Detailed analysis of the expressions of the fault core, or fault facies, provided insight into the heterogeneity and spatial variation of a single fault as it cuts different lithologies. Some examples of fault facies observed in the Iron Wash fault include rotated fault blocks, sheared blocks, re-cemented fault breccias, coalesced cataclastic deformation bands, distributed cataclastic deformation bands, clay gouge, gypsum smear, and fault step over (or fault relay) zones.

Tiny-Perm II (New England Research, www.ner.com), a hand-held instrument for field-based assessment of permeability, was used to measure the field permeability of rocks within the damage zone and to constrain the permeability of both filled and unfilled

fractures. Permeability measurements of specific fault related features, lithologies and of specific fault facies provided support for interpretation of features as being conduits for fluids or baffles (or barriers) to migration along or across the fault. An effort was made to adequately acquire Tini-Perm in strategic areas of the fault to have a complete along-strike profile of the fault and the associated characteristics.

Structural Petrology

Oriented strike-perpendicular thin sections were prepared from hand samples collected at key field localities along the Iron Wash fault from the Navajo Sandstone, upper and lower Carmel Formations, and Earthy and Slickrock Members of the Entrada Formation. Oriented hand samples were collected from the fault core and damage zone and targeted deformed rocks with features such as mineralized fractures, altered fractures, and breccias. Petrographic thin sections were professionally prepared by Burnam Petrographic. Petrographic analysis was used to examine mineralogy and microstructures related to deformation within the fault core, in the associated structures and in the damage zone. Microstructures resulting from different types of deformation mechanisms were examined to infer deformation history of the rocks. Features related to fluid-rock interactions were also identified to better understand the history and role of fluids and/or hydrocarbons within the fault zone. The objective of the petrographic analysis was to provide insight into the role of fractures in conducting fluids, understanding multiple generations of deformation and fluid migration, crack growth and propagation, and other general insights into processes related to faulting.

X-Ray Diffraction Analysis

Samples collected from key locations along the Iron Wash fault were prepared and analyzed using standard X-ray diffraction (XRD) methods to determine mineralogy to supplement mineralogical analysis done using petrographic thin sections. A total of 15 samples were analyzed using standard laboratory methodology for XRD when preparing, processing, analyzing and interpreting samples. These analyses examined compositional variations of the fault facies identified in later sections, the damage zone, and fluid alteration zones. Compositional analyses provided insight into fluid interactions, fluid alterations and chemical signatures across the fault. In addition to sampling key fault facies and damage zone structures, a compositional "scanline" was performed at one field locality to sample a transect perpendicular to strike of the fault core to determine any mineralogical shift across the fault core.

Subsurface Modeling

Because this project is motivated by technical challenges related to the storage of CO₂ and for the oil and natural gas industry, it was important to produce results that focus on the both the surface and subsurface geometry of the fault and the impacts of faults within potential sealing caprock and reservoir units. Subsurface contouring and restoration of eroded units in San Rafael Swell and other similar structures has been done by Barton (2011). Data for this project included publically available files and locations for drill-holes and wells, depth of formation tops, well-site mud logs, wireline logs, pre-drilling and post-drilling well reports, and core data from Utah Division of Oil, Gas, and Mining downloaded from <http://oilgas.ogm.utah.gov> (Appendix A). Data was input into

IHS Petra, an industry-oriented software package designed for oil and gas exploration. Formation top depths for wells were loaded for 675 wells for all available tops available within Grand, Emery and Wayne counties in Utah. Scanned paper wireline logs and well reports were used to verify formation top depths for control wells throughout the field area. Selected paper wireline logs were digitized to provide insight into the log response for various formations of interest and to make petrophysical interpretations about the formations.

Subsurface models provide an excellent framework for the incorporation of detailed fault maps and the integration of fault zone characteristics into a working fault model. Formation top data were gridded to create structural contour maps of various formations at depth. These grids were then input into TrapTester, a program developed by Badley's Geoscience for fault mapping and modeling of fault juxtaposition and sealing properties. These models were developed to make predictions about the fault properties and characteristics of the Iron Wash fault in the subsurface, that were ultimately used to discuss and constrain the ability of the fault to behave as a seal to fluids. Further, the software allows us to make predictions about the height of a CO₂ column that the fault could reasonably support during injection. Details of the model design and input are discussed in later sections.

Geophysical Surveys

In the process of developing this project, several geophysical surveying methods were attempted to try to image the fault zone. Resistivity, induced potential, and active-source seismic surveys were conducted using standard methodologies. The results of

these surveys were inconclusive and therefore not included in the main text of this thesis, however, the raw data and descriptions of the methods used are included in Appendix B.

RESULTS

Overview

The Iron Wash fault study area is located on the eastern side of the San Rafael Swell and in the western section of the San Rafael Desert (Figure 5). The Iron Wash fault strikes $\sim 310^\circ$ and dips steeply (67° - 84°) to the northeast, has a slightly listric fault trace and a maximum stratigraphic offset of ~ 120 m. The fault is oriented perpendicular to the San Rafael Swell where bedding strikes $\sim 45^\circ$ and dips moderately (30° - 40°) to the southeast.

We present geologic maps produced of the Iron Wash fault zone and results from kinematic analysis of the fault (map locations in Figure 6). Measured fault throw profiles of the fault zone are used to determine the distribution of slip along the trace of the fault, to characterize the transfer of throw across fault relays, and to describe the role of fault related folding in this fault zone. We present results on the measured thickness of the fault zone and the fault damage zone. We describe and characterize the structure of two fault relay zones and one fault lens and discuss the overall architecture of the fault zone and fault facies. We present evidence for the migration of fluids vertically and laterally through the fault zone. We present results of x-ray diffraction and petrographic analysis of samples collected from the fault zone. Finally, we describe how we designed various models to reproduce the geometry of the fault and predict fault zone properties and sealing behavior.

The western side of the field area (Figure 6, Areas A and B) consists of a horst and graben complex adjacent to the monocline and a widely distributed fault and fracture network seen in the dipping beds of the Navajo Sandstone and Kayenta Formation along the monocline limb (see Figure 6 for locations; Figure 11). We present data on the nature of the fault geometry as it intersects the monocline to characterize the fault zone thickness, architecture, and strain distribution to characterize the interaction of the Iron Wash fault with the monocline.

The central part of the field area (Figure 6, Area C) contains numerous fault relay structures, one large (~1 km long) fault lens, several 10- to 50-m long fault lenses and extensive fault-related folds (see Figure 6 for locations; Figures 12 and 13). Two examples of meso-scale (10^2 m wide) fault relay zones are exposed (in Area B), a soft- and a hard-linked fault relay (Figure 12). These fault relays are zones in which the throw transferred in a north-stepping (or right stepping) direction from one discrete segment of the fault to another and the associated fault and fracture networks are exposed within different structural levels. We present data on the nature of the fracture and fault distribution, strain transfer, linkage and propagation features, thickness and architecture to characterize the internal structure of fault relays and lenses.

In the far eastern part of the study area (Figure 6, Area D), the Iron Wash fault is a relatively narrow zone of slip accommodation that gradually loses throw to the southeast (Figure 14). On the western side of the monocline, it becomes increasingly difficult to track individual segments of the fault zone or to identify the total amount of slip accommodated by the fault and fracture network as a whole. Due to the nature of the fault

zone and exposure in these segments, the focus of this study is the more structurally complex central areas of the fault zone.

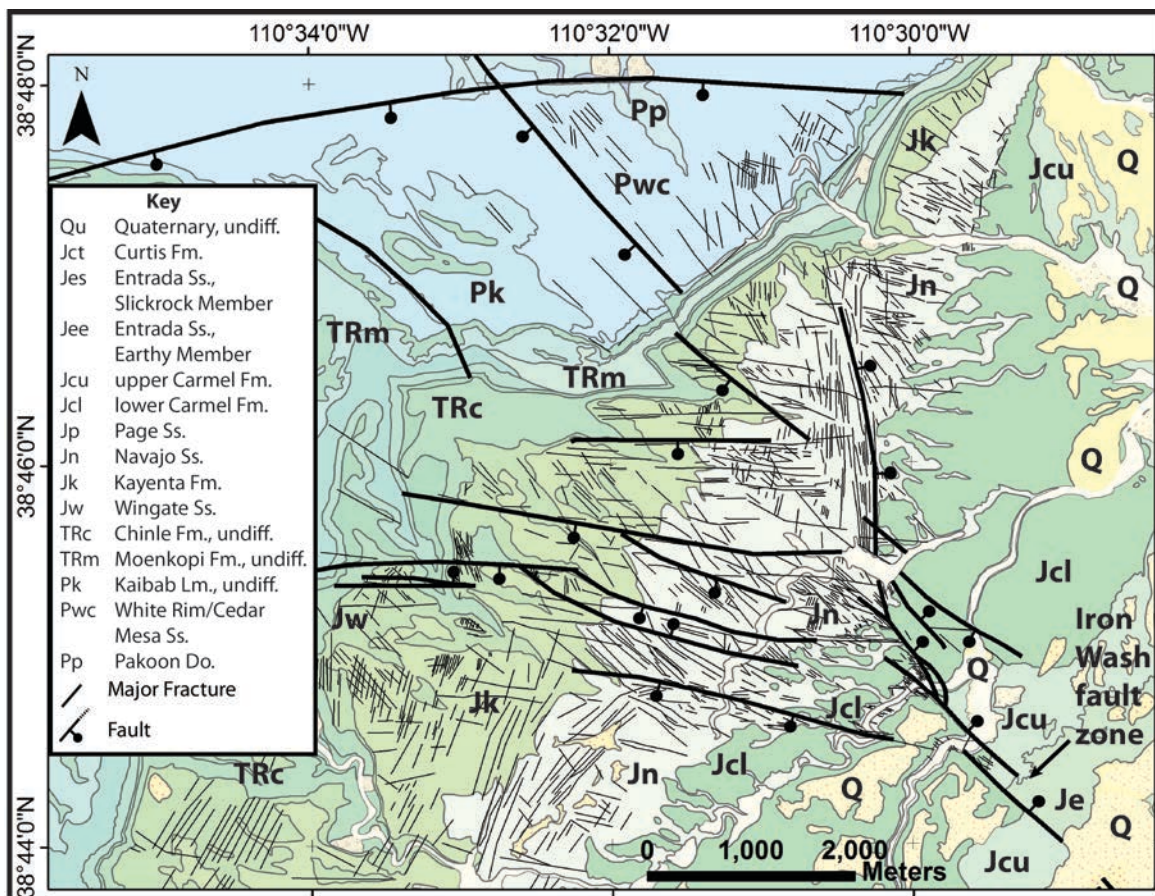


Figure 11. Geologic map of the Iron Wash fault zone (Area A) at the intersection of the San Rafael monocline (location in Figure 6) (modified from Doelling et al., in review).

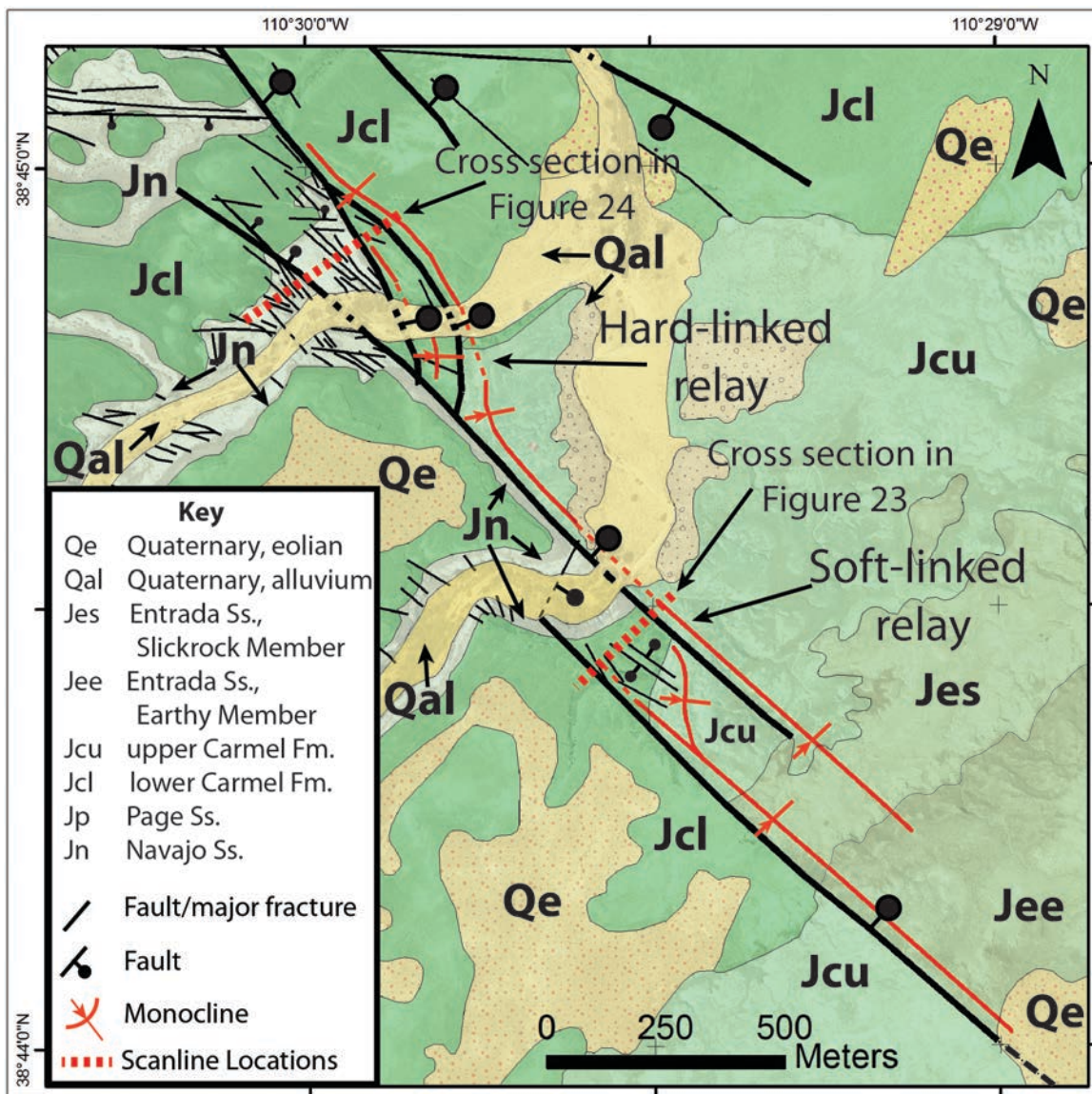


Figure 12. Geologic map of the Iron Wash fault zone (Area B) showing hard- and soft-linked relay zones (location in Figure 6) (modified from Doelling et al., in review).

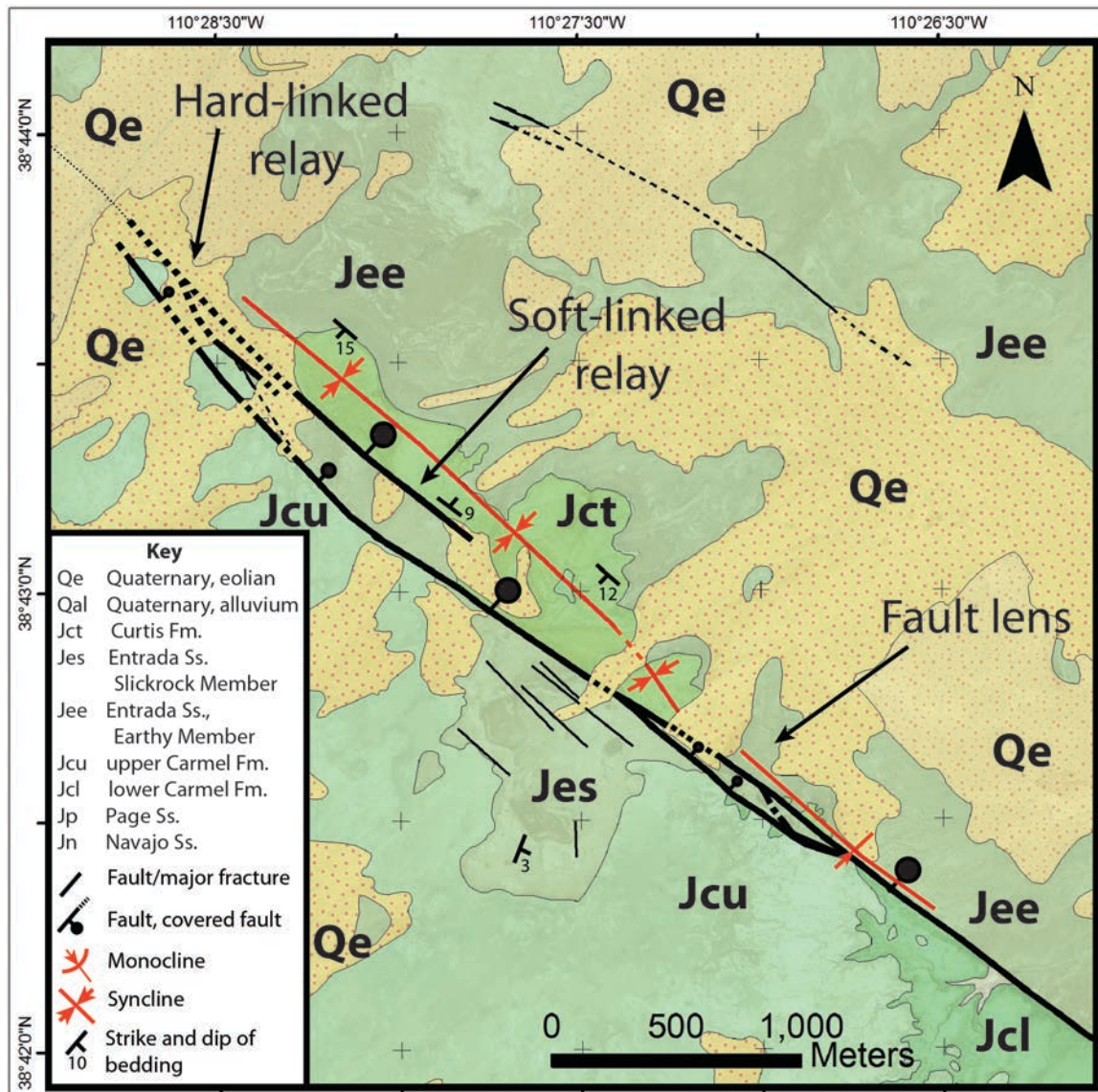


Figure 13. Geologic map of the Iron Wash fault zone (Area C) showing hard-linked relay and fault lenses (location in Figure 6) (modified from Doelling et al., in review).

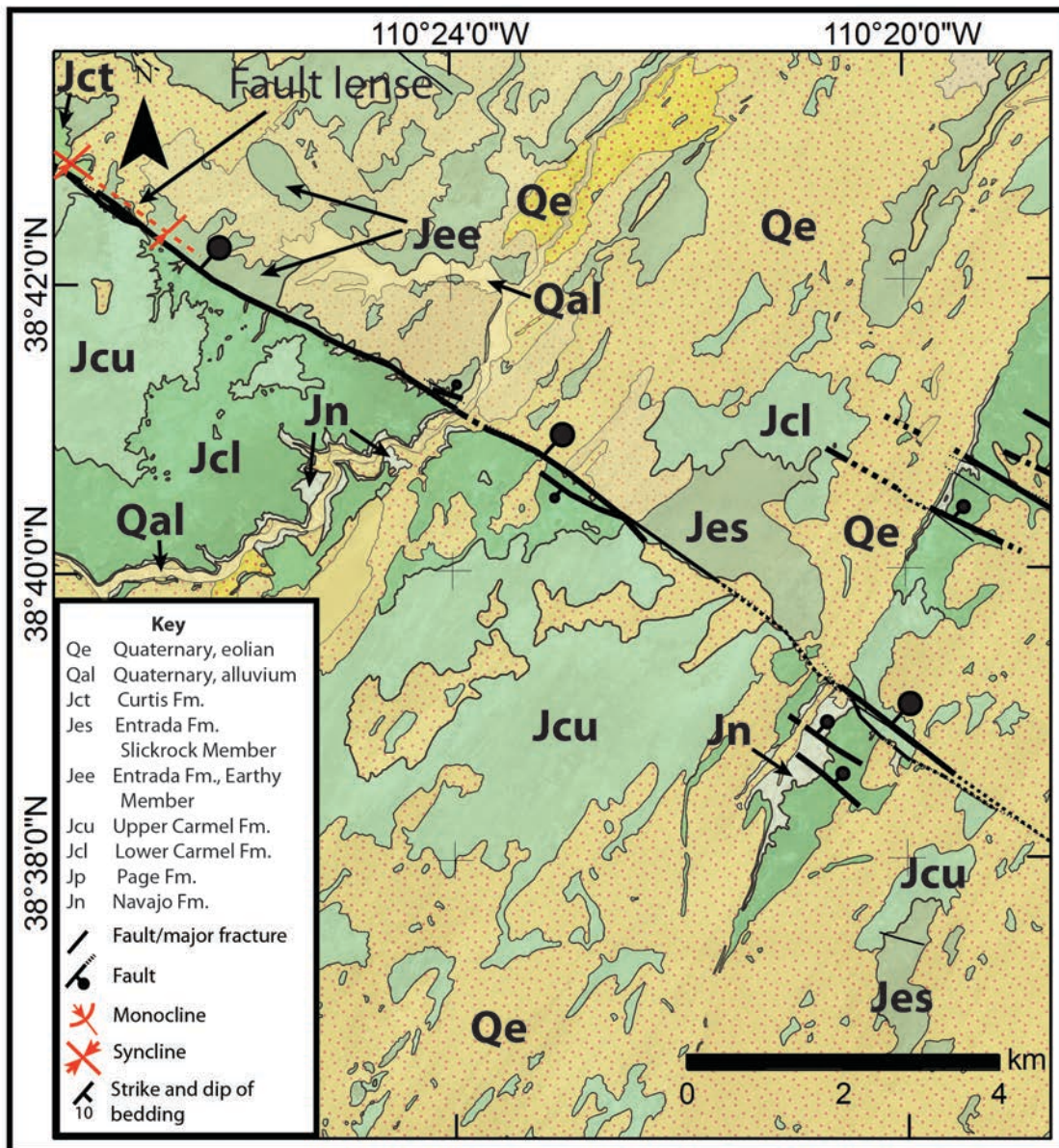


Figure 14. Geologic map of the Iron Wash fault zone (Area D) showing the eastern tip of the fault (location in Figure 6) (modified from Doelling et al., in review).

Strain Distribution

Slip along the fault is characterized to better understand the strain that the fault accommodated and to use this information to analyze the stress field in which the fault formed. We hypothesize that the Iron Wash fault has formed in both the stress fields of the Colorado Plateau and the Basin & Range and these data are used to test this hypothesis.

Where the main strand of the Iron Wash fault intersects the dipping beds of the monocline (Figure 6, Area A), the main strand of the Iron Wash fault tips out and we observe a wide zone of associated faulting in the limb of the monocline (Figure 11). Here we see the intersection of the northwest-striking fault zone (Figure 15a) with the southeast-dipping monocline (Figure 15b) and the beginning of a widely dispersed fault zone at the monocline front (Figure 11). This dispersed fault zone is composed of numerous small-throw faults (<10 m throw) that generally strike east-west (Figure 15c) or north-south (Figure 15d), orthogonal to the main strand of the fault (Figures 11 and 15). Between these small faults a damage zone that consists of well-developed network of deformation bands is exposed and most apparent within the porous sandstones of the Navajo Formation.

Slip vectors were measured on exposed principal slip surfaces with slickenlines located within the fault core away from the San Rafael monocline (Areas B and C, Figure 16a). A set of primary slip planes strike 310° to 325° and dip steeply (72° - 86°) to the southwest and northeast (Figure 16a). A set of secondary slip planes strike 320° to 350° and dip moderately (20° - 42°) to the west and southwest (Figure 16a). A third minor set of slip planes strike 320° and dips shallowly ($\sim 6^{\circ}$) to the northeast. Slip data show a

dominate dip-slip motion on the primary slip planes and oblique-slip motion on other slip planes with a component of left-lateral motion. The amount of oblique slip varies from a minor component to an almost pure strike-slip motion on some planes (Figure 16a).

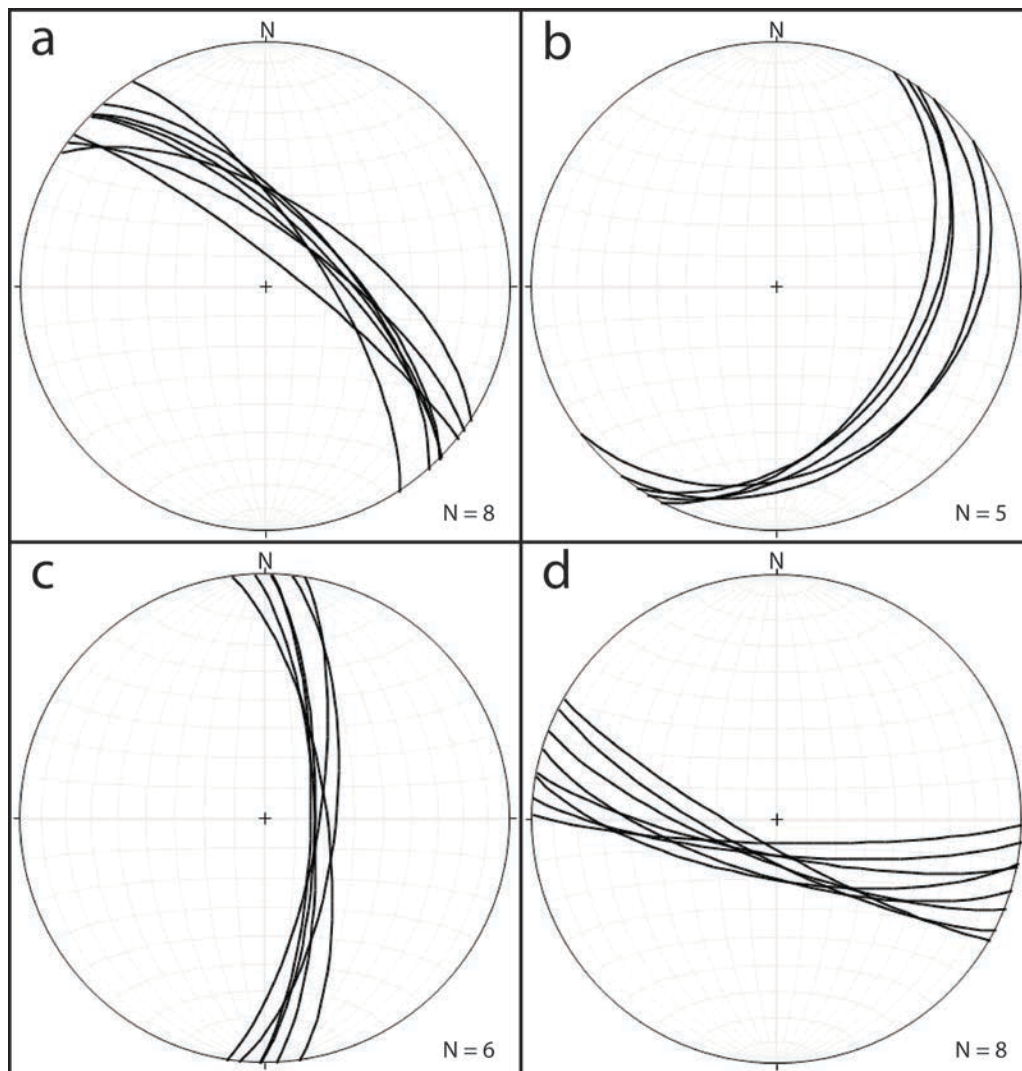


Figure 15. Equal-area, lower hemisphere stereonet projections of faults in the western section of the study area (Area A). Data are from a) main strands of the Iron Wash fault, b) orientation of bedding of the San Rafael monocline, and c/d) small-throw faults (<5 m throw) along the front of the monocline as the main strand of the Iron Wash fault loses throw, see text for descriptions.

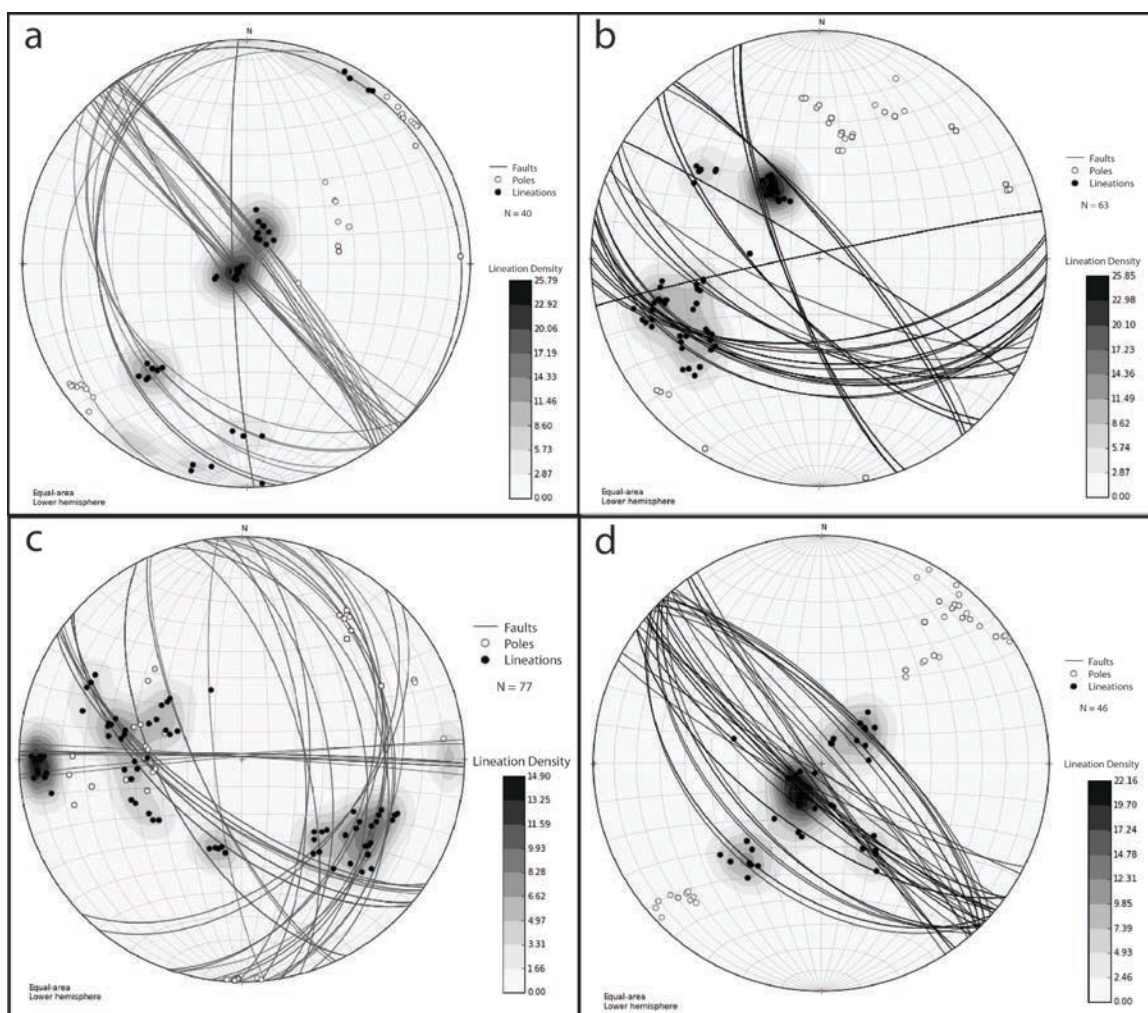


Figure 16. Equal-area, lower hemisphere stereonet projections of planes, poles to planes and lineations of the Iron Wash fault zone. Data are from a) main strand east of the San Rafael monocline (Areas C and D), b) fault strands within the San Rafael monocline (Area A), c) faults within the soft-linked relay (Area B), and d) main strands of the fault surrounding the fault lens (Area C).

Slip vectors were measured on exposed principal slip surfaces with slickenlines located in the fault core as the fault adjacent to and within the San Rafael monocline (Area A, Figure 16b). The main strand of the fault strikes $\sim 320^\circ$ and dips steeply ($\sim 80^\circ$) to the northeast (Figure 16b). The other half of an assumed conjugate fault set to the primary plane strikes $\sim 340^\circ$ and dips steeply ($\sim 75^\circ$) to the southwest. Another set of

secondary slip planes strike 260° to 300° and dip moderately (47° - 71°) to the southwest (Figure 16b). Slip data show a dominate oblique-slip motion in this area. The primary planes that dip steeply have both a left and right-lateral oblique component depending on the dip of the fault. The secondary planes have an oblique-slip motion with right-lateral motion. No faults in this area show dominantly dip-slip motion (Figure 16b).

Fault Throw

Throw on the fault was characterized by measuring stratigraphic offset of the rocks in the hanging wall and footwall at 92 localities over 25-km strike distance along the fault where exposures allowed. Total throw on the fault measured away from the fault core damage zones was determined first (Figure 17). Secondly, we measured throw localized on the primary slip surface (within the fault core) not including throw accommodated by damage zones or fault-related monoclines (Figure 17). We see that throughout the fault zone, total stratigraphic offset away from the fault core is consistently greater than throw measured at the fault core (Figure 17). The reduced throw at the fault core is a result of additional stratigraphic offset accommodated by monoclines adjacent to the fault zone with amplitudes up to ~ 20 m (Figure 17). For the remainder of this study and when conducting calculations, the term throw is used to denote total throw of the fault zone.

Near the San Rafael monocline (Figure 6, Area A), the Iron Wash fault consists of multiple fault segments and total throw is determined by summing individual fault throw across each of these segments. The throw profiles (Figure 18a) allow for the determination of throw gradients (or the distribution of throw perpendicular to strike) to

determine where throw gradients are relatively low (i.e. more distributed throw) or higher to help draw conclusions about the nature of faulting. Fault zone thickness was determined at 40 locations along the fault (Figure 18a) and will be discussed in later sections.

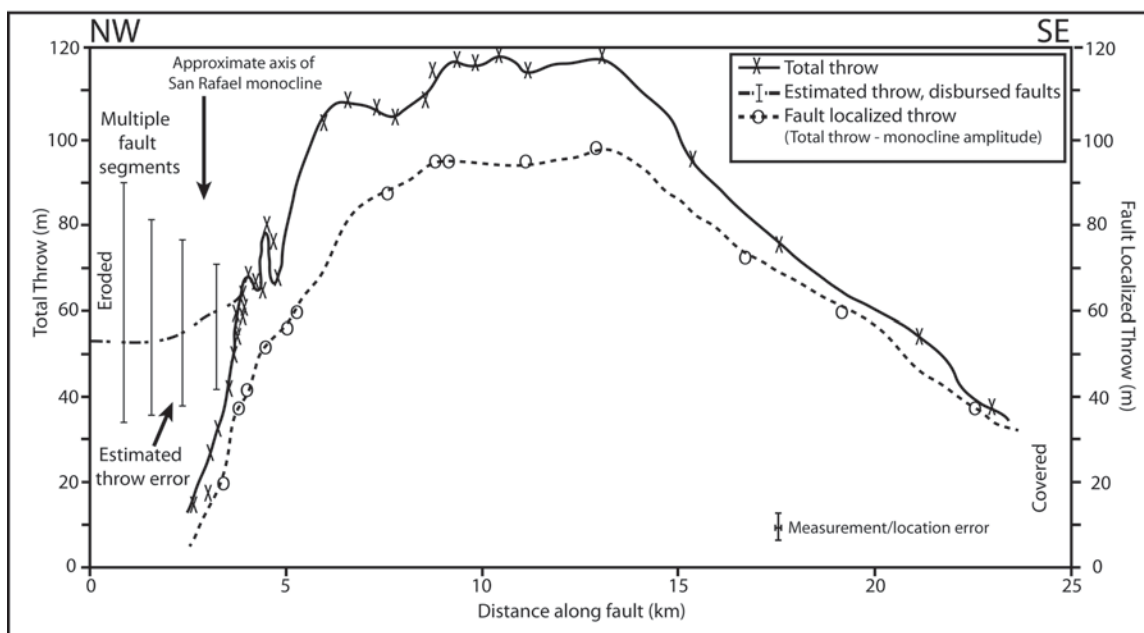


Figure 17. Fault throw profile of the Iron Wash fault zone. Solid line showing total throw accommodated by the fault measured as total stratigraphic offset away from the fault zone, dashed line showing throw accommodated by the primary slip surface measured as throw accommodated by the damage zone and fault monoclines subtracted from the total throw. Vertical bars on left side of figure represent measurement error associated with measuring the throw on dispersed faults in the monocline (Area A).

The throw profile for the fault shows that the ~25 km long fault has a maximum throw of ~120 m (Figure 18a) over a broad ~7 km strike distance slightly skewed to the northwest end of the fault zone. In agreement with observations of other fault systems (e.g., Kim and Sanderson, 2005), the maximum throw lies at approximately the center of

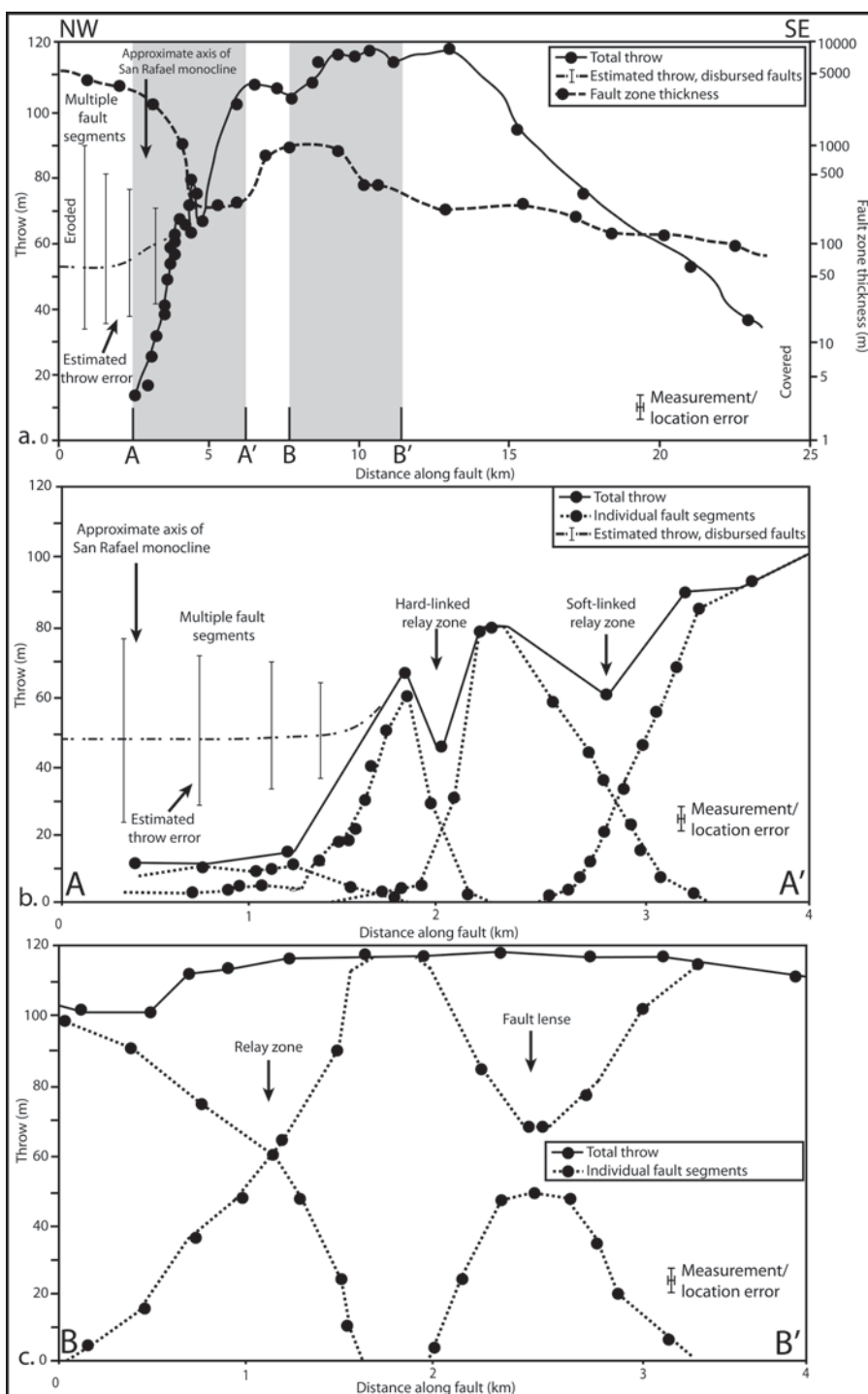


Figure 18. Fault throw and thickness profiles for the Iron Wash fault zone. a) Fault throw and thickness profile of the Iron Wash fault zone, b) fault throw profile of the Iron Wash fault zone from A-A' shown in figure 18a, and c) fault throw profile of the Iron Wash fault zone from B-B' shown in figure 18a. Vertical bars on left side of figures represent measurement error associated with measuring the throw on dispersed faults in the monocline (Area A).

the fault trace. Throw gradually increases from the eastern fault tip to a maximum point on the fault from 9-13 km along the fault (Figure 18a) and then loses throw sharply as the fault approaches the San Rafael monocline. As the fault intersects the steeply dipping beds of the monocline, throw is dispersed across many small-throw faults, but based on field observations and mapping, it appears that the fault likely accommodates similar (or less) total throw as the primary segments of the Iron Wash fault, or somewhere between ~40-90 m of cumulative throw (Figure 18a). West of the monocline, throw is accommodated by a relatively discrete fault zone through the interior of the San Rafael Swell where the fault has an opposite sense of slip to the west of the monocline and throw is ~40-100 m, as measured in the Cedar Mesa Formation (Figure 11).

Because one of the major subjects of this research is to characterize fault relay zones and fault lenses, detailed throw profiles were conducted for the far western segment of the fault containing two fault relays (Area B, Figure 18b) and for the segment containing one fault relay and one fault lens (Area C, Figure 18c). In the area of the fault relays (Area B, Figure 12) throw generally decreases to the northwest, and it appears that although throw decreases slightly across the relay zones, all throw is transferred by each of the relays (Figure 18b). Within the relays however, the throw profile shows that the relays are areas of decreased throw by about ~20 m in each case. As one fault segment dies out and the next segment begins, these are areas of high throw gradient relative to other areas of the fault. The throw gradients here are as high as 70 m of slip accumulated in a fault trace distance of ~300 m, or ~0.23 m per meter of fault length (Figure 18b).

In the central segments of the fault containing a relay zone and a fault lens (Area C, Figure 13) throw is transferred almost completely across the relay and lens (Figure

18c). Here the relay does not appear to be a zone of decreased throw as other examples and the throw gradients are much lower, with gradients as high as 110 m of slip accumulated in a fault trace of ~1500 m, or ~0.073 m per meter of fault length. The throw profile across the fault lens shows that each of the fault strands bounding the lens accommodate approximately half of the total cumulative throw and that strain within the lens does not seem to reduce the total slip on the fault relative to adjacent segments (Figure 18c). Throw gradients on the segments bounding the fault lens are ~45 m of slip accumulated in a fault trace of ~250 m, or ~0.18 m per meter of fault length.

Fault Zone Thickness

Fault zone thickness (refer to terminology and definitions section for clarification) was measured at 40 locations along the fault and examples of these locations can be seen in Figures 11, 12, and 13 (see Figure 6 for locations). In the far eastern segment of the fault (Area D), the fault is generally between 70-200 m wide and contains small folds (5 m to 30 m wide) and narrow damage zones (generally <10 m wide) (Figure 18a). In the central segments of the fault (Area C), where throw is at its maximum, the fault zone is 250-500 m wide (Figure 18a). Along strike to the northeast (Area B) the hard- and soft-linked relays and fault-related folding result in a fault zone between 200-500 m wide (Figure 18a). Where the fault intersects the San Rafael monocline (Area A) throw is dispersed among many small-throw faults (10¹ m's of throw). Throw is transferred from a relatively discrete fault zone (<250 m wide) to a much wider zone (up to ~5000 m) (Figures 11 and 18a). This zone consists of ~10 mapped faults with >10 m of throw and a complex network of fractures contained within the fault zone. This wide zone might be

termed a damage zone, fault relay, or even a large fault splay amplified by the presence of the monocline and is interpreted as a zone of strain dispersal in the form of a very widely spaced small-throw faults each accommodating generally <10 m total throw (Figure 18a).

We plot fault throw as a proxy for fault displacement to examine fault zone thickness as a function of displacement and compare the Iron Wash fault to other published work (Figure 19). The Iron Wash fault zone falls within the previously observed ranges of fault displacement to thickness ratio (D:T ratios) by previous workers (Figure 19). Most studies of fault-related rocks, fault zones, and relay zones show D:T ratios ranging from 0.01 to 1000. The features plotted for the Iron Wash fault include relay zones, fault tips near relays, small faults within relays, the monocline segment of the fault and main segments of the fault and show D:T ratios ranging from 0.01 to 10 (Figure 19). The main segments of the fault and small-displacement (<5 m throw) faults measured around the main strand have D:T ratios ranging from 0.1 to 10. Fault zones where relays are overlapping have D:T ratios of 0.1 to 2.0. The two features that plotted with comparably thicker fault zone for a given thickness (lower D:T ratio) are the segment of the fault within the San Rafael monocline and fault tips near relay zones where D:T ratios were 0.01 to 0.06.

Fault damage zone thickness was characterized using fracture density scanlines away from the fault core (Figure 20). We did not include any fractures in the fault core in these scanlines, but only fractures in the damage zone and host rock. Scanlines data was

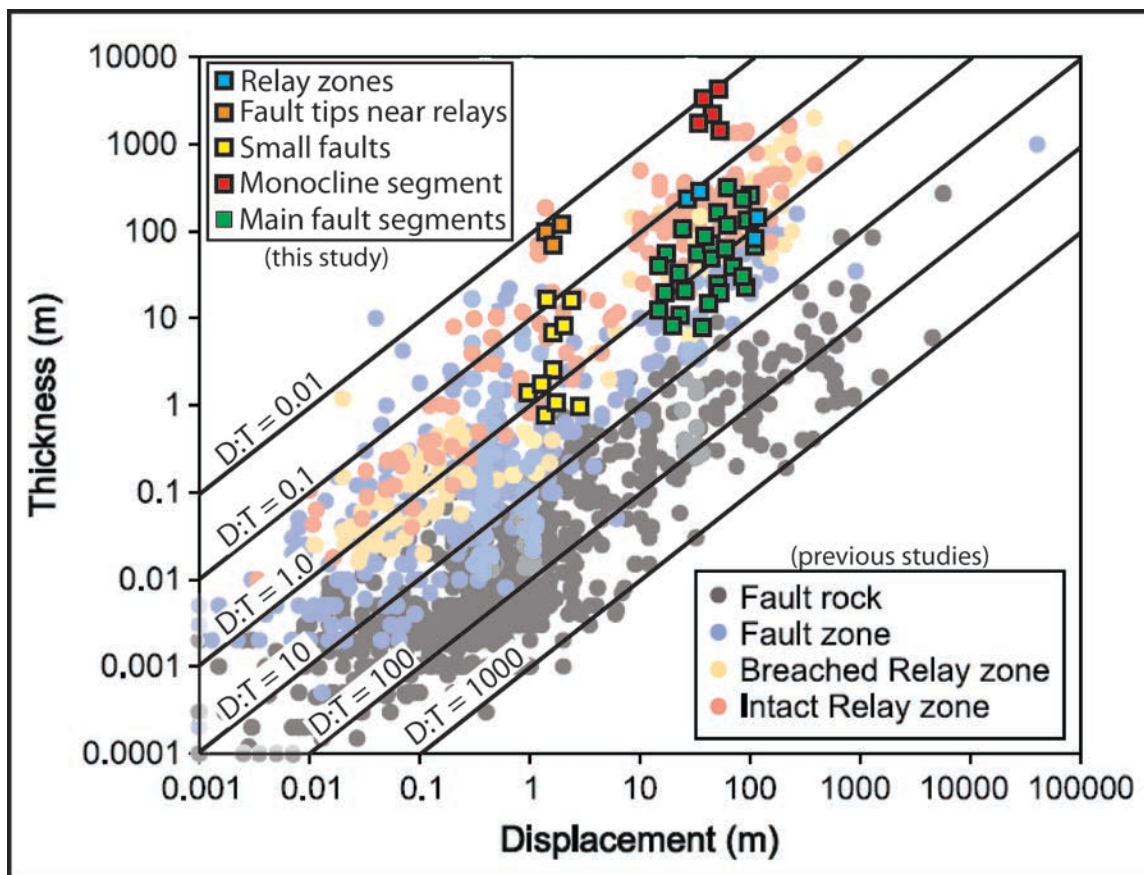


Figure 19. Plot of fault thickness and displacement for the Iron Wash fault zone. Data from previous studies are pale, for comparison with data from this study (modified from Childs et al., 2009 and references therein).

acquired as far as exposures would allow or until 50 m away from the main slip surface. Scanline data was collected where exposures allowed, but an attempt was made to reduce variables between scanlines whenever possible. All scanlines were acquired in areas of the fault where no major secondary structures such as fault relays or fault lenses were present and the throw on the fault was 50-85 m. An attempt was made to target beds with similar characteristics (thickness, lithology, facies), but in some cases this was not possible (see Figure 20 for bedding descriptions). Fracture density scanline data was collected in the hanging wall and footwall for the Earthy and Slickrock Members of the

Entrada Formation, the upper and lower Carmel Formations, and in the footwall of the Navajo Sandstone (Figure 20). No scanline data was collected in a hanging wall exposure of the fault for Navajo Formation because of lack of good exposure with adequate throw.

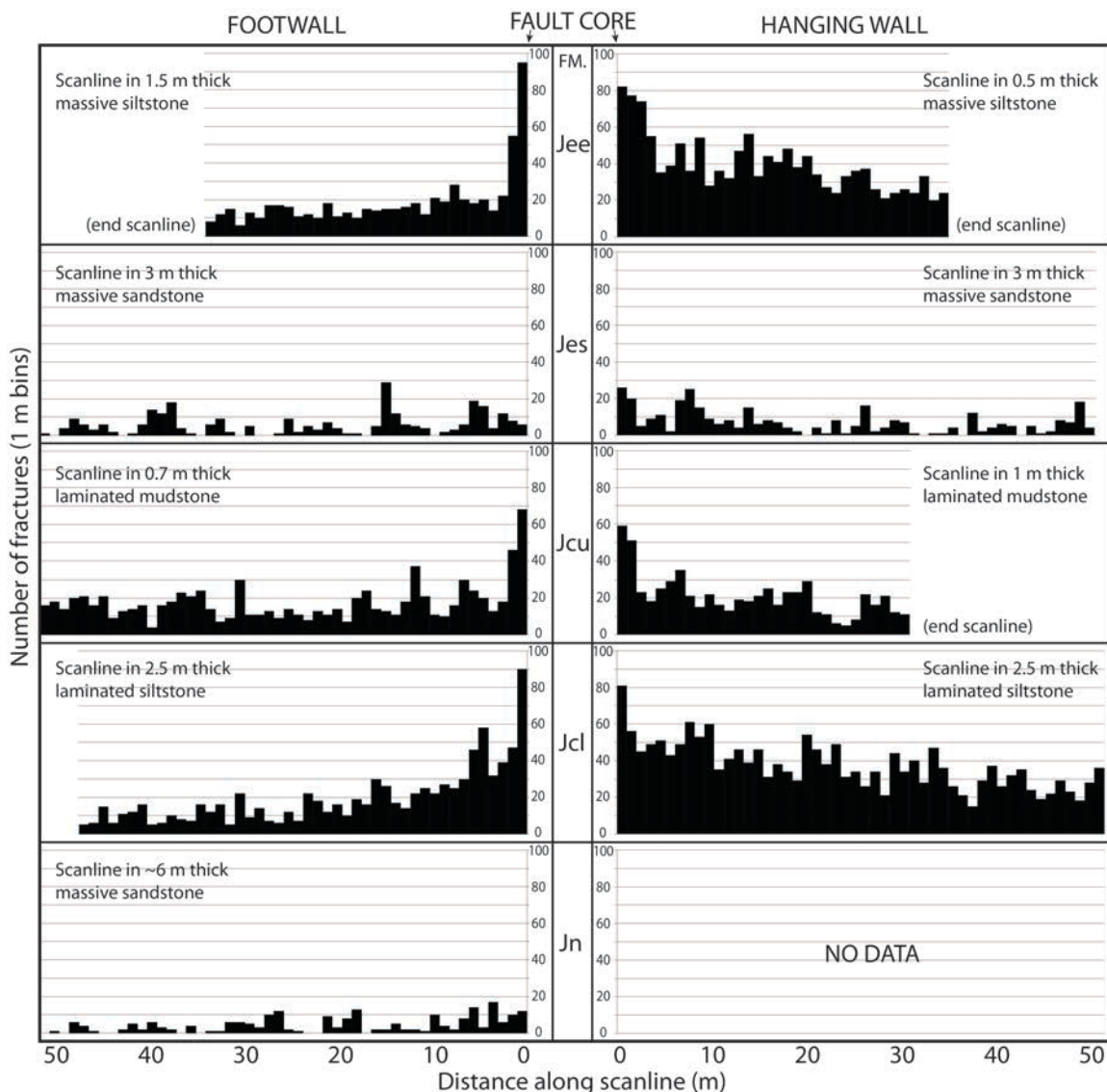


Figure 20. Fracture density scanlines in hanging wall and footwall damage zones of the Iron Wash fault zone. Scanlines in all units from the Jn, Navajo Sandstone; Jcl, lower Carmel Formation; Jcu, upper Carmel Formation; Jes, Slickrock Member of the Entrada Formation; Jee, Earthy Member of the Entrada Formation. Scanlines all plot the fault core at 0 m. Fracture densities are in number of fractures per 1 m bins. Lithologic descriptions are for each of the scanlines.

Scanline data show that the Slickrock Member of the Entrada Formation and the Navajo Formation have the lowest concentration of fracturing and the lower Carmel has the highest overall fracturing (Figure 20). Scanline data show a general trend of increased fracturing in the hanging wall compared to the footwall (Figure 20). Hanging wall fracture density shows a wider damage zone than the footwall damage zone in some cases (Figure 20). This relationship is most apparent in the Earthy Member of the Entrada Formation and the lower Carmel Formation (Figure 20). The Slickrock Member of the Entrada Formation and the upper Carmel Formation do not clearly show one side of the fault having a wider damage zone (Figure 20). The fine-grained lithologies of the Earthy Member of the Entrada Formation and the upper and lower Carmel Formations have wider damage zones than the coarser-grained Slickrock Member of the Entrada Formation and the Navajo Sandstone (Figure 20).

Relay Zone and Fault Lens Structure

General Structure

There are four exposures of fault relay zones where fault throw is transferred from one segment of the fault to another across steps up to ~230 m wide. The two fault relay zones examined in this study are: 1) a soft-linked relay that transfers ~65-80 m of throw across a ~200 m wide relay zone that has no significant faults linking the strands and 2) a hard-linked relay that transfers ~50- 80 m of throw across a ~175 m wide relay zone that is structurally connected by at least two significant fault segments in direct linkage with the south segment (Zone A, Figures 12 and 18b). In the soft-linked relay (Figure 12), the south strand of the fault loses throw to the northwest and the north strand gains throw to

the northwest. The relay zone creates a relay ramp that strikes north-northeast and dips east at 5-33°. Monoclines lie parallel to strike in the hanging walls of both main strands of the fault, and within the relay zone in the footwall of the north strand as it loses throw to the southeast. In the hard-linked relay (Figure 12), the south strand of the fault loses throw to the northwest and the north strand gains throw to the northwest. The relay zone creates a subtle ramp similar to that found in the soft-linked relay, but is truncated by two strands of the north fault deflect towards the southern segment and intersect the fault obliquely. Folds are observed in the hanging wall on the north strand of the fault, north of the relay and is continuous across the relay zone associated with both northern strands and along the southern strand (Figure 12).

Fault-bounded lenses range in dimensions from 5 m long and 3 m wide up to 1 km long and 150 m wide, where throw is accommodated by more than one primary segment of the fault (Figure 18b and c). Fault lenses <~10m long are referred to in this text as fault blocks and are commonly rotated within the fault core bounded by the main fault and smaller synthetic and antithetic faults (Figure 21a). The largest fault lens observed in the field area is in the southeastern segment of the fault (Figure 13) and is approximately 1 km long and up to 150 m wide. Although the nature of the deformation in this area makes determination of exact amount of throw on each segment of the fault difficult, it appears that throw is distributed approximately evenly between the fault segments (Figure 18c). Quaternary cover prevents the investigation of the exact point where the fault diverges into two segments on either end, but the interior of the fault lens was investigated to characterize kinematic indicators and fluid-related mineralization and alteration. This fault lens is the primary area of the fault where extensive oil staining is

present throughout almost the entire lens area. Oil staining is most intense between the fault strands and becomes less common away from the faults. Oil-stained rocks are present in other areas of the fault, but not to the extent found in this area, and will be discussed in later sections.

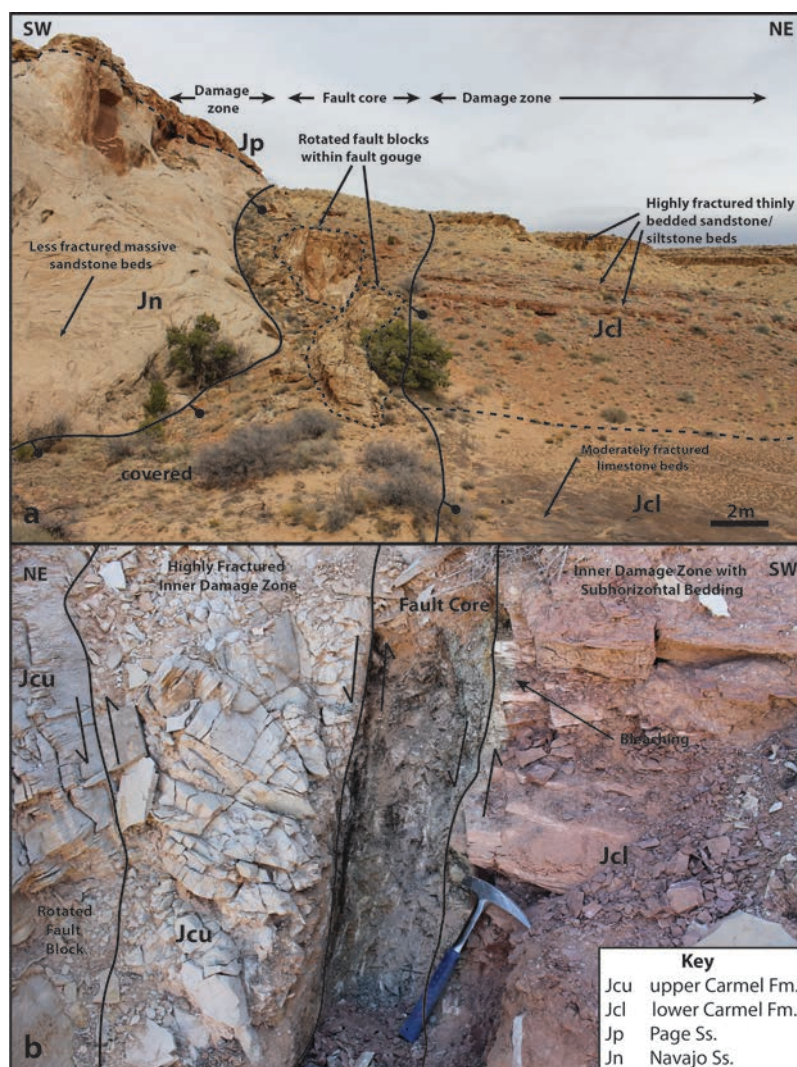


Figure 21. Annotated field photos of the fault core of the Iron Wash fault zone. a) View to the northwest along strike of the fault showing Navajo Formation juxtaposed against upper and lower Carmel Formation with multiple large rotated fault blocks incorporated into the fault core (Area B), and b) view along strike of vertical outcrop of the fault core showing highly deformed damage zone on either side of the fault core, and a fault gouge membrane (clay gouge) within the fault core (Area B).

Strain Distribution

Slip vectors were measured on exposed fault surfaces with slickenlines located in the soft-linked relay zone (Area B, Figure 12) excluding the main strands of the Iron Wash fault (Figure 16c). Three dominate fault orientations can be seen within the relay zone: a $\sim 305^\circ$ striking set that dips $\sim 60^\circ$ southwest and has right-lateral oblique-slip motion, a $\sim 270^\circ$ striking set that is nearly vertical and has almost pure strike-slip motion and, a generally north-south striking set that dips 30° - 65° to the east and has a right-lateral oblique-slip motion (Figure 16c).

Measured slip vectors within a fault lens (Area C, Figure 13) include measurements on the main strands of the Iron Wash fault and internal faults within the lens (Figure 16d). The southern strand of the fault lens is interpreted to be the principal fault based on field mapping, however both segments accommodate roughly equal portions of the total slip (Figure 18c). The $\sim 310^\circ$ striking faults dip 40° - 87° to the northeast and southwest and have a dominantly dip-slip component with a small amount of left-lateral oblique-slip motion on some faults that dip to the southwest (Figure 16d).

We observed a smaller fault set (~ 4 m maximum throw) oblique to the main strand of the Iron Wash fault. We characterize this small graben structure to understand the structural relationship of this smaller feature to the main strand of the fault. Slip vector data from the primary slip surfaces on this fault show that the fault propagated away from the main strand of the fault (Figure 22). This fault creates a small graben adjacent to the main fault that is ~ 20 m in length with ~ 4 m throw near the main fault losing throw away along strike to the northeast (Figure 22a). We interpret this exposure to be evidence of the propagation of small fault segments away from the main strand of

the fault zone (e.g. Roberts, 1996). We identify slip fanning or a change in the slip vector direction towards the fault tips (Figure 22c; Roberts, 1996). This type of structure may be related to the process development of fault lenses or fault blocks within the fault zone as small fault branch out from the main fault zone and incorporate intact blocks into the fault zone (Roberts, 1996).

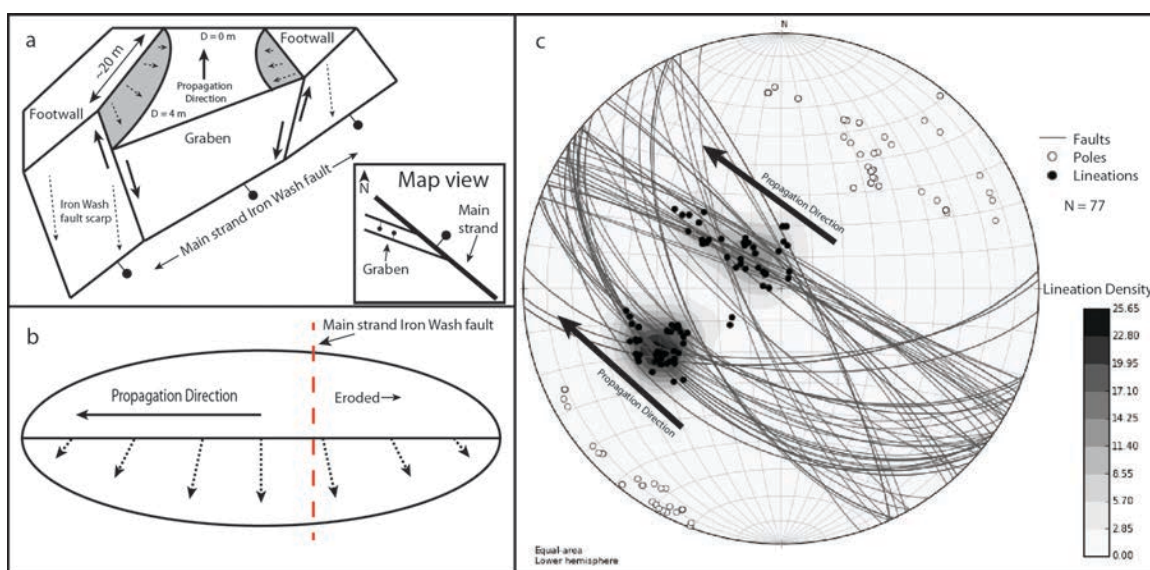


Figure 22. Summary of data and interpretation of small-throw fault (~4 m throw) adjacent to the main slip surface of the Iron Wash fault zone. a) Schematic representation of a small-throw (~4 m throw) fault propagating obliquely away from the principal slip surface of the Iron Wash fault (e.g. Roberts, 1996), b) schematic cross section of interpreted propagation of a single fault, c) slip vector data from the two fault creating the graben showing increasing rake angle towards the fault tips and the propagation direction. Small faults within the graben strike slightly more east-west than the main segments of the Iron Wash fault.

Strain analysis of slickenline data from the Iron Wash fault zone was performed using the methodology described by Krantz (1988) to determine the presence of three-dimensional strain within the fault zone and the changes in strain along strike (Figure 16).

Three-dimensional strain requires three or four fault sets to accommodate strain, whereas plain strain one or two fault sets (Reches, 1978; Aydin and Reches, 1982; Krantz, 1988, 1989). Aydin and Reches (1982) argue that multiple fault sets along the eastern flank of the San Rafael monocline formed contemporaneously based on crosscutting relationships and therefore formed during one stage of deformation. The western section of the fault experienced three-dimensional strain, specifically the segments of the fault that lie closer to the San Rafael Swell (Figure 16; Reches, 1978; Aydin and Reches, 1982; Krantz, 1988). Localized and perhaps more intense three-dimensional strain developed within relays zones adjacent to the San Rafael Swell. These data are interpreted to indicate that the Iron Wash fault has formed in two different strain fields (Reches, 1978; Krantz, 1988).

Fracture Distribution

In the central part of the fault zone (Area B, Figure 12), a fracture density scanline within the soft-linked relay shows how brittle deformation is associated with the relay zone and the four small-faults with throws ranging from 1.5-3.1 m (Figure 23). Fracture density in the lower Carmel Formation is generally higher within the relay zone than outside of the relay, and each of the small faults have related damage zones contributing an overall higher fracture density (Figure 23). Fracture density is greater on the north half of the relay, or on the half of the relay closer to the fault that accommodates the majority of the slip. Within the relay, faults and fractures are generally sub-parallel and orthogonal to the main fault strands and small-faults being both synthetic and antithetic to the main fault (Figures 12 and 23).

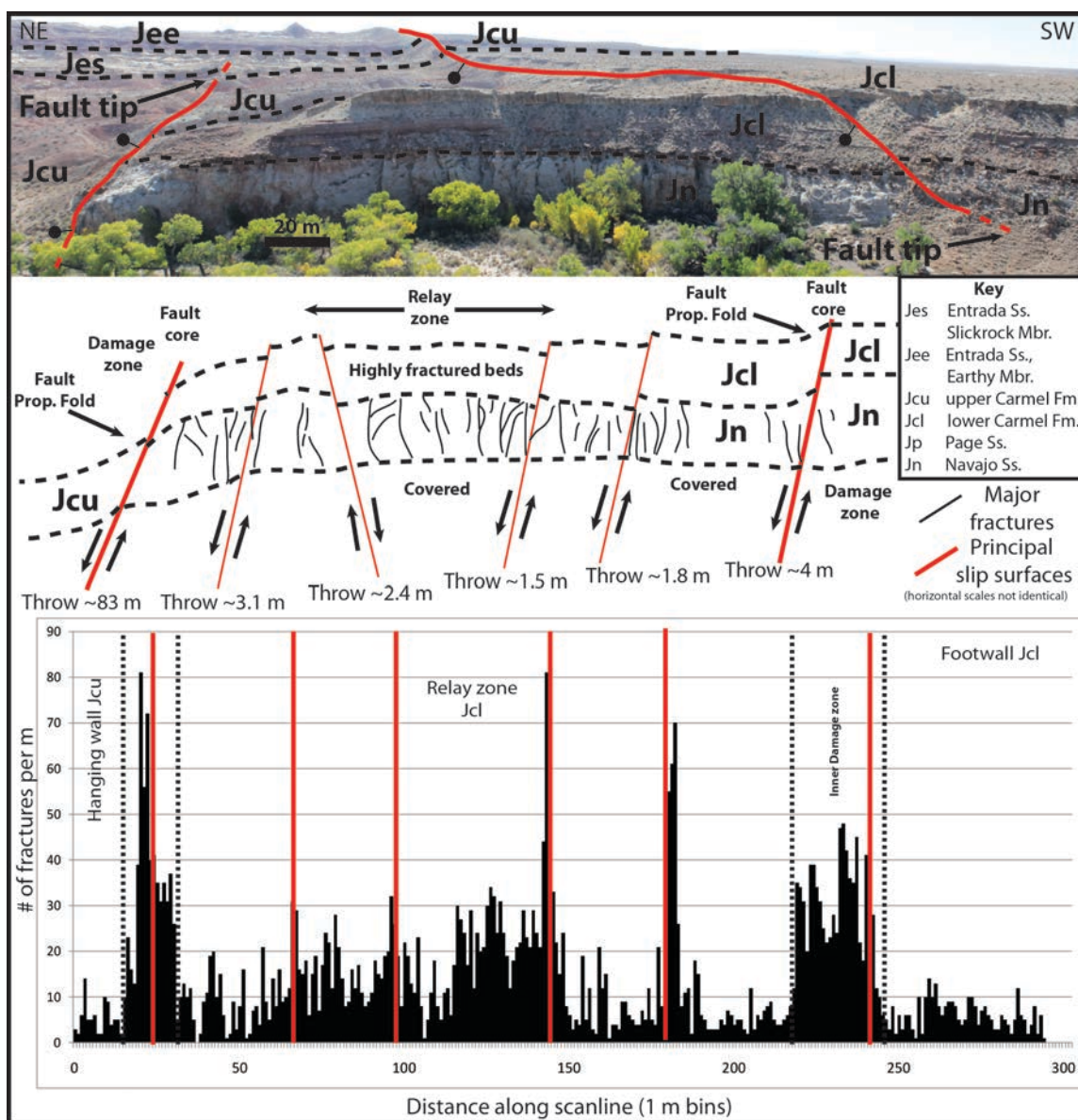


Figure 23. Summary of soft-linked relay zone (Area B). View to the southeast of soft-linked relay zone, schematic representation of the relay zone, and fracture density scanline across the relay zone (see Figure 12 for location) within the upper and lower Carmel formations.

Approximately one kilometer to the north of the soft-linked relay (Area B, Figure 12), a fracture density scanline within the hard-linked relay shows a relay zone that is more intact and less impacted by faulting than the soft-linked relay (Figure 24). Fracture

density in the Navajo Formation is similar both within the relay zone and outside of the relay. The damage zone in the footwall of the south fault, where throw is about two meters, is substantially wider and more deformed than in the footwall of the north strand, where throw is about 40 m (Figure 24). In this location the D:T ratio approaches 0.01 as a fault with 1-2 m of throw produces a damage zone thickness of 80-100 m (Figure 19).

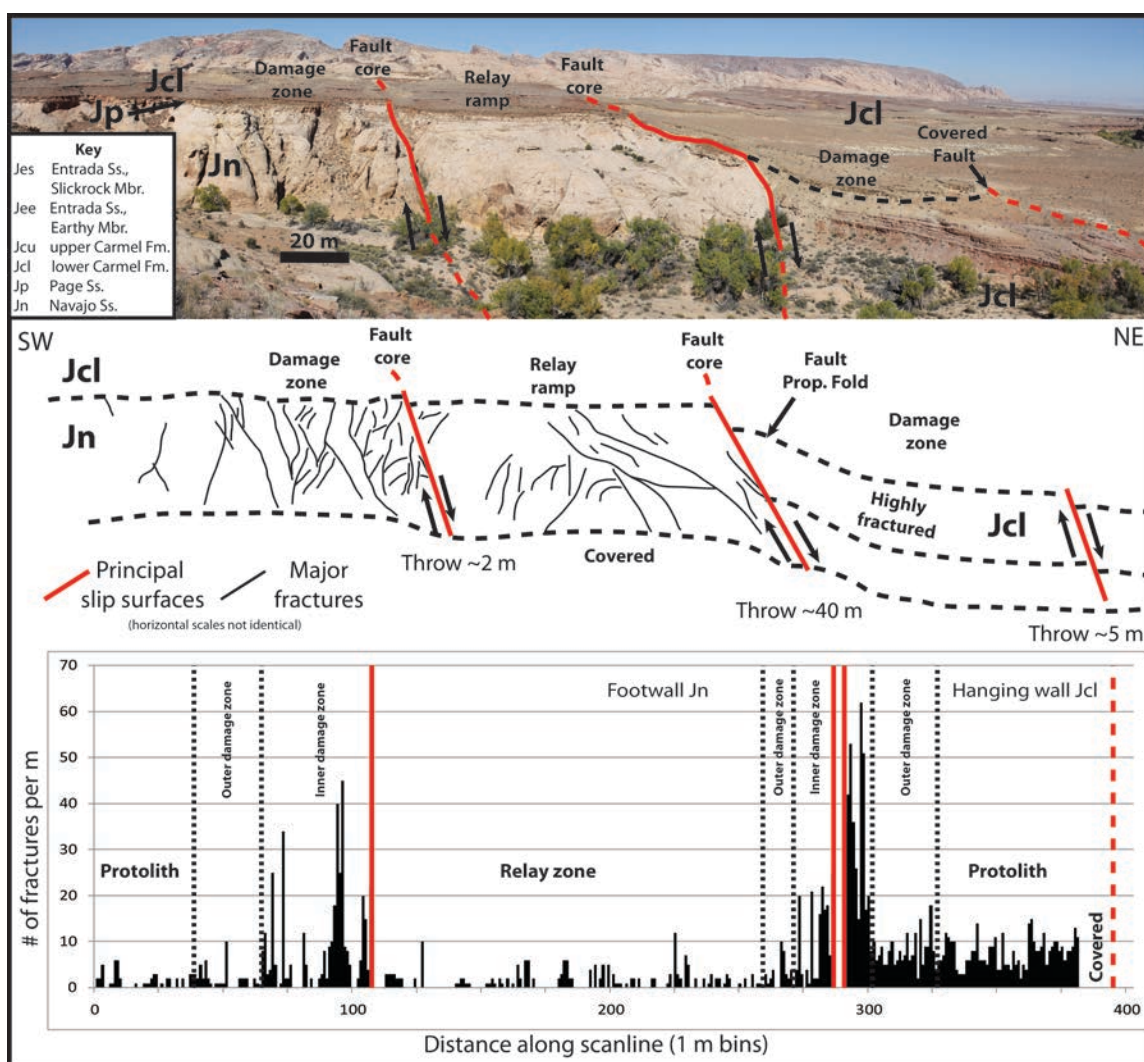


Figure 24. Summary of hard-linked relay zone (Area B). View to the northwest of hard-linked relay zone, schematic representation of the relay zone, and fracture density scanline across the relay zone (see Figure 12 for location) within the Navajo and lower Carmel formations.

Fracture orientations within the relay zones were measured to better characterize possible fluid conduits within the relay and any possible connectivity to underlying fracture networks or enhanced fracturing within the relay zone (Figure 25). Fractures outside of the relay zone have one dominate strike of $\sim 310^\circ$ (Figure 25a). Fractures within the relay show three distinct orientations with strikes of $\sim 305^\circ$, a second set striking between 340° and 60° with an mean strike of $\sim 10^\circ$, and a third set striking $\sim 90^\circ$ (Figure 25b). All fractures measured were at a high angle to bedding and generally had dips $>75^\circ$.

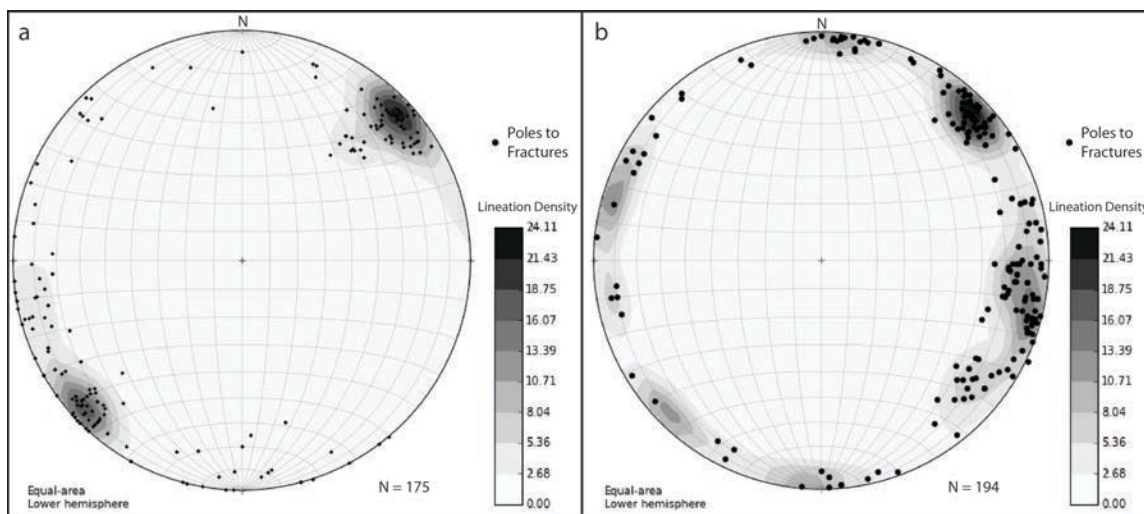


Figure 25. Equal-area, lower hemisphere stereonet projections with Kamb contour of poles to planes of fractures in the Iron Wash fault zone. a) Fractures outside of relay zones and b) fractures within soft-linked fault relay. Data comes from Area B within and around fault relays.

Fault-related Folding

In the central segment of the fault the hanging wall of the fault contains a ~ 600 m wide syncline with a hinge that lies ~ 200 m northeast of the fault core and with a fold

axis approximately parallel to strike of the fault (Figure 12). Based on available outcrops of the eroded syncline, we estimate that it has an amplitude of ~20-30 m and limbs that dip between 8°-19°.

Many fault-related monoclines are observed along the fault with axes that are parallel to sub-parallel to the main strand of the fault. They have the synclinal hinge of the monocline located 5-30 m from the fault core and with amplitudes ranging from 1-20 m (Figures 11, 12 and 13). Several exposures of cross-sectional views of these monoclines allows for investigation of the amplitude and internal structure of the folds (Figures 26 and 27). These monoclines accommodate throw that is distributed across the fold instead of being concentrated at the principal slip surface (Figure 26). Throw accommodated by the monoclines results in larger total stratigraphic separation away from the fault than the throw accommodated by the principal slip surface (Figures 17 and 27). These folds appear to be either draped over fault tips or dragged up against the fault and occur primarily on the hanging wall side of the master fault (Figure 27). Some of the folds have an orientation similar to the structure they are related to, for example, there is evidence of folding related to the formation of the fault relays (Figure 12). Folded rocks have dips of 10°-32° in the direction of the relay ramp to form a monocline that is constituting the relay ramp. These folds are observed to follow fault strands around relay structures (Figure 12); where the fault becomes two distinct strands that link to the next segment, each of the fault strands has a fold associated with it that parallels the fault until it becomes hard-linked. Although the area is quite complex and it is difficult to tell with certainty, it seems that the fold is continuous across the relay, possibly indicating that as throw is transferred by fault linkage, similarly, folding may be transferred as well. Cross-

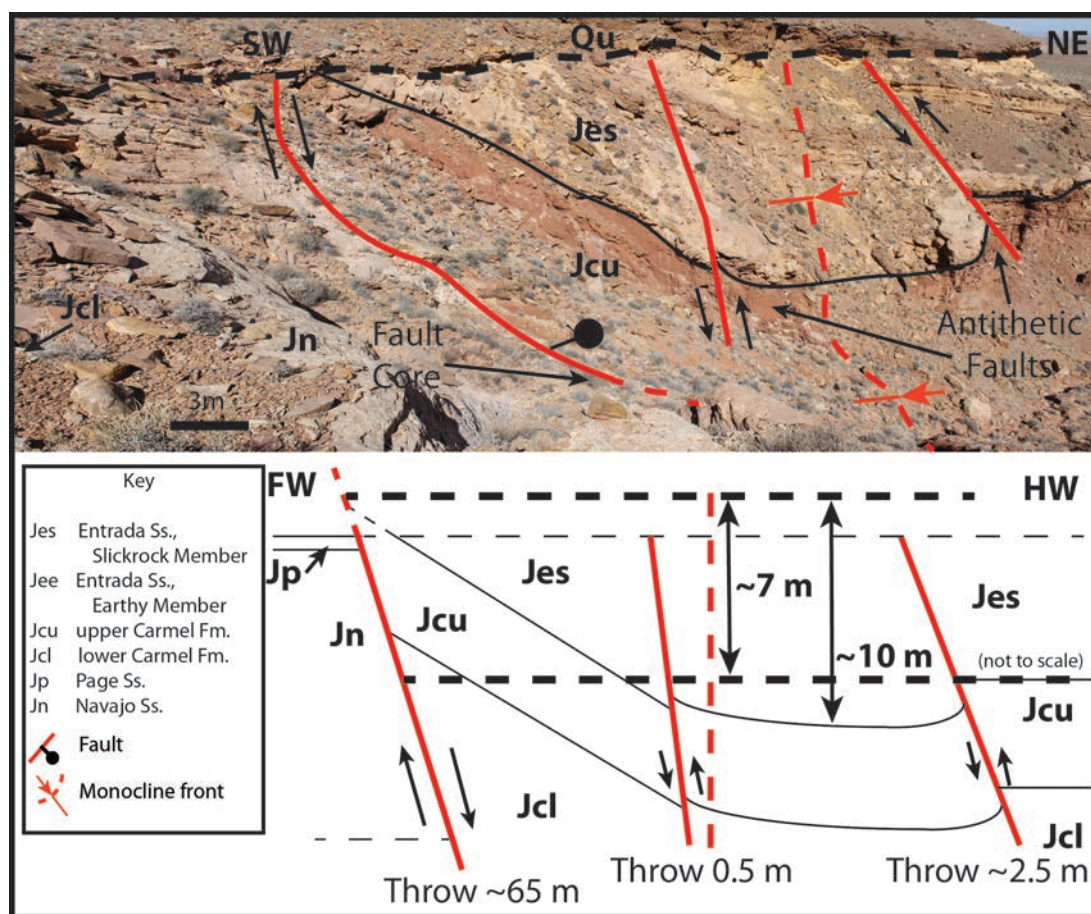


Figure 26. Annotated field photo and schematic cross-section of fault-related fold illustrating displacement accommodated by the flexure of bedding (Area D). View to the northwest of the fault core and primary slip surface in the eastern part of the fault zone (see Figure 14 for location).

cutting relationships are observed such that folds are cut by the fault obliquely, indicating that some of the folds existed at the time of continued fault growth. These folds are interpreted to be a result of the formation and propagation of the fault (Schlische, 1995; Janecke et al., 1998), and appear to be present mostly in the Earth Member of the Entrada Formation and in the upper and lower Carmel Formations and completely intact (entire fold structure preserved) near fault tips where throw approaches zero (Figure 27). They

are observed to be zones of increased fracture development and commonly coincidental with small faults that also appear to be related to the folding.

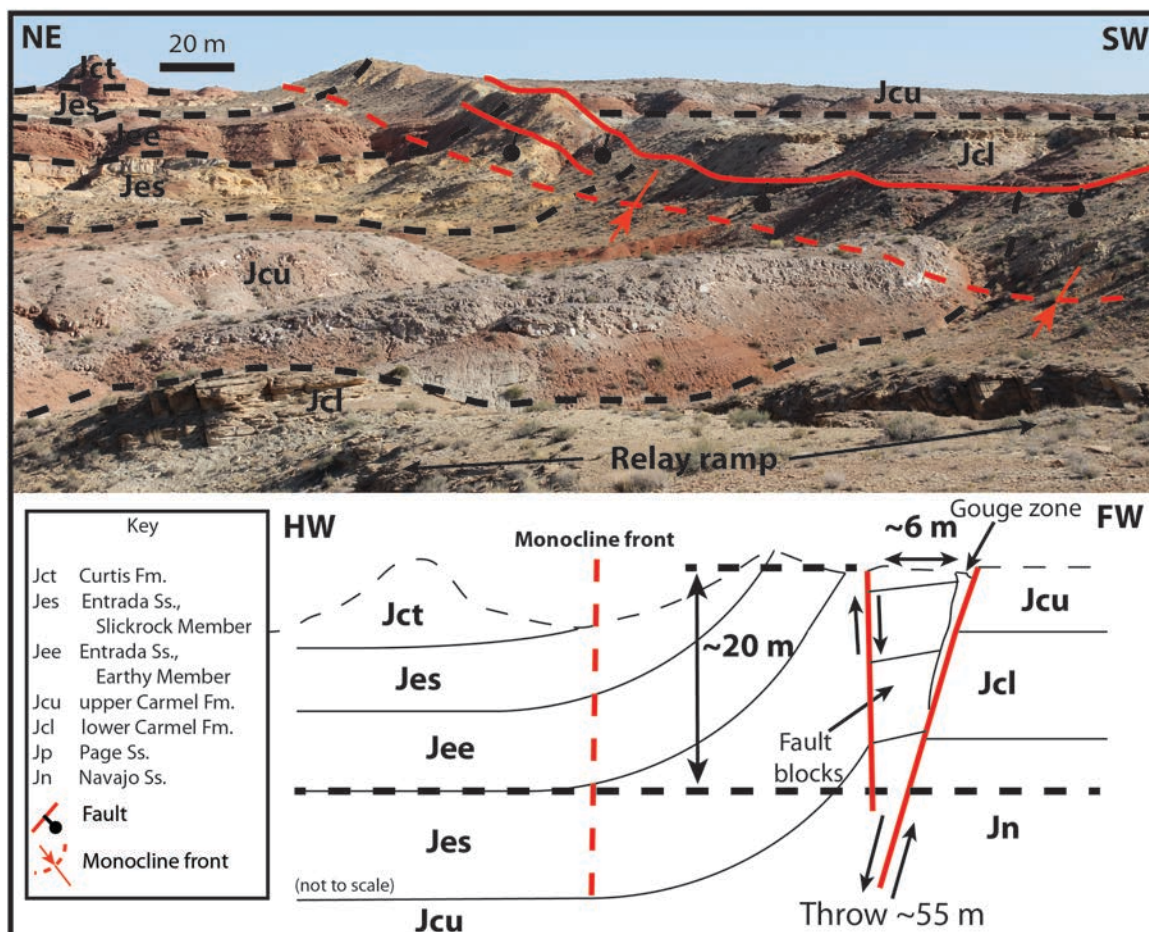


Figure 27. Annotated field photo and schematic cross-section of fault-related fold illustrating displacement accommodated by the flexure of bedding (Area B). View to the southeast of the fault core and primary slip surface in the central part of the fault zone (see Figure 12 for location).

Fault Zone Architecture

The majority of throw on the Iron Wash fault is commonly localized in a narrow fault core and surrounding damage zone (Figures 10 and 21). The fault is a complex zone

hosting principal slip surfaces with smaller associated structures surrounding the central fault core (Figure 9). Fracture intensity is highest within and adjacent to a narrow fault core and decreasing away from the fault core within both an inner and outer fault damage zone (Figure 9 and 23).

The core of the Iron Wash fault is highly heterogeneous along strike and is divided into distinct fault facies (Braathen et al., 2009). In some locations, the fault core is composed of rotated fault blocks suspended in a complex zone of fault gouge (Figure 21a). The fault blocks are commonly bound by the primary slip surface towards the hanging wall and synthetic faults (Figure 27). In areas of the fault where porous sandstones are in both the hanging wall and footwall, the fault core is composed of zones of intense deformation band development (Figure 28). In these zones, the fault core is a narrow (<50 cm) zone of coalesced deformation bands with little to no development of fault gouge or incorporation of fine-grained clay gouge into the fault zone (Figure 28). In other areas of the fault zone where fine-grained units are cut by the fault, the core is composed of narrow zones (<1 m) of highly developed fault gouge and clay smear surrounded by fault breccia, cataclasite, and occasionally rotated fault blocks (Figure 21b). Fault gouge and clay smear membranes are composed of cataclasite and altered clays derived from the faulted rocks of both the hanging wall and footwall. Fault breccia recemented with calcite and fine-grained quartz sand matrix is exposed in areas of the fault where porous sandstones are juxtaposed (Figure 28). The fault breccias are composed of angular to sub-angular clasts of sandstone in a cataclastic matrix that is recemented with calcite and to a lesser extent quartz (Figure 28).



Figure 28. Annotated field photos of expressions of the fault core and damage zone. a) View to the northwest of fault core consisting of fault breccia and deformation bands in the Navajo Sandstone, b) fault core showing intensely deformed fault breccia recemented with calcite in the Navajo Sandstone close to contact with lower Carmel Formation, c) coalesced deformation bands along the footwall side of the fault core in the Slickrock Member of the Entrada Formation, and d) coalesced deformation bands along the fault core in the Navajo Sandstone.

The Iron Wash fault zone has a heterogeneous architecture along strike and contains distinct architectural components such as rotated fault blocks (Figure 21a), fault

lenses (Figure 29a), brecciated fault core containing fault blocks (Figure 29b), and commonly consists of multiple slip surfaces (Figures 21a and 29). Along-strike variations in the fault zone architecture and the linkage of slip surfaces are characterized by four representative cross-sections of the fault zone (Figure 30). We see large variability in fault block and fault core width, distance between slip surfaces, distribution of slip on slip surfaces, and amount of rotation of fault blocks (Figure 30). In some locations, the footwall has been dragged down into the damage zone of the fault (Figure 31). Dragging of the footwall down into the fault zone creates the inner damage zone of the fault where zones of intense fracturing are present (Figure 31). In other areas of the fault, the fault core is composed of a combination of fault-related folds and large (8 m long and 4 m wide) rotated fault blocks (Figures 21a, 26, 27, 30, and 31). The fault blocks and fault related folds are typically spatially associated with multiple synthetic and antithetic faults (Figure 26, 27, 30, and 31).

Evidence for Fluid Migration

The interaction between faulting and fluids has been described by many previous workers in many different field localities (e.g. Barton et al., 1995; Hickman et al., 1995; Foxford et al., 1996; Evans et al., 1997; Peaver et al., 1997; Chan et al., 2000; Gudmundsson et al., 2001). Evidence for fluid migration along faults in and around the San Rafael Swell area has also been well documented (e.g. Evans et al., 2004; Shipton et al., 2004). We present here evidence for fluid migration along the Iron Wash fault within the fault core, in the damage zone and away from the fault.

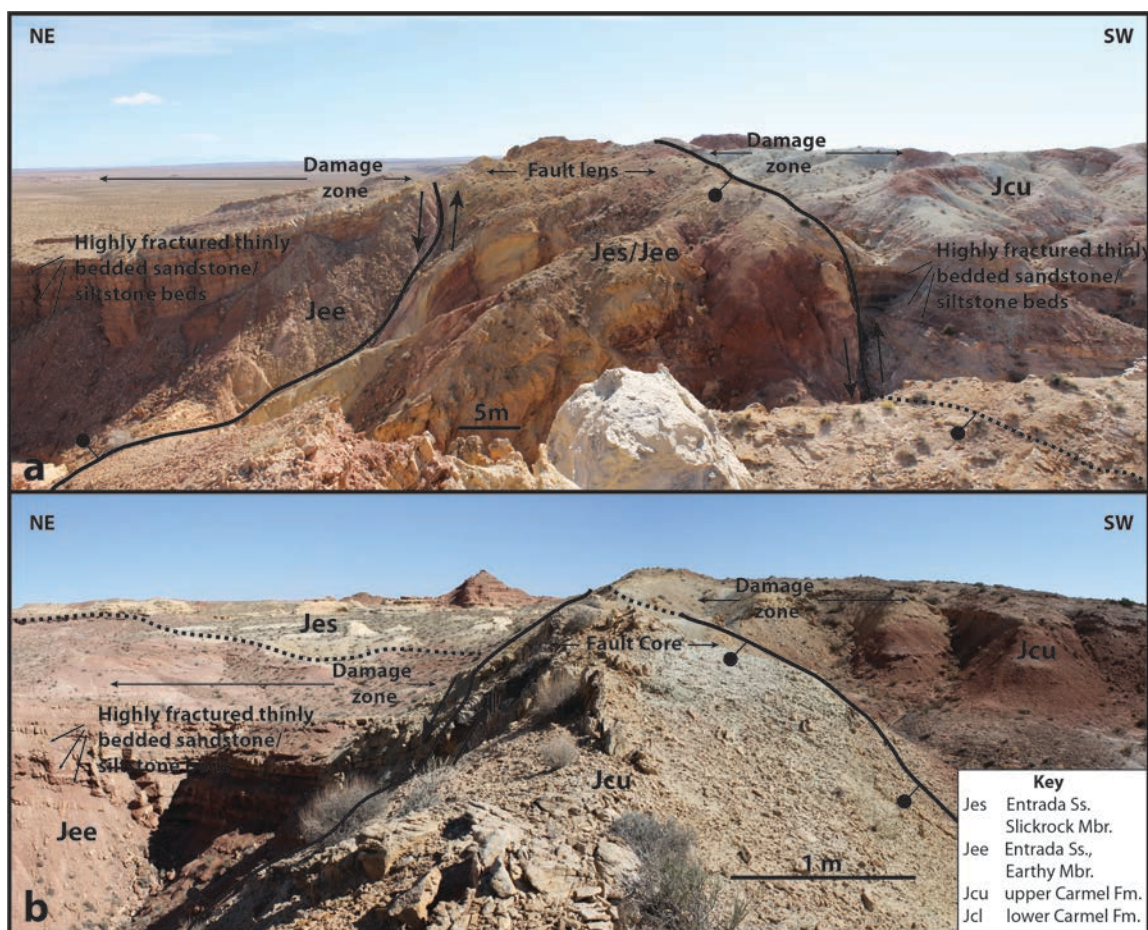


Figure 29. Annotated field photos of expressions of the architecture of the fault zone. a) View to the southeast of fault lens bound by two primary slip surfaces of the Iron Wash fault (Area C, see Figure 13 for location) and b) view to the southeast of ~3 m wide fault core containing fault breccia, rotated fault blocks and multiple slip surfaces (Area B, see Figure 12 for location).

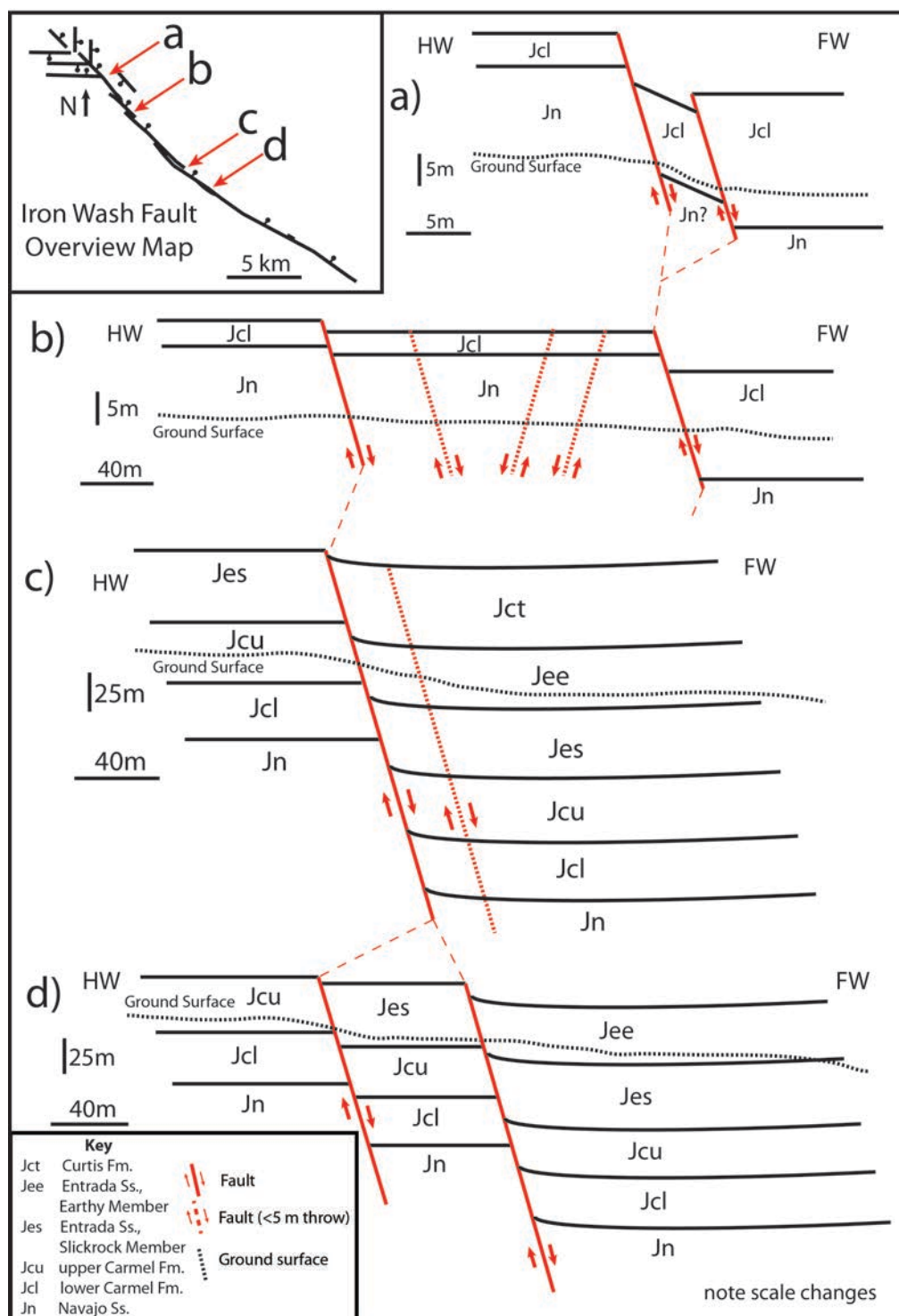


Figure 30. Multiple schematic cross-sections designed to illustrate fault architecture along strike. Cross-sections illustrate variation in geometry, width and multiple strands of faults that are part of the Iron Wash fault zone. These four examples are about 2-6 km apart and are based on field exposures of the fault zone and mapping of fault strands along strike.

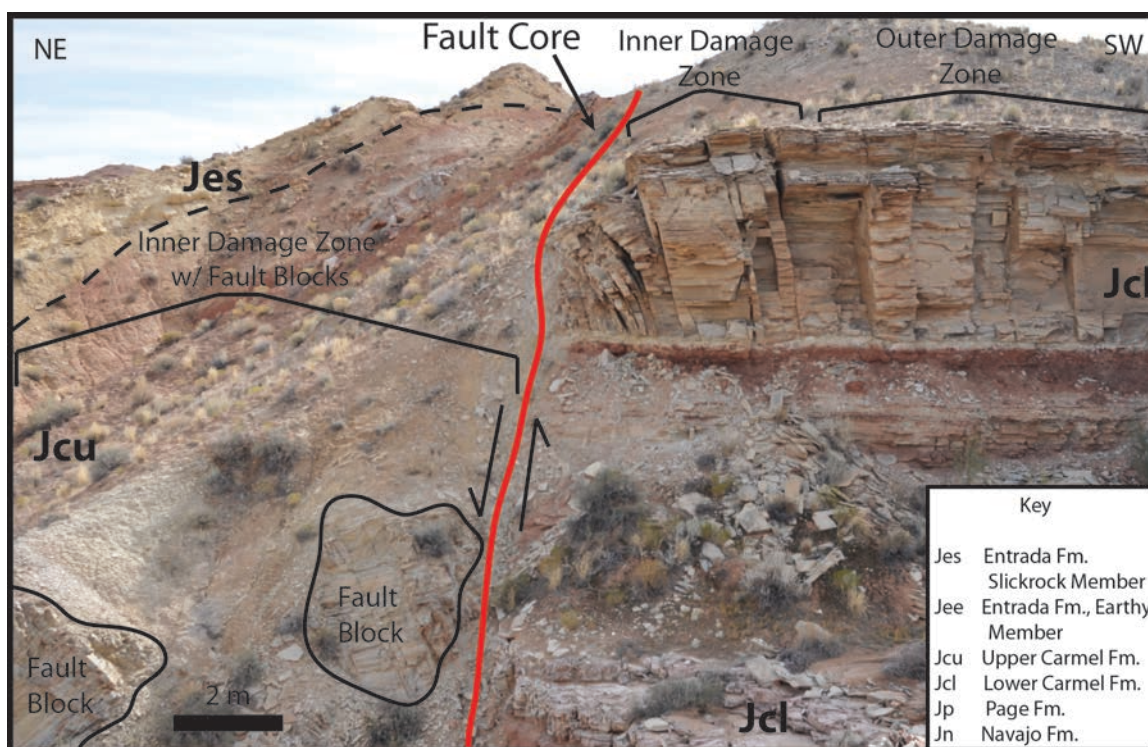


Figure 31. Annotated field photo of large fault blocks within the fault core adjacent to fault related monocline. View to the southeast of the central part of the fault zone showing a relatively undeformed damage zone in the footwall and highly fractured damage zone in the hanging wall (see Figure 12 for location).

Evidence for the migration of fluids along the Iron Wash fault includes structures and features resulting from fluid-rock interactions and preserved mineralization within faults and fractures (e.g. Barton et al., 1995; Foxford et al., 1996; Evans et al., 1997). Evidence for fluid alteration and mineralization is observed along most of the length of the fault zone at different intensities and types of alteration products (Chan et al, 2000). These features reflect the type of fluids present, the chemistry and reactivity of the fluid and the rock involved, and the pressure-temperature regime at which the fluid-rock reactions occurred (e.g. Peaver et al., 1997; Chan et al., 2000; Gudmundsson et al., 2001).

Bleached rocks along and adjacent to fractures are common where reducing fluids have moved along fractures and removed or 'bleached out' the iron oxide (or other oxide) staining from a volume of rock surrounding the fracture (Figure 32; Hawley, 1968; Foxford et al., 1996; Chan et al., 2000). Bleaching and oil staining are commonly both present within the same fracture systems (Figure 32), lending credence to the idea that bleaching here is related to oil migration in and along the fault zone. Bleached and unbleached fractures have a dominate orientation of $\sim 310^\circ$ which is similar to strike of the fault with a minor component of fractures striking more east-west (Figure 33a). Unbleached fractures also have a north-south striking fracture set and a east-west striking fracture set (Figure 33b).

Oil staining is found within fractures in numerous locations along the fault. This 'dead' oil has lost all or most of the aromatic compounds and is present as a stain (Figure 34) or as crystallized oil preserved in fractures (Figure 32). Oil is also found staining rocks within the fault core in various locations and is commonly cut by later episodes of faulting (Figure 34) or concentrated along fractures and cross-bedding (Figure 34). Oil-stained fractures have a dominate strike of $\sim 310^\circ$ or generally parallel to strike of the fault, with a minor east-west striking component (Figure 33c). Based on cross-cutting relationships in the oil-stained rocks, it is clear that the majority of oil staining is older than the deformation associated with the formation of the Iron Wash fault. Evidence of this cross-cutting relationship is clear in areas where oil-stained sandstone with cross-bedding of the Slickrock Member of the Entrada Formation is cut by later faulting and fracturing (Figure 34a, b). However, in several instances it is clear that oil migration occurred after deformation bands within the porous sandstone units had formed (Figure

34c). In others locations, oil appears to have been present at the time of formation of deformation bands because oil residue is incorporated into the cores of the deformation bands (Figure 34c)

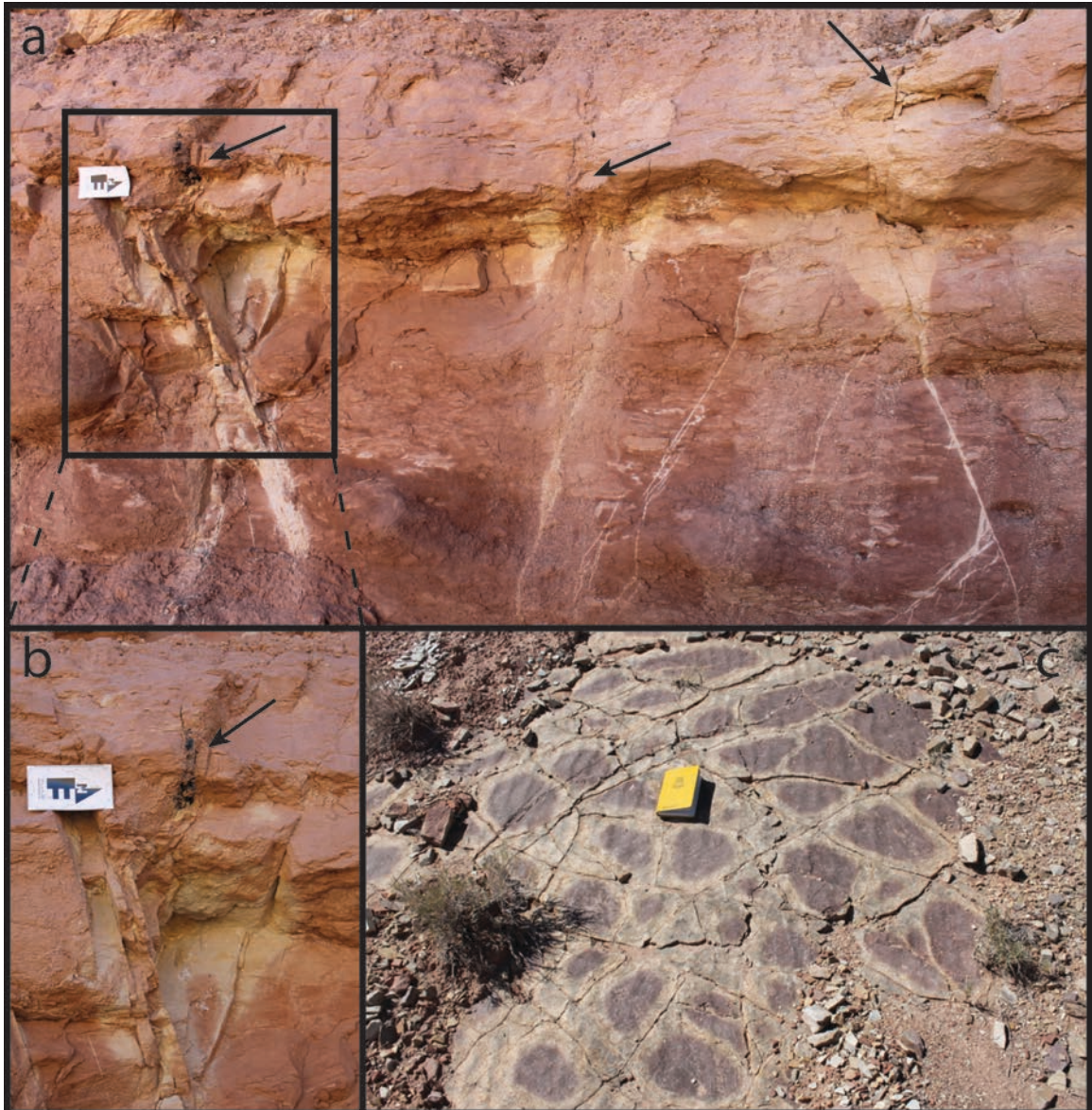


Figure 32. Annotated field photos of evidence for fluid migration within the fault zone. a) Bleached fractures and oil staining (indicated by arrows) within fractures located in the damage zone of the fault in the Earthy Member of the Entrada Formation, b) close-up view of box in Figure a, and c) bleaching halos around fractures in the lower Carmel Formation in a rippled bedding plane surface of a silty oolitic limestone.

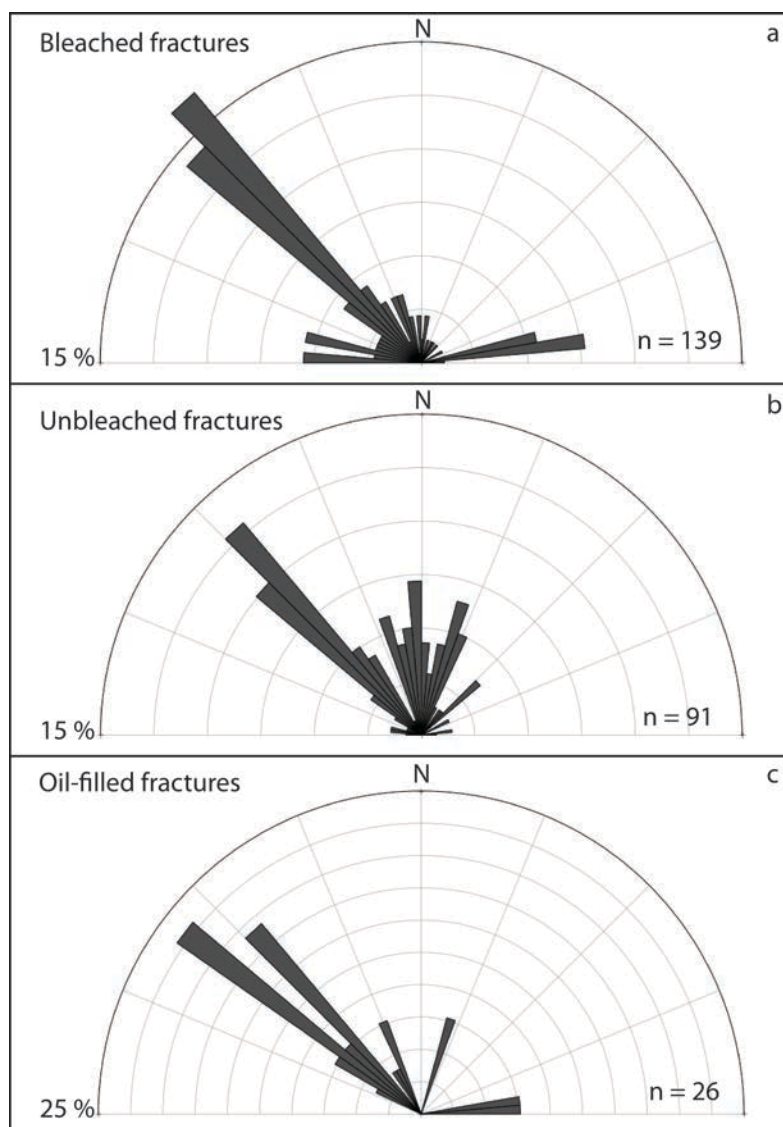


Figure 33. Rose diagrams showing strike of fractures with different morphologies along the Iron Wash fault. Fracture data collected from Area B and projected in the northern hemisphere with 5° bins. a) Bleached fractures, b) unbleached fractures, c) oil-filled fractures. Note scale change in c.

Breccias in the fault zone commonly contain angular to sub-angular clasts of sandstone encased in a calcite-cemented sandstone, siltstone and cataclasite matrix (Figure 28). Clasts suspended in the breccia commonly show evidence for multiple generations of deformation as they are composed of sandstone that contains deformation

bands and is then incorporated into the fault core (Caine et al, 2010). These breccias are interpreted to be the result of formation of the brecciated fault rock and cementation by calcite- or CO₂-bearing fluids producing a matrix of fine-grained calcite and cemented cataclasite (Caine et al., 2010).

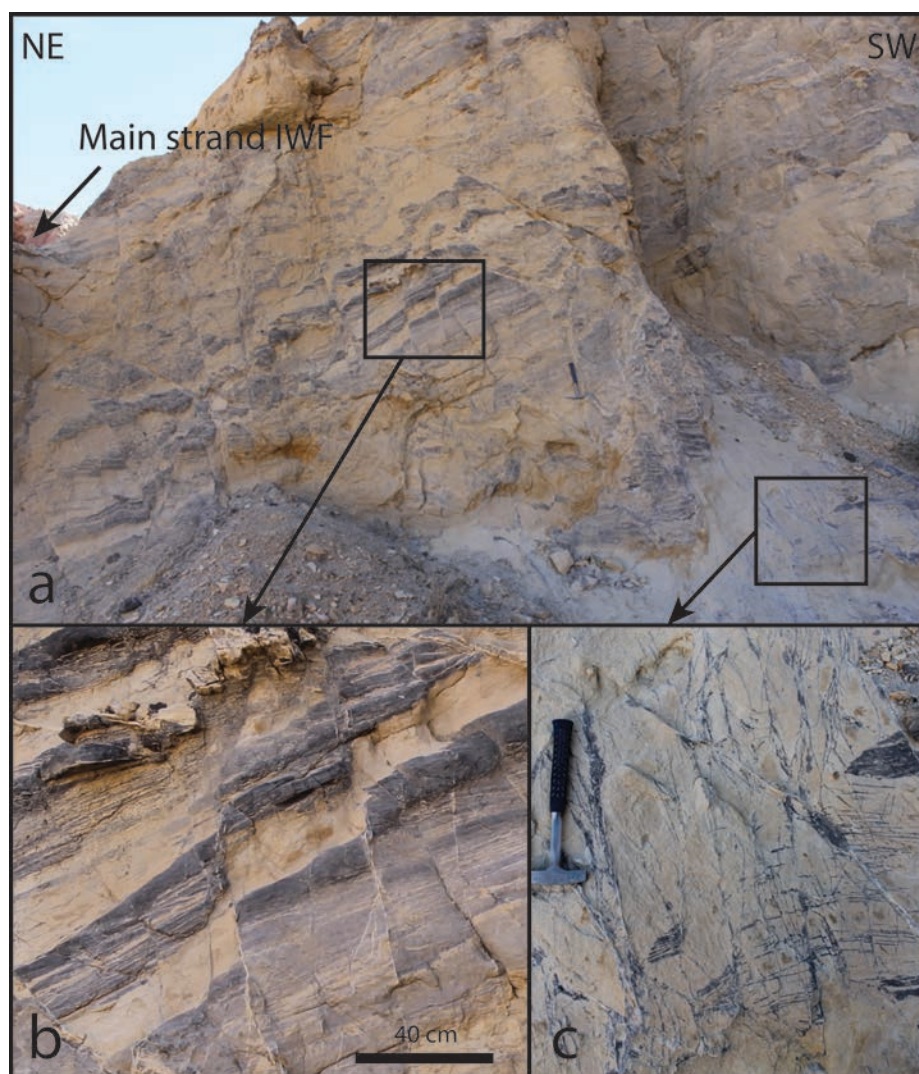


Figure 34. Annotated field photos of examples of evidence for fluid migration within the fault zone in Area C within a fault lens. a) View to the southeast of the fault lens with extensive oil staining within bedding cut by later faulting in the Slickrock Member of the Entrada Formation (see Figure 13 for location), b) close-up view of box in a, showing oil-stained bedding cut by later faulting, and c) close-up view of box in a, showing deformation bands and oil staining concentrated in fractures.

X-Ray Diffraction Analysis of Fault-Related Rocks

X-Ray diffraction analysis was conducted on 15 samples to examine the mineralogy of the host rock and fault rocks. Host rock samples included porous sandstones of the Navajo Sandstone and the Slickrock and Earthy Members of the Entrada Formation to characterize any evidence of alteration of these formations (Figure 35). All samples collected from host rock are composed almost exclusively of quartz (Figure 35). Analysis of one oil-stained sample of the Slickrock Member of the Entrada Formation indicated the presence of carbon (Figure 35). Unbleached samples of the Slickrock Member of the Entrada Formation contained hematite while bleach samples were devoid of hematite and contained dolomite and kaolinite (Figure 35). One sample of the Navajo Formation and a bleached sample from the Slickrock Member of the Entrada Formation contained calcite as secondary minerals.

A sample transect with 4 samples within the fault core in a location with Navajo Formation in the footwall and upper Carmel Formation in the hangingwall was analyzed for mineralogy to determine any variation across the fault core (Figure 36). Samples were collected approximately every 12 cm across the fault core (Figure 36). The dominant fault zone mineralogy is quartz and calcite (Figure 36). In the two samples closer to the footwall, dolomite is present (Figure 36). Clay content increases closer to the footwall as indicated by the presence of illite, muscovite and mica and a more intense clay peak in the diffractograms (Figure 36). We interpret increasing clay content as indicative of a more well-developed fault core resulting from incorporation of material derived from the hanging wall and footwall and altered by migration of fluids through the fault zone.

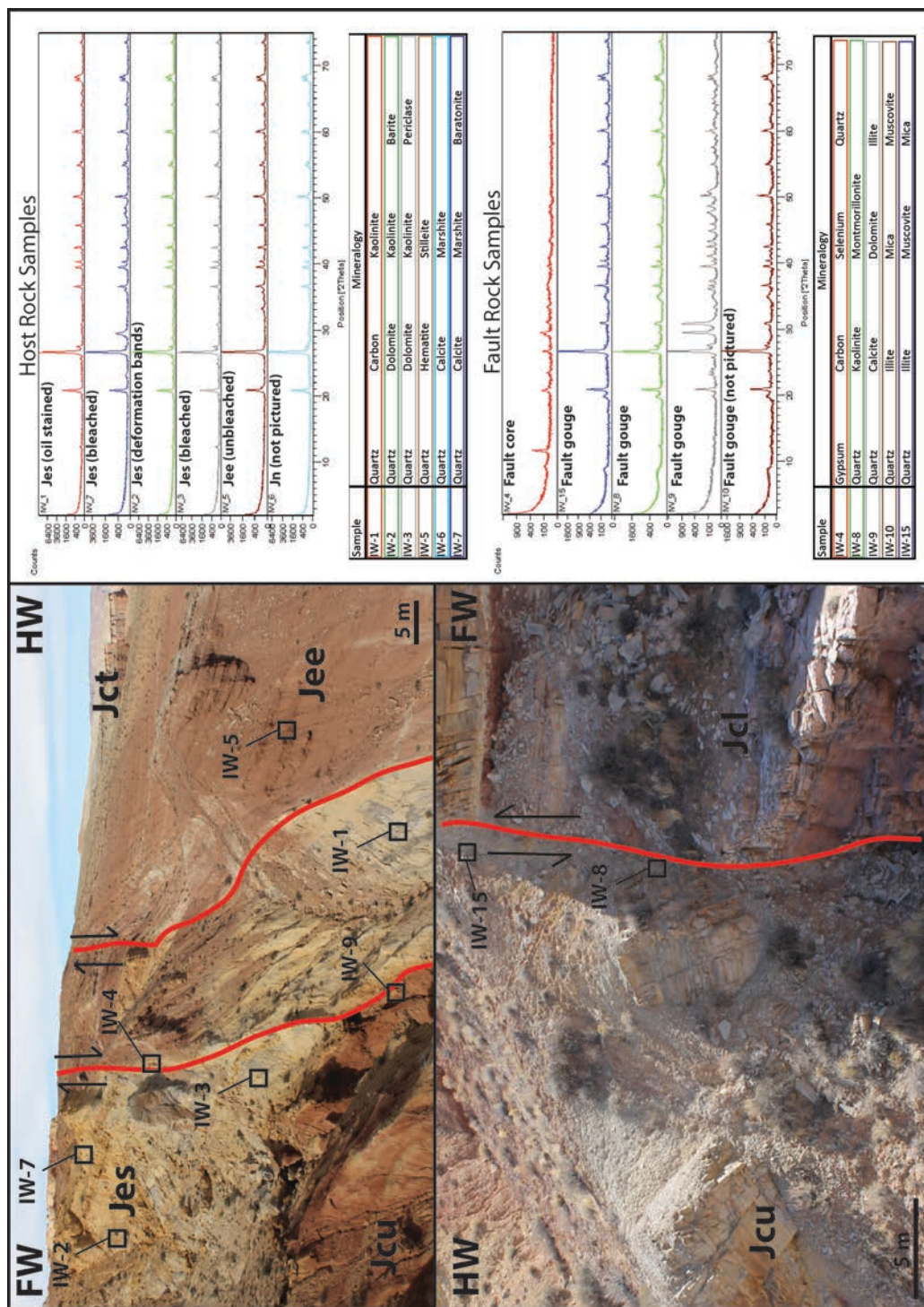


Figure 35. X-Ray diffraction analysis for host rocks and fault-related rocks. Annotated field photos showing sample locations from Areas B and C, diffractograms showing intensity in counts for 2θ angles of diffraction, and interpreted mineralogy for each sample (some samples not pictured).

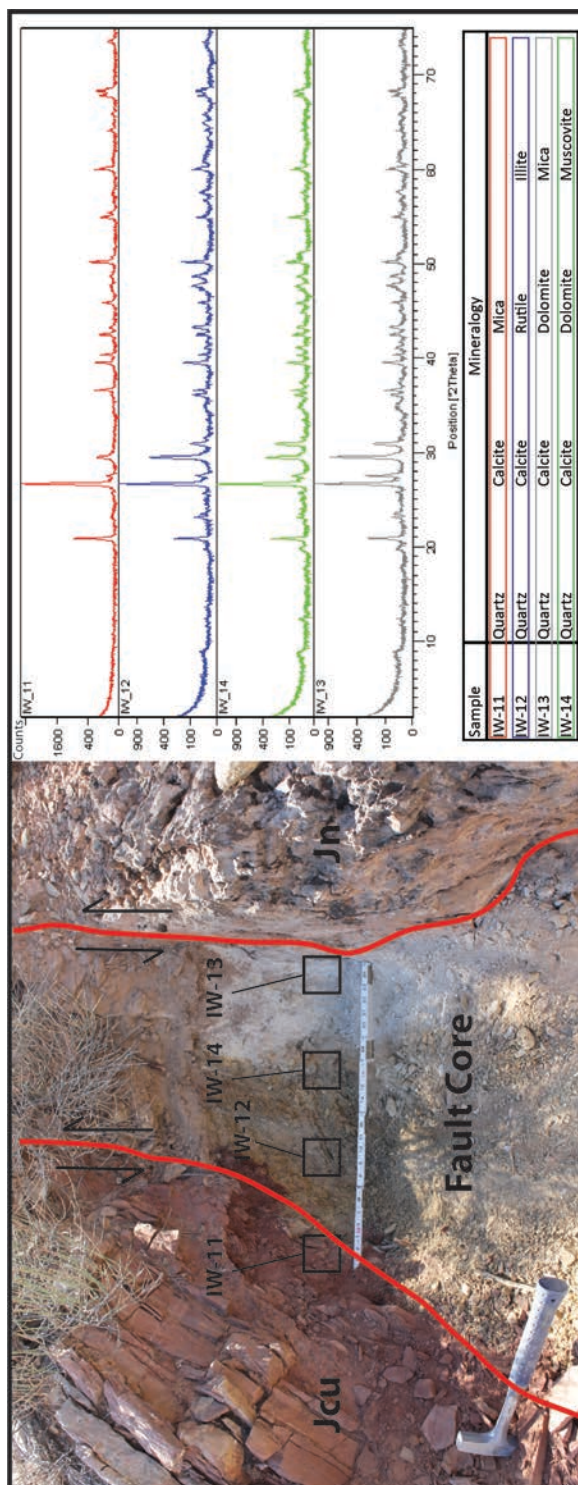


Figure 36. X-Ray diffraction analysis for a sample transect across a fault gouge zone. Annotated field photos showing sample transect in Area B, diffractograms showing intensity in counts for 2θ angles of diffraction, and interpreted mineralogy for each sample.

Petrographic Analysis of Fault Rocks

Petrographic analysis of 24 thin sections add insight into relative timing and types deformation mechanisms, evidence for fluid migration, and mineralization in and around the fault zone. Photomicrographs demonstrate many micro-textures and structures including intra-, inter- and transgranular microfractures and fault-related rocks such as cataclasite breccias. The host rocks are composed of fine to medium-grained well-sorted sandstones, with thinner siltstones, oolitic and fossiliferous grainstones, lime mudstones and gypsum beds.

Cataclastic deformation bands are the most common microstructure identified in the fine to medium-grained porous sandstones and exhibit grain crushing of different intensities (Figure 37a; Antonellini and Aydin, 1994; Fossen et al., 2007; Rotevatn et al., 2008). Within cataclastic band cores, well- to sub-rounded quartz grains are interpreted to have experienced grain crushing resulting in reduction in grain sizes (Figure 37a). We observe intense grain-size reduction from initial quartz grains with grain diameters of ~0.2-0.6 mm down to <0.05 mm and suspension of these grains in a matrix of ultra-fine-grained cataclastic material (clay size) and calcite cement (Figure 37 a and b). Cataclastic deformation bands are in places cut by later generations of fractures that are typically filled with calcite (Figure 37 a and b).

Two of the dominate deformation mechanisms observed within the field area are cataclastic deformation bands (Figure 37a) and breccias of the fault core (Figure 37b). Deformation bands are the dominate deformation structure in the porous sandstones of the Navajo Formation and the Slickrock Member of the Entrada Formation. They are interpreted to be the result of mechanical reduction in grain size as individual quartz

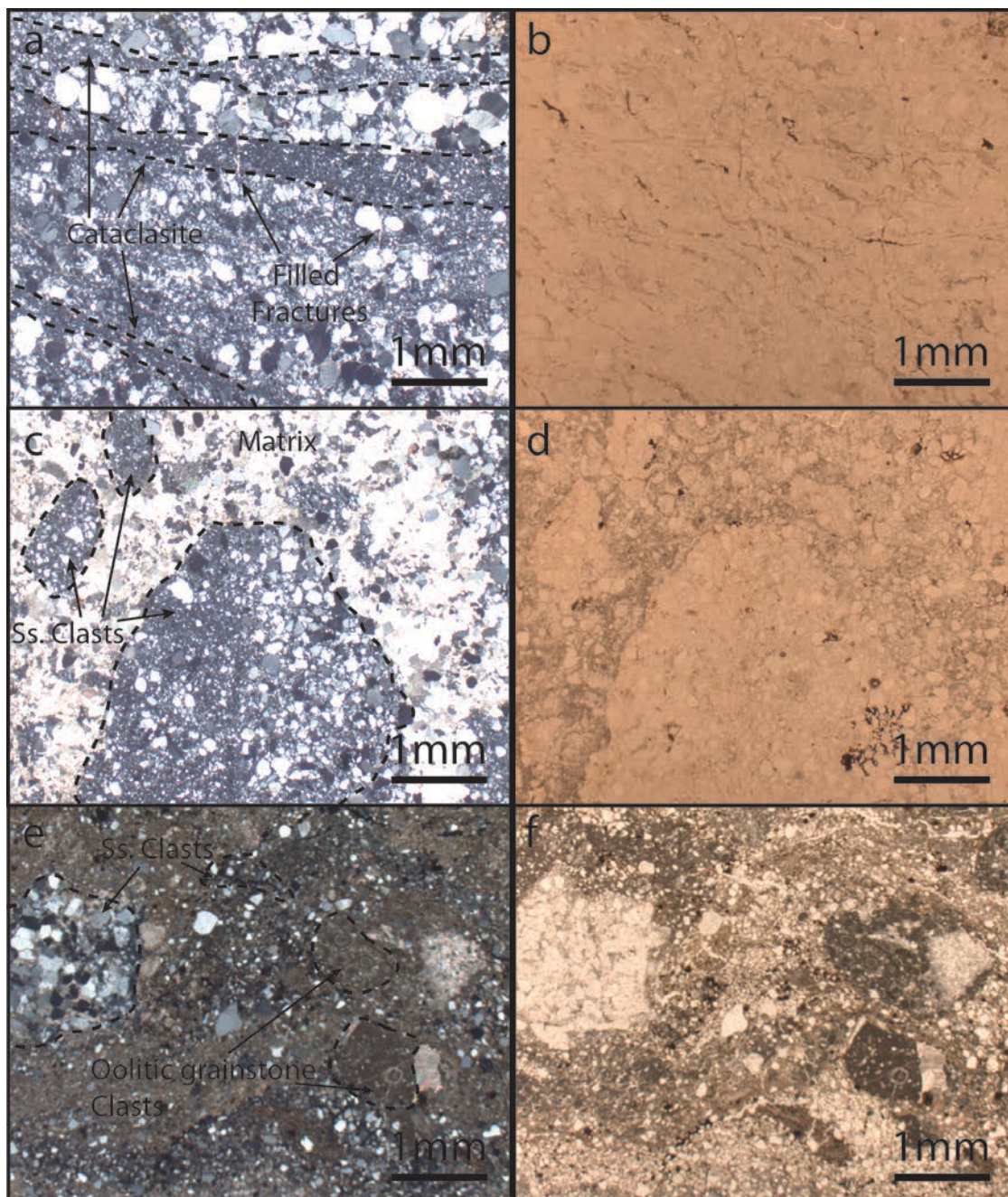


Figure 37. Photomicrographs of deformation structures in the Iron Wash fault zone. Left images are cross-polarized light, right images are plane-polarized light. a/b) Porous sandstone of the Navajo Formation showing cataclastic deformation bands and cross-cutting filled fractures, c/d) fault breccia composed of material from the lower Carmel Formation and Navajo Sandstone within fault core containing quartz sandstone clasts supported in a calcite-cemented matrix and, e/f) fault breccia from within fault core with arrows showing different components of the fault core including clasts of sandstone, oolitic grainstone, lime mudstone, and calcite-cemented cataclastic material from the lower Carmel Formation and Navajo Sandstone.

grains are crushed and porosity is reduced during slip along the deformation band (Antonellini and Aydin, 1994; Fossen et al., 2007; Rotevatn et al., 2008). Cataclastic deformation occurs away from the fault as isolated or coalesced clusters of deformation bands. Highly developed zones of coalesced deformation bands are commonly the primary deformation structure of the fault core and accommodate the majority of slip on the fault (Figure 28).

Fault breccias and evidence for later cementation to preserve the breccia textures are seen in many locations along the fault (Figure 31). Fault breccias typically consist of sub-angular to sub-rounded clasts of porous sandstone suspended in a matrix of individual grains and cataclastic material and in many cases are cemented with calcite (Figure 37 c and d). Many of the clasts of the fault breccias consist of previously cataclastically deformed rock, which is evident by cataclastic deformation bands within clasts creating a cataclasite in breccia texture (Figure 37 c and d). Several examples of the incorporation of components of the hangingwall and footwall into the fault breccias are seen on both hand sample and in thin section. In places, fault breccias are composed of clasts of sandstone derived from the footwall and clasts of oolitic limestone derived from the hanging wall (Figure 37 e and f). Many of the fault breccias are cemented with ultra-fine-grained calcite containing cataclastic material and individual suspended grains (Figures 37 c, d, e, and f). Fault breccias result from the mechanical crushing of fault rocks to produce angular to sub-rounded clasts of rock that become suspended in a matrix of fine-grained sand and silt that is cemented by calcite to preserve the breccia texture (Figure 37).

Oil staining within the fault zone is common and is most intense within the fault lens in the central segment of the fault zone (Figures 35 and 36). It is characterized in hand sample by black staining and occasional fetid odor of hydrocarbon present when fresh surfaces are exposed. In thin section, oil staining appears as amorphous opaque fill within pore space, in deformation bands, filling or partially filling fractures and as staining rims on calcite crystals (Figures 38 and 39). We differentiated oil from hematite staining, which is the other common opaque material in thin section, by the use of reflected light where oil appears black and lacks the red or rust colored rims that hematite commonly exhibits (Figure 38).

Hydrocarbon occupies most or all pore space within some samples (Figure 38b). Hematite-coated grains are commonly present in many of the samples containing oil staining (Figure 38e) and in some cases, oil and calcite seem to displace hematite and concentrate it in discrete bands within the rock (Figure 38b). Commonly in breccias and more deformed samples, oil and hematite are both present filling pore space or coating grains within the calcite matrix or in suspended clasts (Figure 38h).

Evidence for several fluid types are seen within the same fracture or fracture sets filling different areas of the fracture and/or contained within previously mineralized fractures. Most commonly, calcite mineralization and oil staining are seen co-located within the same fracture and occasionally with hematite also present (Figure 39). Oil staining is commonly contained within calcite crystals that have mineralized open fractures. In such cases, oil staining is not in contact with the fracture wall (Figure 39 a and b). In other cases, oil fill almost fills the entire fracture with little to no formation of calcite crystals (Figure 39 c and d). In places, oil staining lines the calcite crystal grain

boundaries (Figure 40). Microfractures are also seen to contain oil staining and calcite cement in fracture widths $<10\ \mu\text{m}$ (Figure 39 c and d).

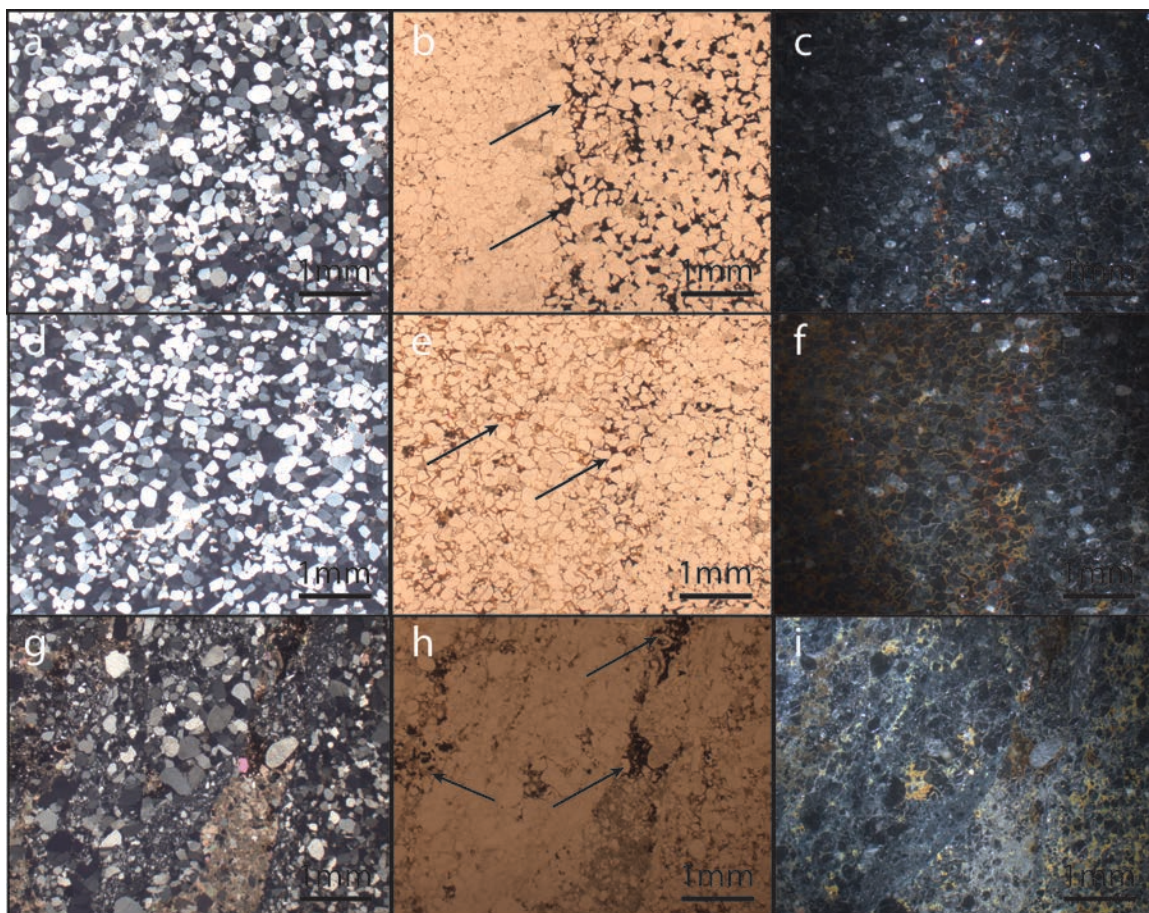


Figure 38. Photomicrographs of mineralization in the Iron Wash fault zone. Left images are cross-polarized light, middle images are plane-polarized light, right images are reflected light. a/b/c) Well-sorted sandstone of the Slickrock Member of the Entrada Formation, arrow shows oil staining and minor hematite staining is present, d/e/f) well-sorted sandstone of the Slickrock Member of the Entrada Formation showing hematite-coated grains throughout the sample and minor oil staining and, g/h/i) fault breccia composed of Slickrock and Earthy Members of the Entrada Formation showing calcite cemented matrix with oil staining and hematite and calcite cement.

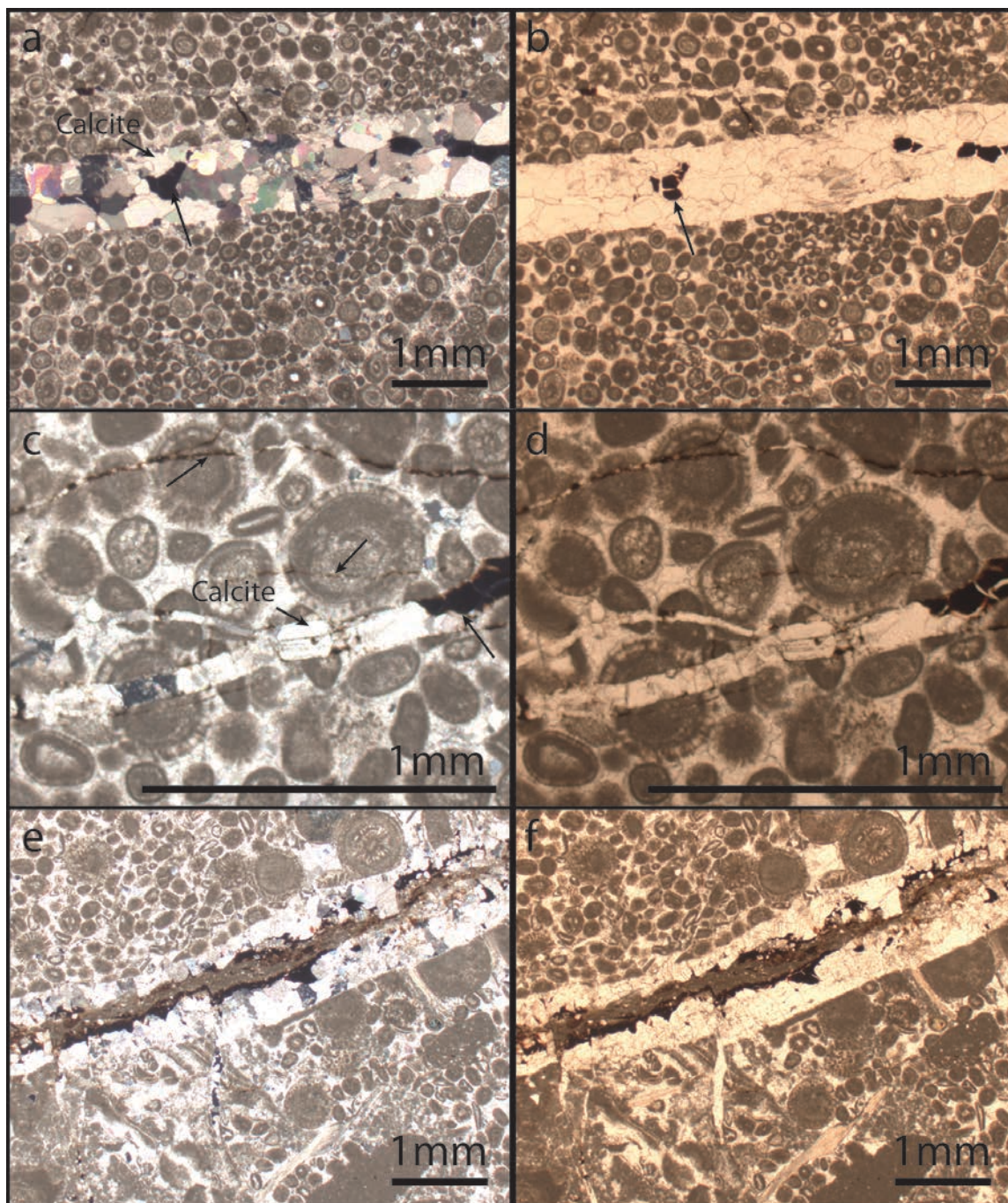


Figure 39. Photomicrographs of fracture mineralization in the Iron Wash fault zone. Left images are cross-polarized light, right images are plane-polarized light, samples are oolitic grainstones of the lower Carmel Formation. a/b) Calcite mineralized fractures with arrows indicating oil staining confined within the calcite crystal matrix, c/d) calcite mineralized fractures containing oil staining arrows indicating micro-fractures containing mostly oil staining and minor calcite mineralization, and e/f) calcite mineralized fracture with calcite crystals on the fracture margins, oil staining contained within the calcite, and a fine-grained oil-stained calcite cemented cataclasite in the interior of the fracture.

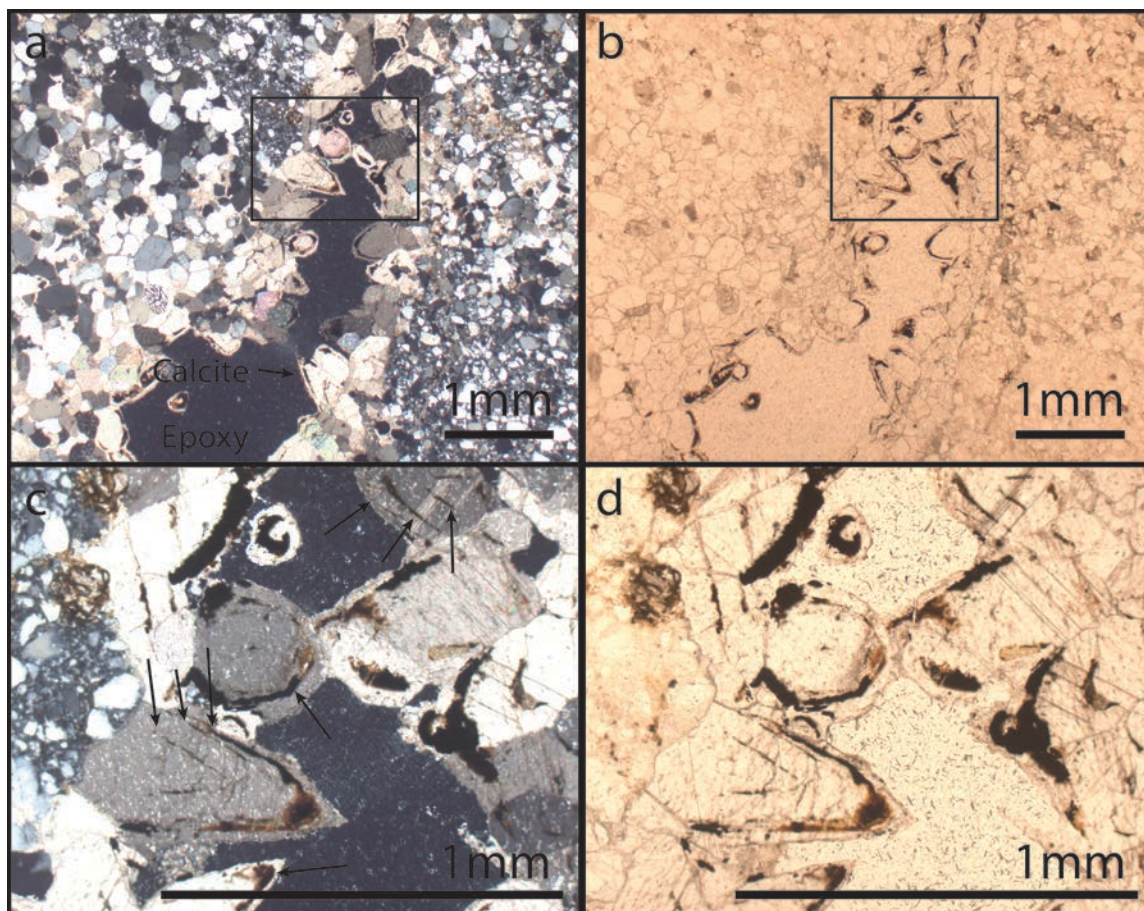


Figure 40. Photomicrographs of calcite growth and mineralization in fractures in the Iron Wash fault zone. Left images are cross-polarized light, right images are plane-polarized light, sample from the fault core with open mineralized fractures in Navajo Formation. a/b) Open fracture lined with euhehedral calcite crystals, inset box shows locations of c and d, c/d) euhehedral calcite crystals showing locations of oil staining rings formed during crystal growth.

Evidence of multiple generations of fluid flow is found in several samples from the fault core. Calcite fracture fill is observed to have grown on the margins of an open fracture and encompasses an oil-filled inner fracture with a fracture core of oil-stained cataclastic material (Figure 39 e and f). The inner fracture fill is a calcite-cemented, oil-stained matrix supported cataclasite containing survivor grains of calcite rock fragments (Figure 39 e and f). Euhehedral calcite crystals that have grown on the margins of an open

fracture demonstrate multiple phases of calcite crystal growth and oil staining as evidenced in Figure 40. Calcite crystals have oil bands that are interpreted to have been oil that stained the outer part of the crystal during early generations of crystal growth and was subsequently encased by additional calcite growth. By counting the number of oil-stained bands in the crystal, it appears that these crystals record at least three cycles of calcite growth and oil wetting. This interpretation is based on the number of bands and does not imply that multiple episodes of fluids moved through the fracture, only that there were stages of crystal growth and oil staining (possibly during the same fluid event).

Deformation bands that have formed in the presence of oil staining are black in hand sample and appear to be "oiled" deformation bands (Figure 36). In the oil-stained porous sandstones where deformation bands have formed, it seems that the cataclastic textures formed after the oil staining, based on the apparent incorporation of oil stained material into the cataclastic material. In thin section oil can be seen staining the undeformed sandstones and is incorporated into the core of the cataclastic bands (Figure 41 a and b). Within the deformation bands oil is seen as stained areas or zones of oil staining aligned with the deformation band (Figure 41 c and d). Oiled deformation bands are interpreted to be the result of dead-oil stained porous sandstone experiencing later formation of cataclastic textures.

The nature of fracture margins can provide some insight into how these fractures formed and timing of mineralization. Some fractures show complex boundaries where cataclasite and calcite-cemented grains create a very tortuous fracture boundary with a less distinct margin that is the edge of a fracture that is mineralized with large (~1-2 mm) calcite grains (Figure 42 a and b). Other fractures show distinct fracture margins with

very discrete boundaries that follow grain boundaries that in some cases and cut across grains in some cases, but overall create a sharp fracture boundary. Calcite mineralization is inside many fractures throughout the field area (Figure 42 c and d).

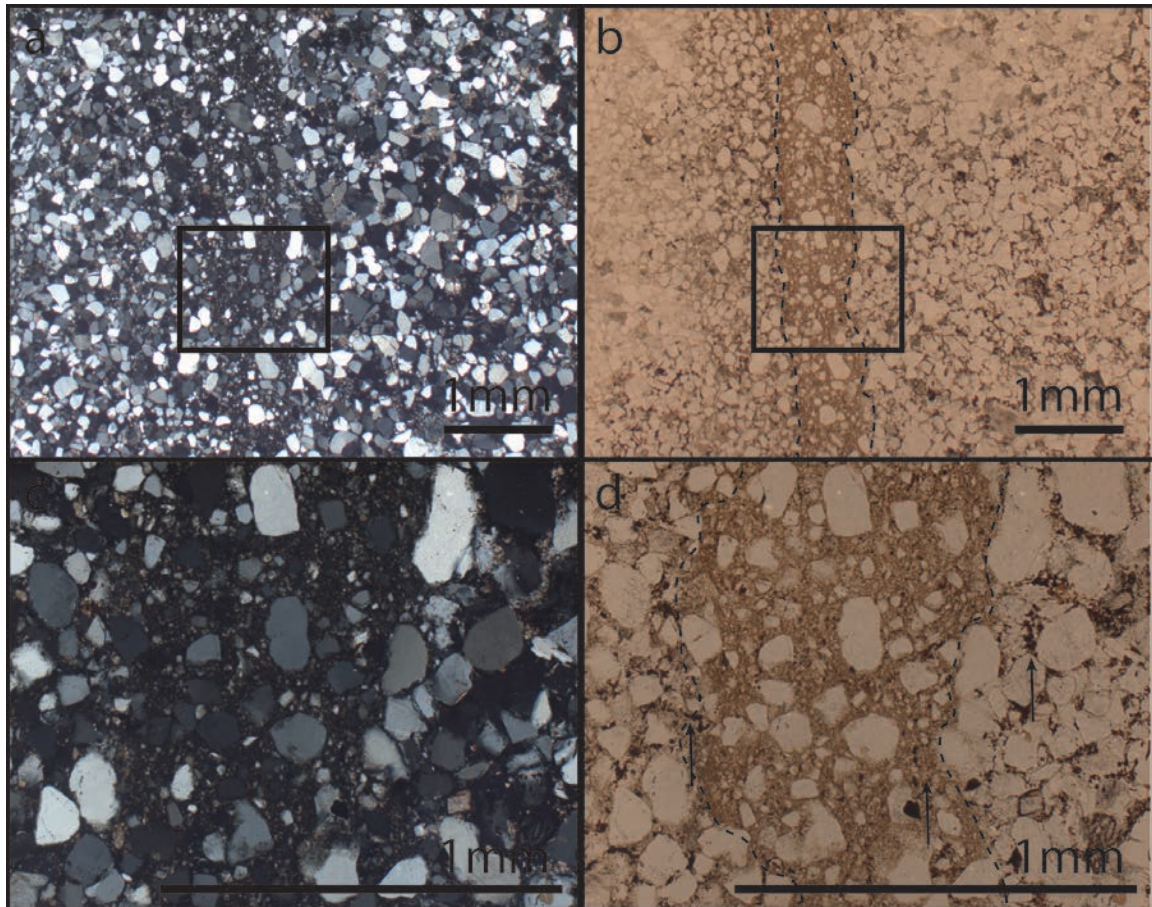


Figure 41. Photomicrographs of oil-stained and mineralized deformation bands in the Iron Wash fault zone. Left images are cross-polarized light, right image is plane-polarized light, samples are porous sandstones of the Slickrock Member of the Entrada Formation. a\b) Cataclastic deformation band within an oil-stained sample, the deformation band contains oil from the surrounding rock and calcite cementation, inset box shows locations of c and d, c\d) close-up of cataclastic material with oil staining surrounding the cataclastic core, the deformation band contains calcite and oil stain.

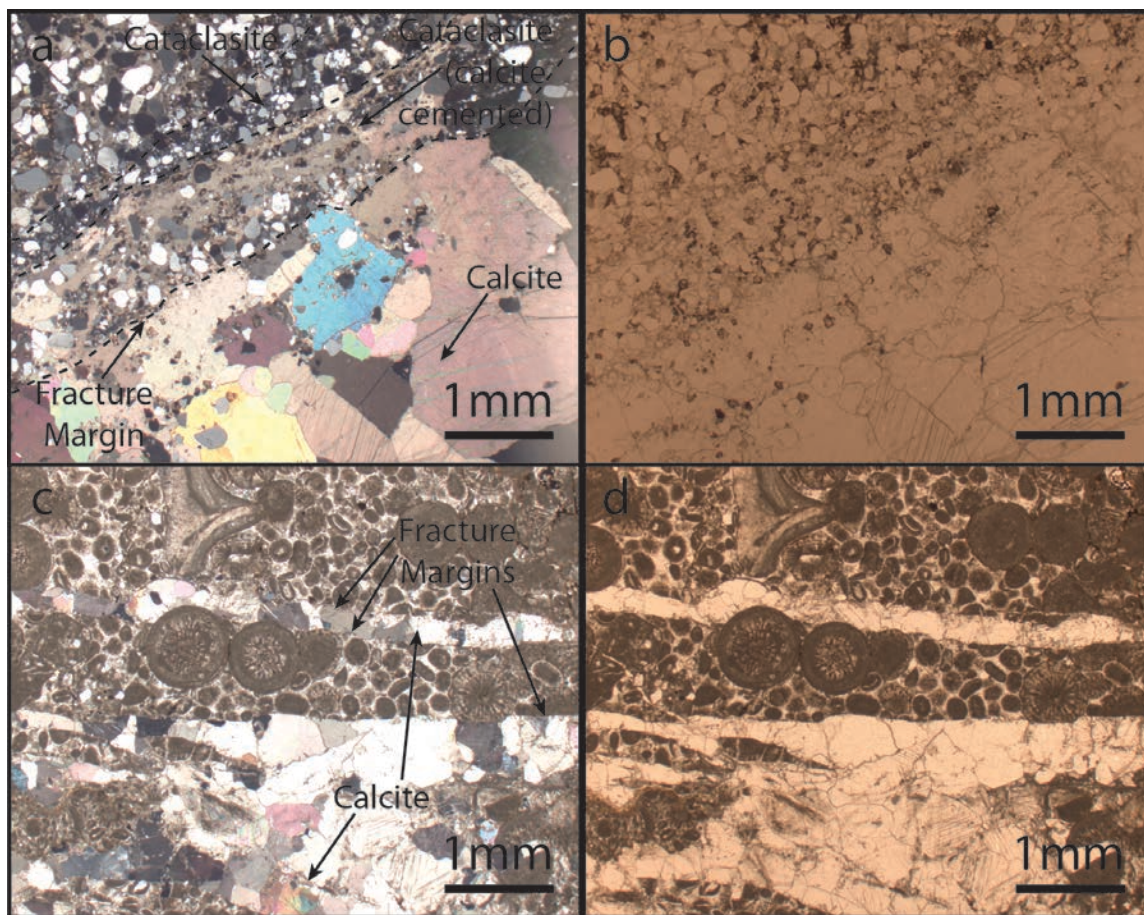


Figure 42. Photomicrographs of mineralized fractures and fracture margins in Iron Wash fault zone. Left images are cross-polarized light, right images are plane-polarized light. a/b) Fracture margin in Navajo Formation with cataclasite and calcite-cemented grains adjacent to large calcite crystals within the fracture, c/d) calcite mineralized fractures in oolitic grainstone in lower Carmel Formation with fracture margins that show fractures following grain boundaries and cutting grains.

ANALYSIS

Fault Zone Behavior and Geomechanical Modeling

In previous sections of this study, we show that the Iron Wash fault is a complex zone of faults, fractures, and folds. We describe and characterize fault linkage structures along the fault and provide data on the internal strain accommodation within these

structures. We have described the architecture of the fault zone and the fault facies found as different rocks are juxtaposed. We provide evidence that the fault zone has experienced multiple types and generations of fluid movement resulting in mineralization and alteration along faults and fractures. Here, we synthesis these data from field observations and petrographic analysis and combine them with geophysical and petrophysical observations to develop three different types of fault models.

These models were developed for three purposes: 1) to recreate the geometry of the fault in the subsurface, 2) to predict fault zone behavior as a seal to fluids, and 3) to predict the geomechanical response of the fault zone in an imposed stress field and while increasing the effective stress on the fault. The goal of the geometric recreation is to reproduce a possible subsurface geometry of the fault zone and the composition and juxtaposition relationships of rocks that are faulted in the area. These modeled fault properties and lithologic characteristics are then used as input for models and used to make predictions about fault behavior with respect to fluid migration. Geomechanical models are subjected to an imposed stress field to predict the nature of failure along the fault and the formation of fracture networks. The models produced for this study are one of several realizations of what are likely several allowable interpretations of the data available and are presented to provide insight into how surface and subsurface data can be combined to provide insight into the complexity of the subsurface.

Model Inputs and Design

Geometric recreation models incorporate data from field observations, subsurface geophysics and borehole data and geometrically restored formations that were eroded

from the field area. Oil and gas exploration well and drill hole data is compiled using the software package IHS Petra (www.ih.com). This project uses the existing framework of a previous project developed by Barton (2011) at Utah State University that was focused on restoration of the Navajo Formation. Formation tops are added to the project to complete the stratigraphic column for the wells in the area, using formation top data from Utah Division Oil, Gas and Mining (www.oilgas.ogm.utah.gov), by investigating individual well reports for additional tops data, and by picking tops from wireline logs. This project used a total of 675 drillholes within the database and utilized a total of 328 drillholes located adjacent to the field area (Appendix A). A type log for the area is produced to act as a guideline for other picks in the area (Figure 43). Gridding of the formation tops is performed using various gridding algorithms: highly connected features method, disconnected features method, least squares method, linear projection method, and minimum curvature method (see Tearpock and Bischke, 2003 for description of methods). Final versions of the structural contour maps are produced using a minimum curvature gridding method because it produced the best results based on the density of the data being gridded. Minimum curvature gridding produces smoothed grids that were interpreted to be most representative of the formations at depth and it worked well in an area with only one major fault.

Subsurface Contouring

A structure contour map of the top of the Navajo Formation, the primary unit of interest in this study as an analog to a potential CO₂ reservoir (Figure 44), shows that top of the Navajo Sandstone defines a broad, low amplitude (~300 m high) anticline that has

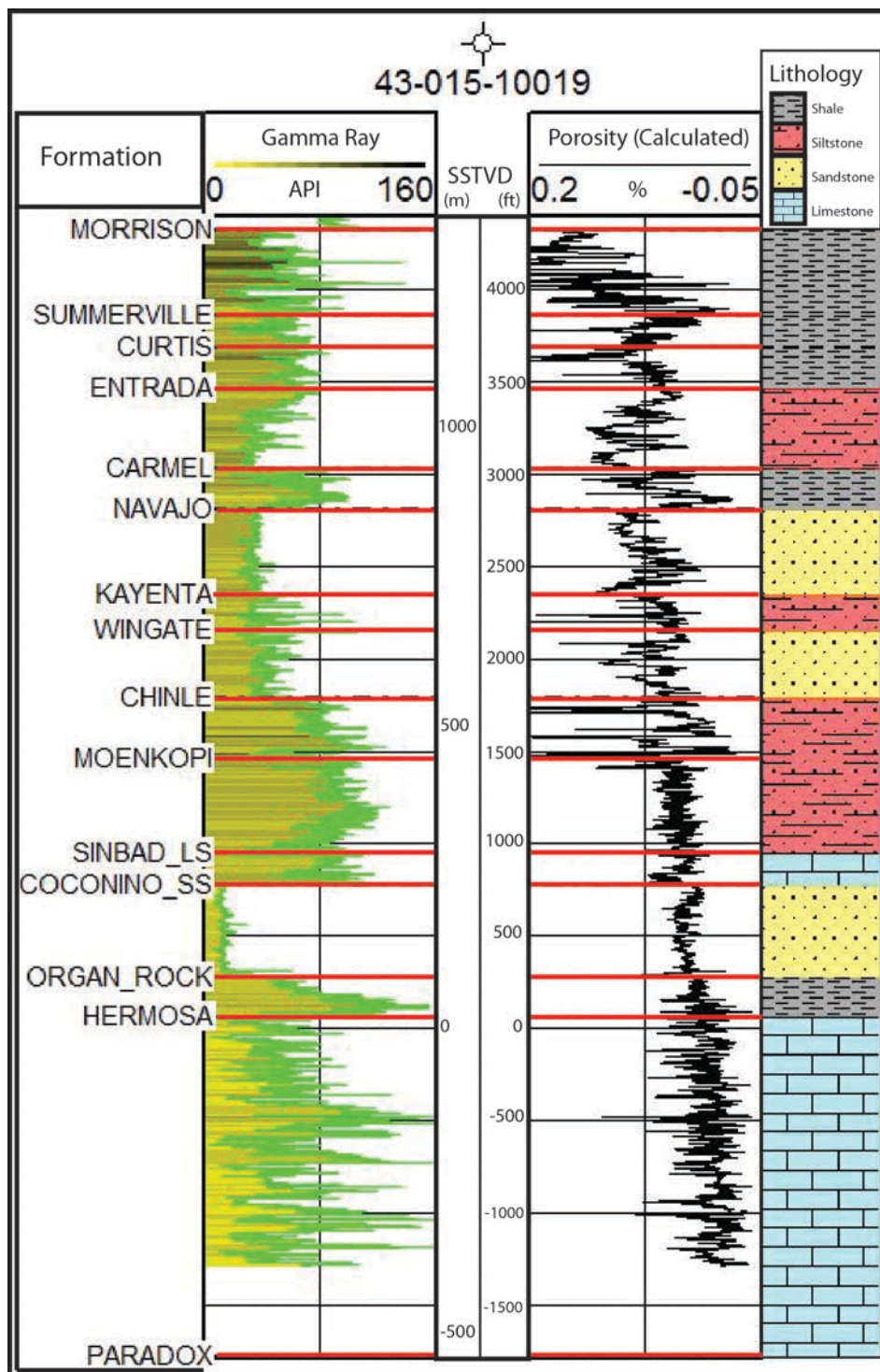


Figure 43. Generalized type log for the San Rafael Desert from exploration drill-hole API# 43-015-10019. Left track shows a gamma-ray curve and center track shows calculated porosity curve. Annotations show generalized lithology and formations tops from the Morrison to the top of the Paradox Formation (data from Utah Division of Oil, Gas, and Mining, <http://oilgas.ogm.utah.gov>).

a fold axis oriented $\sim 300^\circ$ with a plunge $< 5^\circ$ (Figure 44). The geometry of this anticline and the folded sedimentary package is seen in a well correlation cross-section along with the location of the Iron Wash fault (Figure 45). The northwest-trending regional anticline has been referred to as the Nequoia Arch (Heylmun, 1964; Baars, 1987) and a smaller anticline located in the vicinity of the Iron Wash fault is referred to as the Iron Wash Arch (Figure 46; Heylmun, 1964). The Iron Wash fault is located on the northeastern flank of this anticline (Figure 44) and appears to offset units at least 800 m deep based on the available borehole data adjacent to the fault (Figure 45). Although no boreholes adjacent to the Nequoia Arch penetrate the crystalline basement, based on the deepest boreholes in the area, it appears that basement would be no more than 300-500 m deeper than the maximum depth of boreholes in the Nequoia Arch area. Thickness of the Navajo Sandstone varies between 150-230 m within the gridded area and is as deep as 1100 m as measured from the surface. Restoration of the Navajo Sandstone where it is eroded above the San Rafael Swell was performed by using elevations of stratigraphically deeper units and restoring elevations of the Navajo Sandstone based on the thickness of the rock column above the units that have not been eroded (Figure 44).

The Nequoia Arch was a target of oil and gas exploration in the 1950's and 1960's (Figure 46) and is parallel to the structural trend of the Uncompahgre Uplift to the north and the Four Corners lineament to the south (Heylmun, 1964; Baars, 1987). Altered rocks within the San Rafael Swell have been well documented due to their importance in mineral exploration and economic ore deposits (Hawley et al., 1968). Extensive alteration of the Moenkopi Formation was identified within the San Rafael Desert and into the San

Rafael Swell (Hawley et al., 1968). The structural high of the Moenkopi Formation is co-located with the extent of bleaching in this unit (Figure 47).

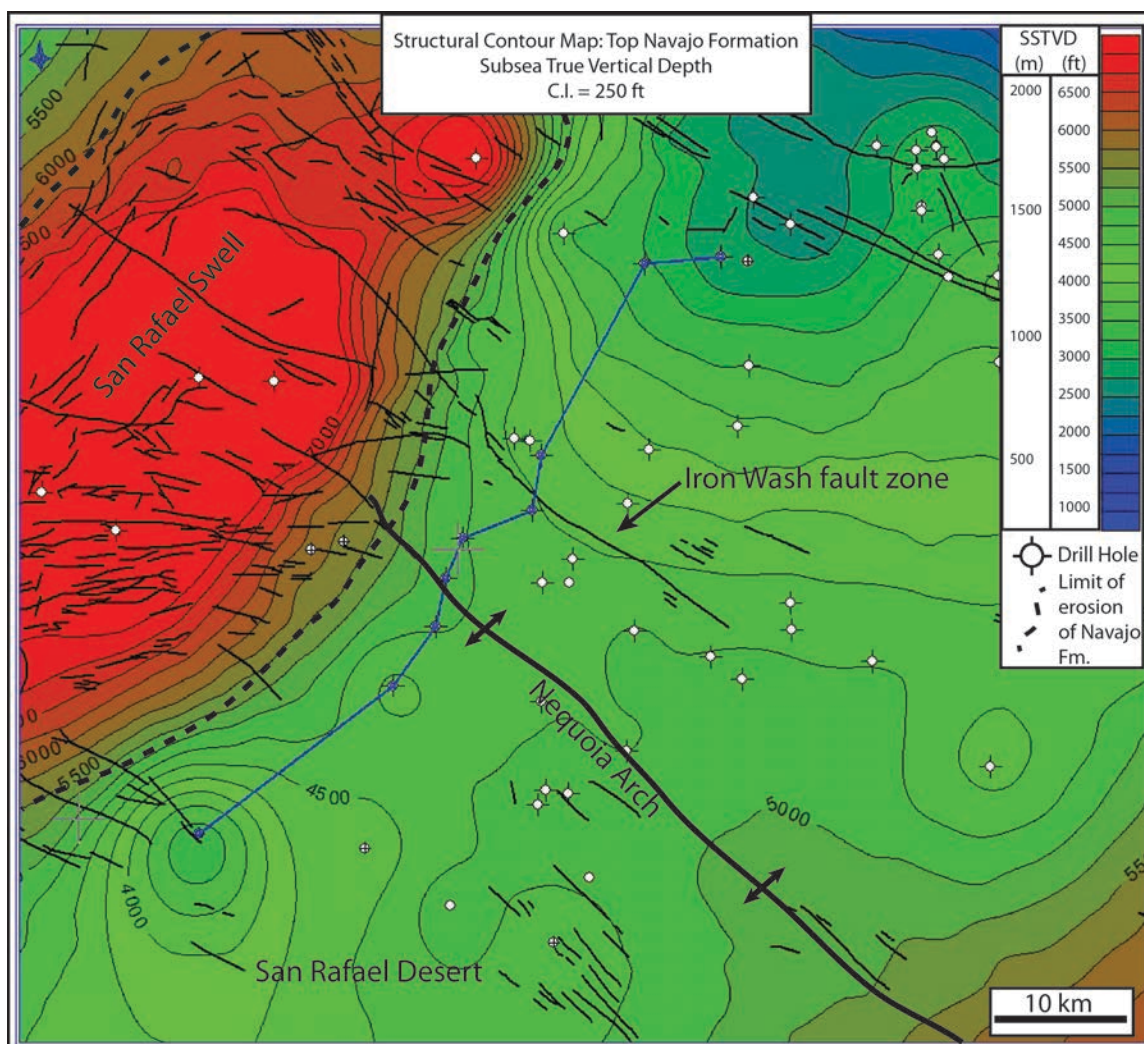


Figure 44. Structure contour map of the top of the Navajo Formation. Data is contoured in true vertical depth and gridded from formation top data. Within the San Rafael Swell contours are projected into the air using estimated thickness of eroded units (data from Utah Division of Oil, Gas, and Mining, <http://oilgas.ogm.utah.gov>). Blue line shows location of cross section in Figure 45.

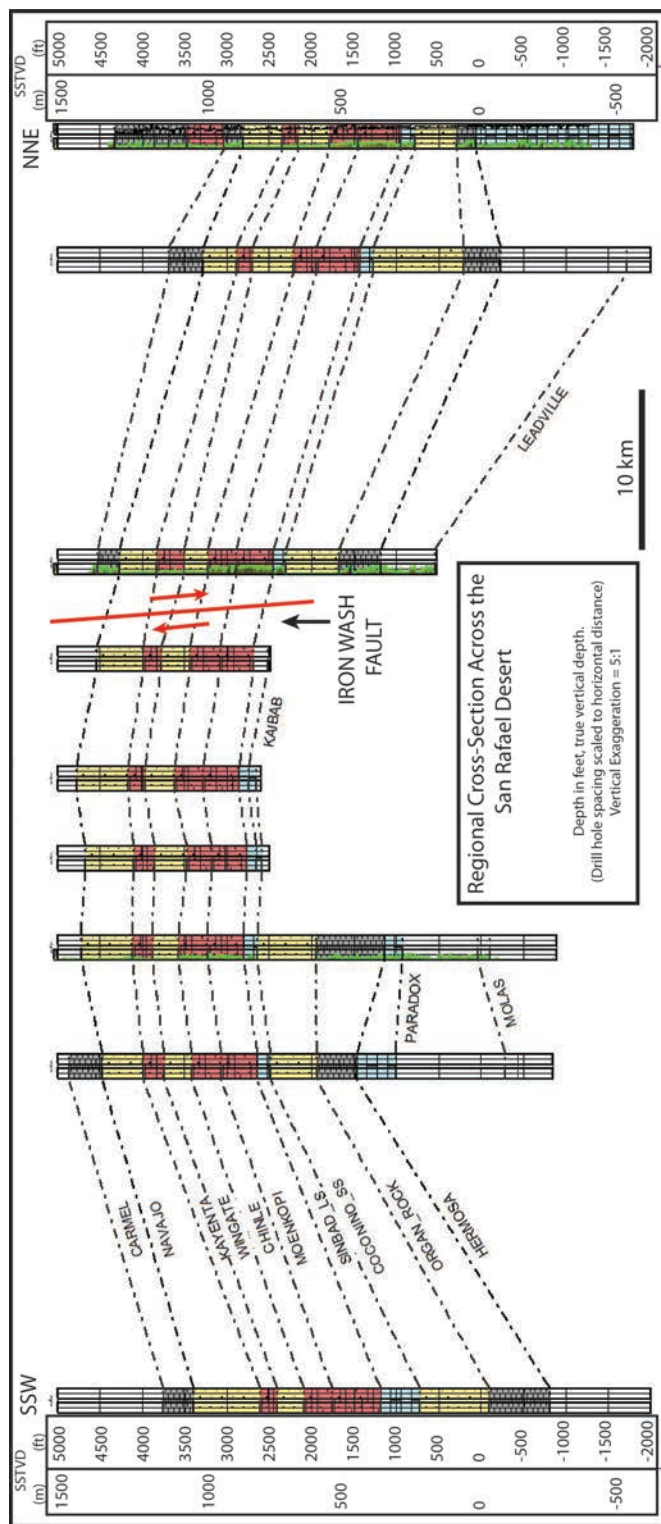


Figure 45. Well log correlation across the Nequoa Arch. Structural relief of the arch is ~500 m. Location of cross section shown in Figure 44 (data from Utah Division of Oil, Gas, and Mining, <http://oilgas.ogm.utah.gov>).

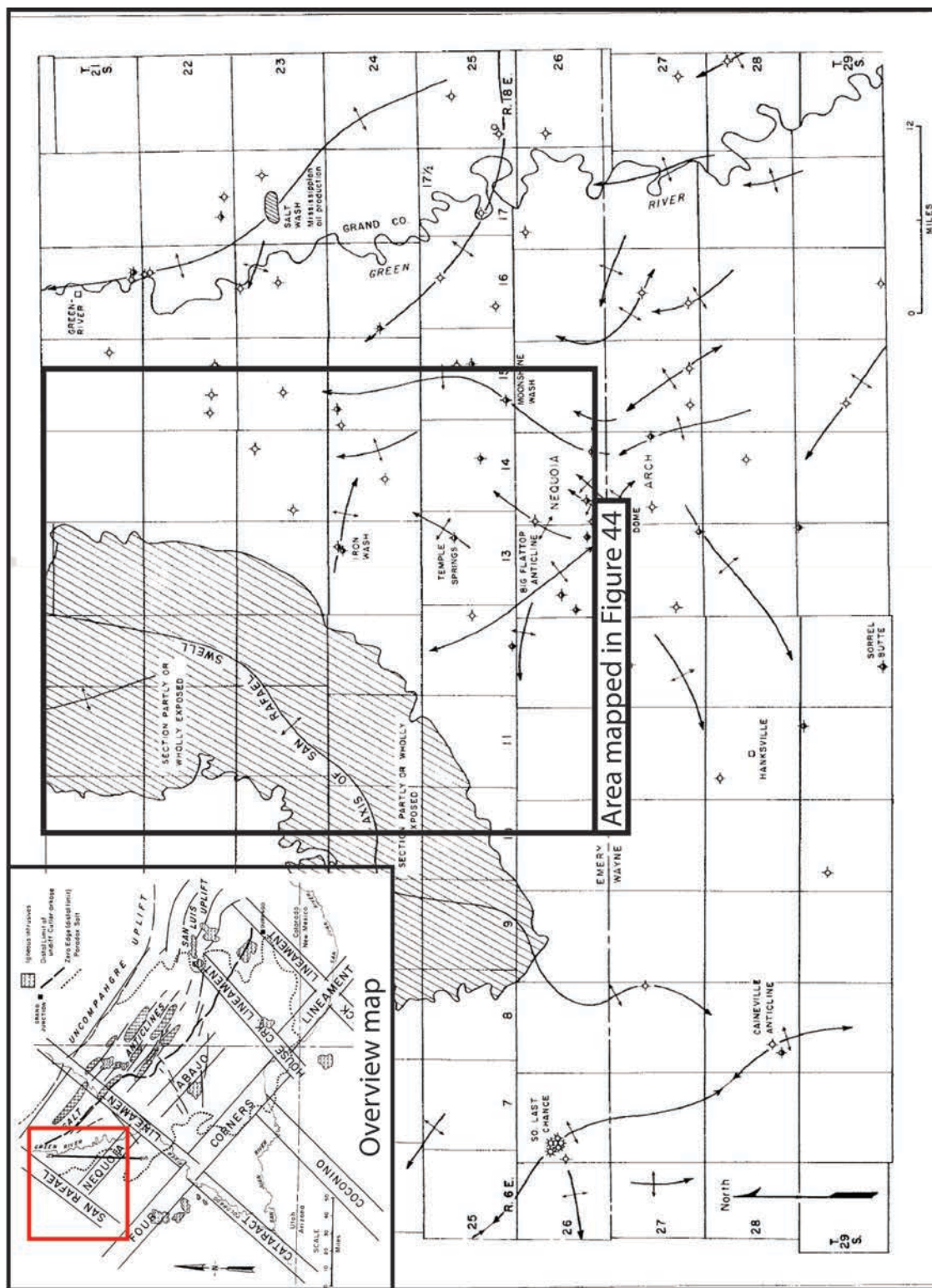


Figure 46. Oil and gas exploration map of the San Rafael Swell and Desert showing the Nequoia Arch (modified from Heylmun, 1964; Baars, 1987).

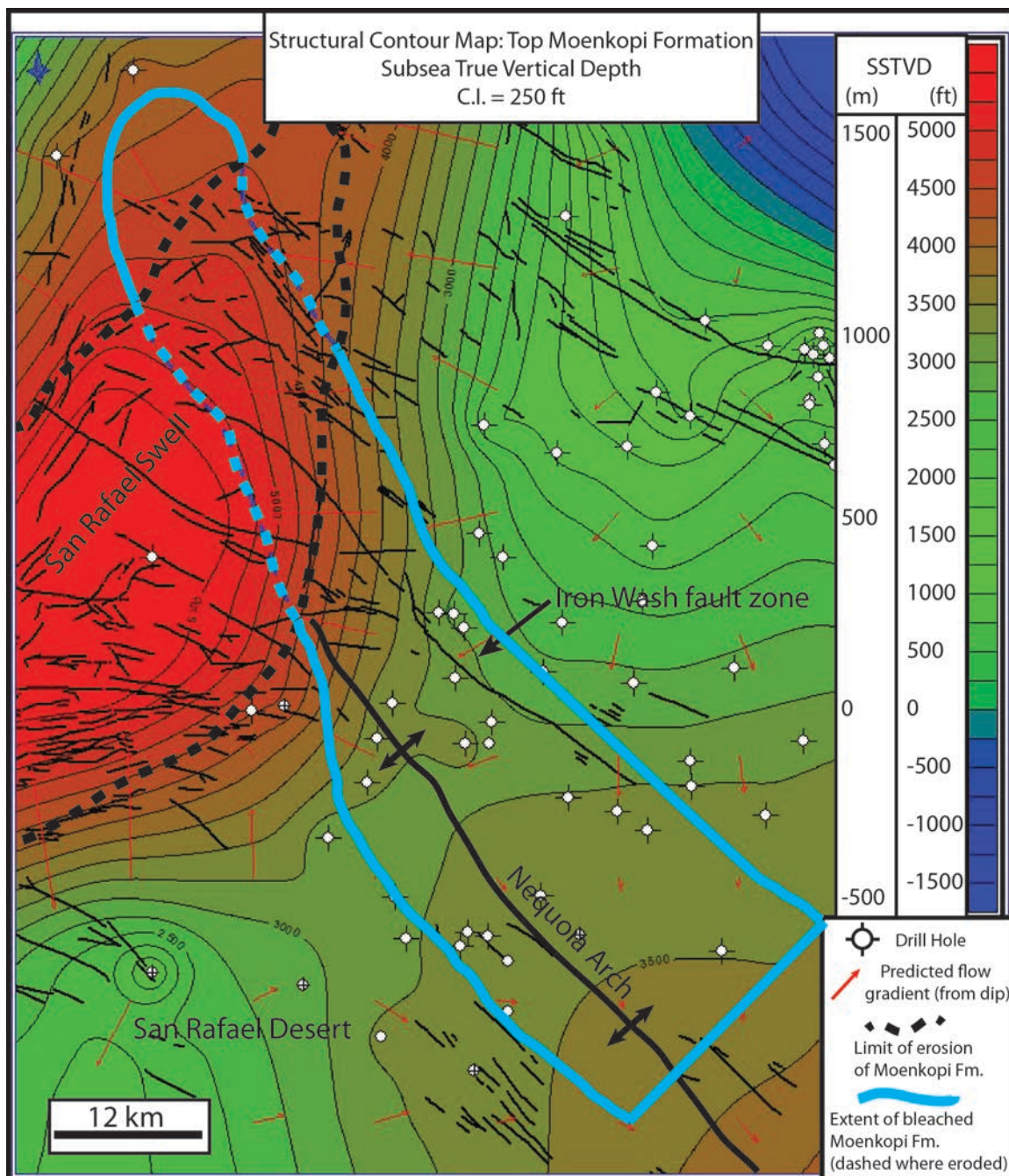


Figure 47. Structure contour map of the top of the Moenkopi Formation outline of the approximate extent of bleaching in the Moenkopi Formation. Data is contoured in true vertical depth gridded from formation top data, blue polygon shows extent of bleaching in the Moenkopi Formation and is approximated by dashes where the unit is eroded. Within the San Rafael Swell contours are projected into the air using estimated thickness of eroded units (modified from Hawley et al., 1968; data from Utah Division of Oil, Gas, and Mining, <http://oilgas.ogm.utah.gov>).

Fault Permeability Modeling

Gridded surfaces derived from well and borehole data were transferred to TrapTester™, a three-dimensional modeling program designed specifically for modeling characteristics of fault zones and fluid-fault interactions (www.badleys.co.uk). A simple model of the Iron Wash fault was created by projecting the fault surface to depth by creating a tri-mesh surface at a dip of $\sim 65^\circ$ (Figure 48). A shallower dip was used in the fault model than the average dip of $\sim 75^\circ$ measured at the surface because we assume the fault has a slightly listric geometry at depth. Key stratigraphic surfaces of the tops of the Morrison Formation, Navajo Formation and Kayenta Formation were input into the model from gridded surfaces derived from well and borehole data to produce a model of the rocks cut by the fault (Figure 48). Wireline log data were tied to the gridded surfaces at key intervals and additional units were interpolated between the gridded surfaces. This simplification step in the modeling process enables us to model the entire rock column without the need to input gridded surfaces for each horizon. A gamma ray curve from the type log (Figure 43) was used to construct a shale volume curve, a calculation of the total shale volume in the formation as a percentage of the total rock volume. Many of the fault models used an existing framework of components that were modified and re-configured to produce geometries that represent the Iron Wash fault.

To simplify the modeling process the Iron Wash fault is initially modeled as a single fault surface with no additional structural features as observed in the field (Figure 48). This simple model produces a model similar to what may be imaged in a seismic expression of the fault. For this fault model, rock types and shale volume were input into the model to produce shale juxtaposition diagrams that show the lithologic juxtaposition

along the fault zone for a range of values for throw. For the Iron Wash fault there are large proportions of shale in the upper part of the sequence and dominantly sandstone in the lower portions of the sequence (Figures 43 and 49). Based on the units present and the throw of the fault, there is dominantly shale-shale juxtaposition in the upper part of the sequence and sand-shale and sand-sand juxtaposition in the lower part of the sequence (Figure 49).

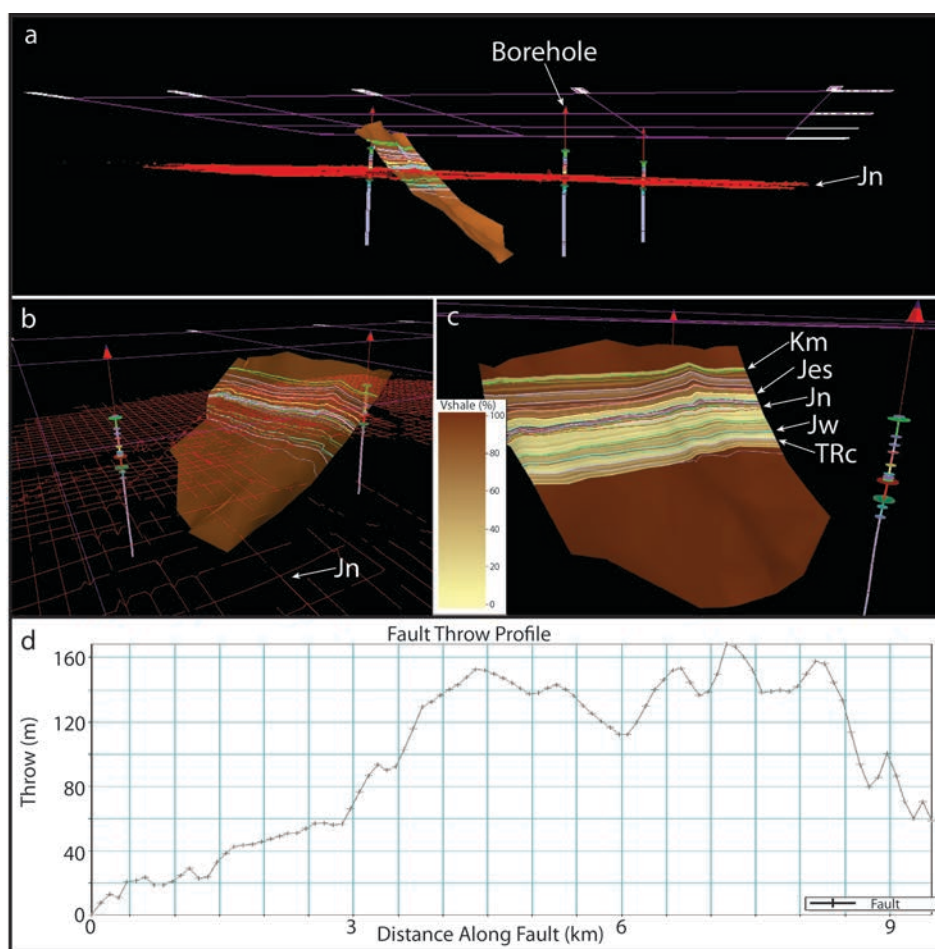


Figure 48. Overview of Iron Wash fault model design in TrapTester. a/b) Perspective views of fault model showing borehole locations with marker horizons and top of the Navajo gridded horizon, c) perspective view of the fault model showing the calculated volume of shale (V_{shale}) as a percentage projected on the fault plane and several marker horizons (see text for description of method), d) throw profile of the fault in the model.

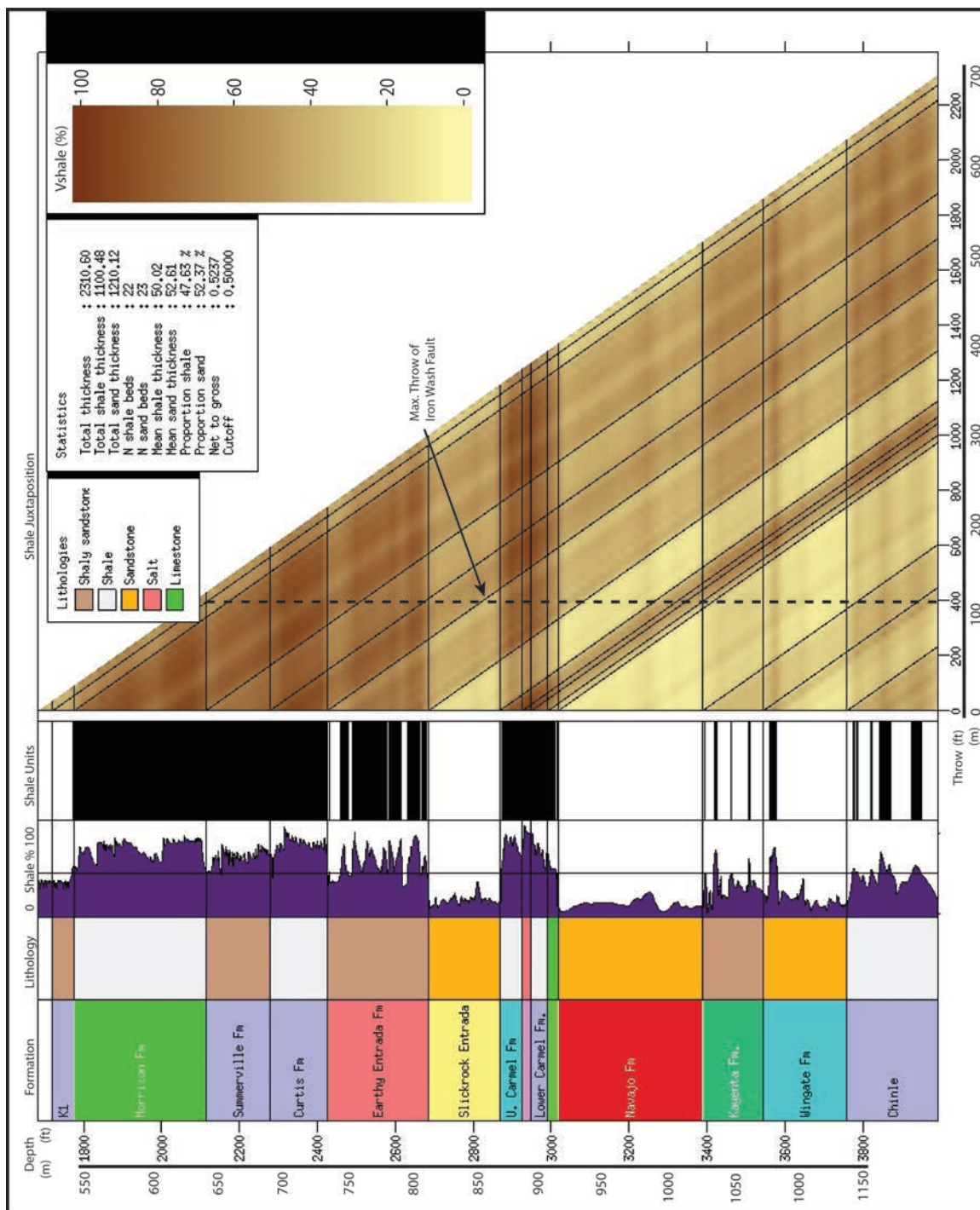


Figure 49. Triangle diagram of shale juxtaposition for the Iron Wash fault model. Shale volume calculated from V_{shale} log for fault throw between 0-700 m (see text for description of method).

From these model inputs we can analyze the seal capacity of the fault zone using proxy-properties and empirical correlations with other faults (Manzocchi et al., 1999). Shale gouge ratio (SGR) is a proxy-property based on the proportion of phyllosilicate displaced past any point on the fault (e.g. Yielding et al., 1997; Manzocchi et al., 1999). The SGR is used in combination with empirical databases to assess the ability of a fault to act as a seal and SGRs of ~15-20% have been suggested as a minimum value to produce a sealing fault membrane (Watts, 1987; Manzocchi et al., 1999). The SGR for the Iron Wash fault is calculated based on Skerlec (1996) using Eqn. 1, and is calculated for a range of values of fault throw to produce a SGR plot to show areas of the fault where seal integrity may be low due to low fault gouge development (Figure 50). Well-developed fault gouge is commonly associated with sealing faults in the subsurface, with a common cutoff for fault seal being $SGR > 30\%$, a partial sealing behavior with $15\% < SGR < 30\%$ and dominantly non-sealing faults with $SGR < 15\%$ (Skerlec, 1996). In the modeled fault SRG plot shown in Figure 50, we can see that in areas where the thick sandstone sequences dominate and only thin shale sequences are present, very low shale gouge regions are present.

$$\text{Shale gouge ratio (SGR)} = \frac{\sum [(\text{Zone thickness}) \times (\text{Zone clay fraction})]}{\text{Fault throw}} \times 100\% \quad (1)$$

Lindsey et al. (1993) developed a methodology for using shale smear factor (SSF) to predict the likelihood of continuity of shale smear along the fault. This is another proxy-property of the fault zone based on the proportion of the fault throw to the

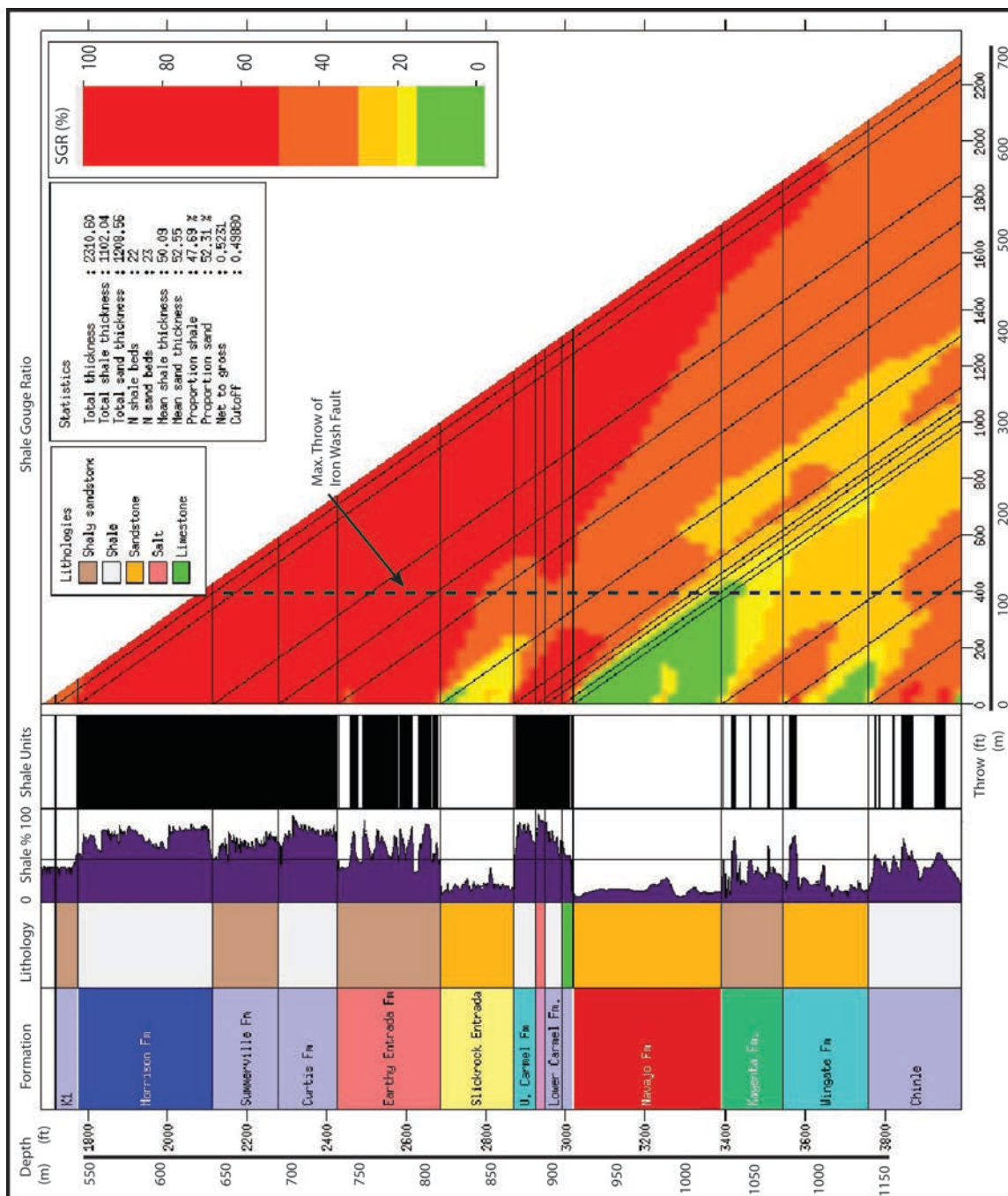


Figure 50. Triangle diagram of shale gouge ratio for the Iron Wash fault model. Shale gouge ratio calculated from V_{shale} log for fault throw between 0-700 m (see text for description and method).

thickness of shale in the sequence. The SSF is used in a similar manner as SGR to predict the sealing behavior of faults where lower values of SSF result in more complete shale smear along the fault and therefore higher sealing potential.

The SSF is calculated for the Iron Wash fault (Figure 51) based on Lindsey et al. (1993) using Eqn. 2 and is calculated for a range of values for fault throw. In the modeled fault SSF plot, high in the sequence, where the rocks are dominantly shale, the SSF is low (<3.0) and the fault is predicted to behave as a seal. Lower in the sequence, where sandstone reservoirs are present, we calculate $0.3 < \text{SSF} < 6.0$ and predict a partial sealing behavior. Hence, also with this method there is a substantial part of the fault that is not predicted to seal with $\text{SSF} > 6.0$.

$$\text{Shale smear factor (SSF)} = \frac{\text{Fault throw}}{\text{Shale layer thickness}} \quad (2)$$

Based on the plots for SGR and SSF, it appears that the fault would most likely behave as a seal where the fault juxtaposes units above the Earthy Member of the Entrada Formation, where the sequence is dominated by units with >50% shale (Antonellini and Aydin, 1994; Yielding et al., 1997; Manzocchi et al., 1999; Shipton et al., 2002). In the middle part of the stratigraphic sequence, there is transition zone from dominantly shale units to dominantly sandstone units (Figure 51). In this transition zone, the fault is predicted to behave as a partial seal in the sand-shale sequence of the Slickrock Member of the Entrada Formation and the Carmel Formation. Below the transition, where the fault

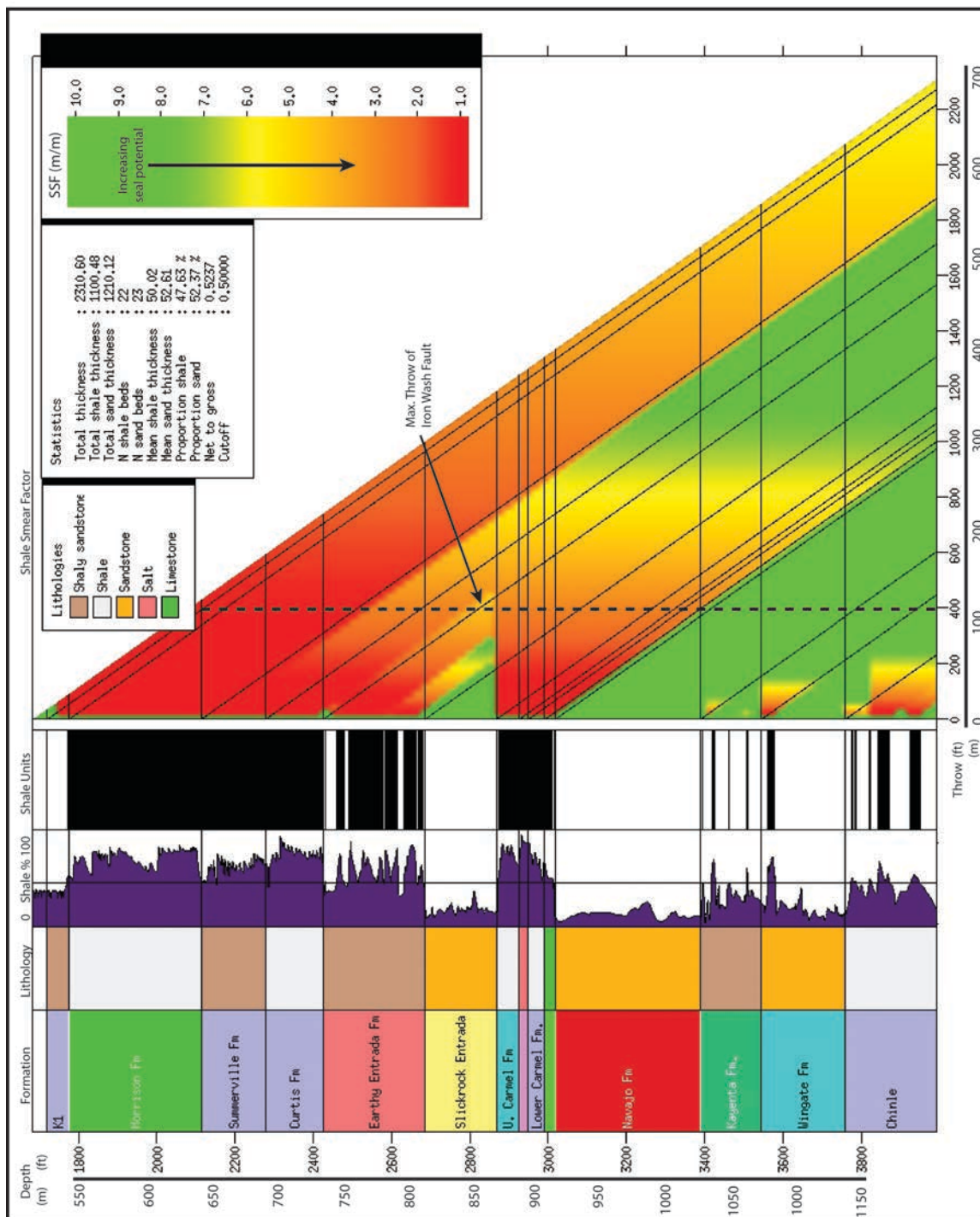


Figure 51. Triangle diagram of shale smear factor for the Iron Wash fault model. Shale smear factor calculated from V_{shale} log for fault throw between 0-700 m (see text for description and method).

juxtaposes rocks that are generally <50% shale, the fault is not predicted to act as a seal (Figure 51).

From the calculated values determined for SGR, fault zone permeability is calculated for the Iron Wash fault (Figure 52) using Eqn. 3 and the method determined by Manzocchi et al. (1999). Modeled values for permeability are based on the SGR plots and empirical values for the fault permeability based on the amount of shale gouge present. The lower part of the sequence in the fault zone with greater sandstone content and higher initial permeability has higher modeled fault zone permeability, generally >0.04 mD. In the upper part of the sequence, the fault has low modeled permeability, generally <0.01 mD. These values provide a quantitative measure of the sealing behavior of the fault based on the more qualitative SGR measurement. Recent work suggests that for a given porosity, permeability is higher in host rock than in fault core slip zones and slip surfaces, and that as the amount of deformation increases, permeability decreases (Antonellini and Aydin, 1994; Shipton et al., 2002; Torabi et al., 2013).

$$\text{Average Permeability} = \log(k) = 4\text{SGR} - \frac{1}{4}\log(\text{Fault throw})(1 - \text{SGR})^5 \quad (3)$$

Shale gouge ratio has been related to across fault pressure difference (AFPD) by using empirical databases that are used to calibrate the relationship between fault-seal attributes and capillary fluid properties (Bretan et al., 2003). The calibration of SGR against AFPD used robust datasets but each fault is geologically unique and therefore is only an predication of the possible fault zone capillary entry pressure (FZP), also

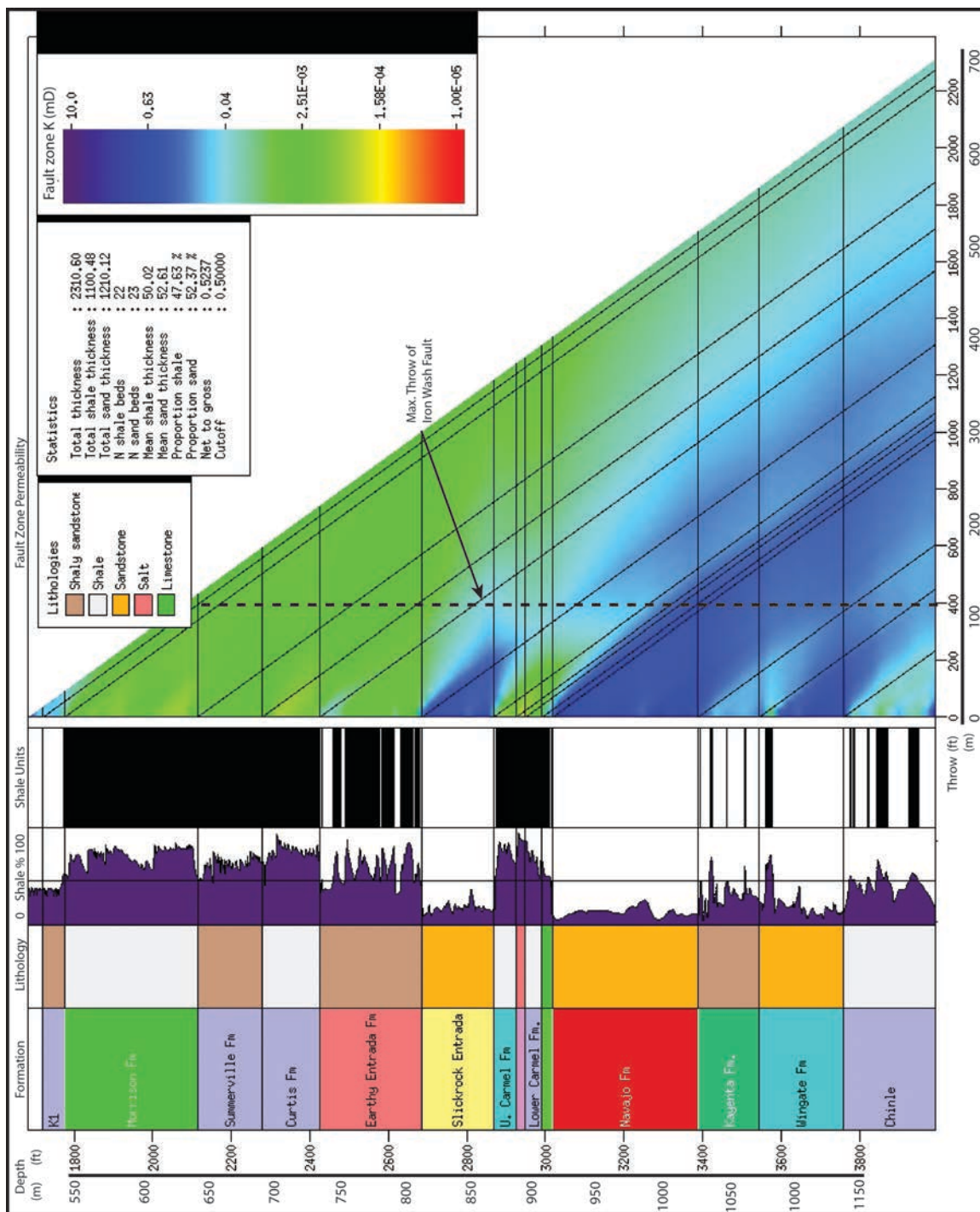


Figure 52. Triangle diagram of fault zone permeability for the Iron Wash fault model. Fault zone permeability diagram calculated from V_{shale} log and shale gouge ratio for fault throw between 0-700 m (see text for description and method).

commonly referred to as across fault pressure difference (AFPD). The FZP is strongly dependent on which fluid types are juxtaposed by the fault (e.g., oil against water or gas against water), the depth of burial, and the estimate of the clay content of the fault zone (Bretan et al., 2003). Capillary entry pressure for supercritical CO₂, assuming a density of 550 kg/m³, is calculated for the Iron Wash fault (Figure 53) using the method determined by Breten et al. (2003) using Eqn. 4. The value for C in Eqn. 4 is a depth-dependent term that was set equal to 0.5 for all calculations in this study as all burial depths are <3.0 km. These calculations assume that as pressure builds up on one side of the fault and that the dominate mechanism of seal bypass is through capillary action through the fault zone. Modeled FZP for the faulted units of the Slickrock Member of the Entrada Formation generally have low entry pressure of <2 MPa (Figure 53). Stratigraphically higher, the modeled FZP for the faulted units including the Earthy Member of the Entrada Formation generally have high entry pressure of >8 MPa (Figure 53).

$$\text{Fault zone capillary pressure (FZP)} = 10^{\left(\frac{SGR}{27} - C\right)} \quad (4)$$

The potential hydrocarbon column height (H) is the height of a column of fluid or gas that can be supported against a fault before the capillary entry pressure is exceeded and the fault no longer acts as a seal (Bretan et al., 2003). Empirical relationships between SGR and AFPD are used to predict the hydrocarbon column height that the fault may be able to support at different levels within the fault units (Childs et al., 2002; Bretan et al., 2003). The value H is expressed as the maximum column height of a fluid with a

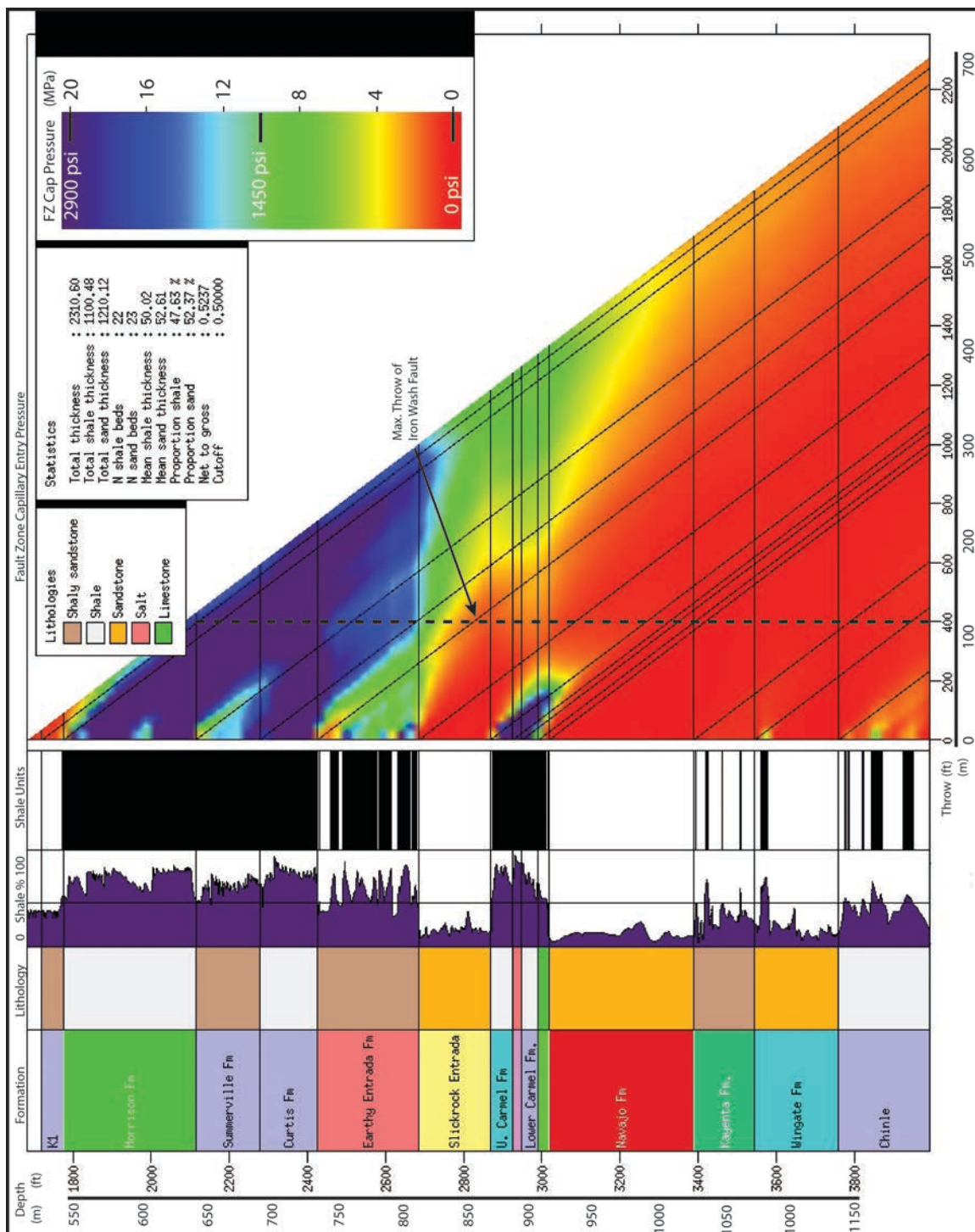


Figure 53. Triangle diagram of fault zone capillary entry pressure for the Iron Wash fault model. Fault zone capillary entry pressure calculated from V_{shale} log and shale gouge ratio for fault throw between 0-700 m (see text for description and method).

known density that is buoyantly driven to float above a water-saturated reservoir. The model incorporates a fault with calculated proxy-properties (SGR) and a calculated fault capillary entry pressure (AFPD). Potential CO₂ column height is calculated for the Iron Wash fault using the same methodology developed for prediction of hydrocarbon column heights (Jennings, 1987; Bretan et al., 2003, Bretan et al., 2011) using Eqn. 5. Column height is calculated using FZP which was previously calculated, ρ_w is the pore-water density (1000 kg/m³), ρ_h is the hydrocarbon density for which we substitute supercritical CO₂ density in our model (550 kg/m³), and g is gravitational acceleration (9.81 m/s²) (Bretan et al., 2003; Bretan et al., 2011). The maximum column height is a result of the buoyancy driven effect of a lower density fluid (like CO₂ or oil) with respect to the water or brine in the reservoir. The column height is a maximum height at any point along the fault zone and can be used in conjunction subsurface fault mapping to predict when a leak point along strike of the fault might be predicted. The predicted maximum CO₂ column height is >60 m for most areas of the Iron Wash fault where significant volumes of shale are predicted in the fault zone (Figure 54). Where the volume of shale gouge predicted is low, the maximum CO₂ column height is predicted to be only 10-30 m (Figure 54).

$$\text{Fluid column height } (H) = \frac{FZP}{g(\rho_w - \rho_h)} \quad (5)$$

The methodology for using shale gouge ratio in the calculation of FZP and fluid column height was initially developed to predict these properties in systems where the

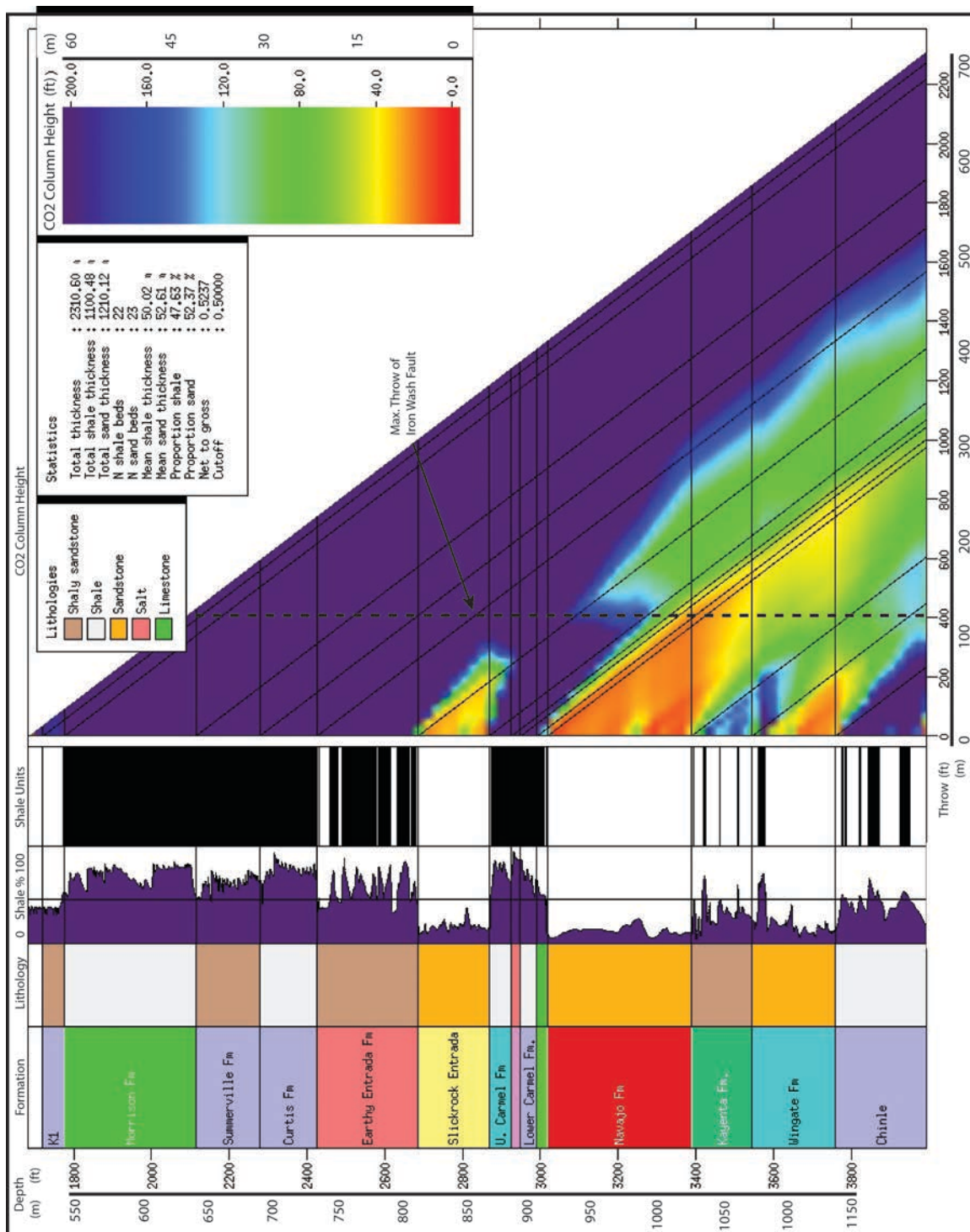


Figure 54. Triangle diagram of predicted maximum CO₂ column height for the Iron Wash fault model. Predicted maximum CO₂ column height diagram calculated from fault zone capillary entry pressure and assuming a density of CO₂ = 550 kg/m³ for fault throw between 0-700 m (see text for description).

dominate fluids are hydrocarbon and brine. It has been recently applied to systems where CO₂ is injected resulting in a CO₂-brine system (Bretan et al., 2011), but some uncertainty remains in this new application of the method. The calculation of capillary entry pressure is dependent on the wetting angles of the fluids in the system and Eqn. 4 assumes a wetting angle of zero in the oil-water system (Bretan et al., 2003). However, because the wetting angle in a CO₂-water phase may range as high as 60° at pressures of 10 MPa, the predicted capillary entry pressure and column heights would be reduced by a factor of 50% (Bretan et al., 2011). Additionally, the interfacial tension between two phases in an aquifer, such as in a system with CO₂ and brine, will influence the resulting capillary entry pressure and is a pressure-temperature dependent relationship (Torabi et al., 2013). These factors has not been included in the calculations in this study as this will introduce model complexities that our data cannot address or test. Because the process of prediction of column heights is dependent on the density of the fluid, an understanding of the pressure and temperature regime becomes much more important when dealing with a supercritical fluid such as CO₂ (Antonellini and Aydin, 1994; Yielding et al., 1997; Manzocchi et al., 1999; Shipton et al., 2002).

Geomechanical Models

We calculate likelihood of fault failure in the subsurface as the pressure would be increased on the fault surface, as would be expected in the case where fluids, such as CO₂, were being injected against one side of the fault surface. To do this, the basic model has a state of stress consistent with the general state of stress in the Colorado Plateau stress field (Figure 55; Patton and Zandt, 1991; Flesch and Kreemer, 2010). Stress

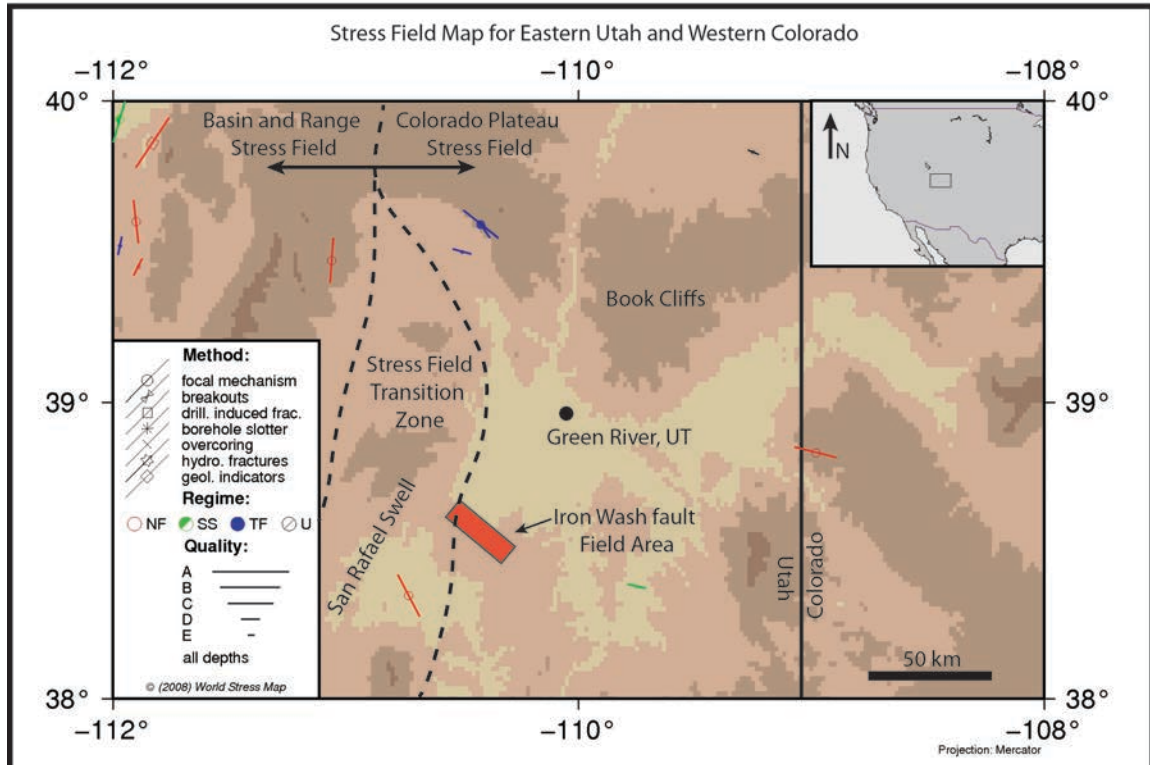


Figure 55. Stress field map of eastern Utah and western Colorado. Dashed line approximates the transition zone between the Colorado Plateau stress field dominated by north-northeast extension and the Basin and Range stress field dominated by east-west extension (Patton and Zandt, 1991; Flesch and Kreemer, 2010). Red box indicates location of the Iron Wash fault field area.

orientations were determined from the world stress map project (www.world-stress-map.org) and stress magnitudes were calculated assuming that the crust is at a critically stressed state (e.g. Barton et al., 1995). Stress notation used here is $S_v > S_{Hmax} > S_{Hmin}$ where S_v is the principal stress and is assumed to be vertical and S_{Hmax} and S_{Hmin} are the maximum and minimum horizontal stresses, respectively. Vertical stress is assumed to be the lithostatic gradient of 24 MPa/km, the minimum horizontal stress is calculated based on Anderson (1951) as 15 MPa/km using Eqn. 6 by assuming a Poisson's ratio, $\nu = 0.25$. The maximum horizontal stress, S_{Hmax} , is assumed to be 18 MPa/km, or slightly less than

the mean stress, however, because we were interested in the differential stress for all cases, this value was not important in the modeling process. Models are produced assuming both a cohesionless material and a material with a cohesion of 5 MPa and with a Coulomb failure envelope defined by a coefficient of internal friction, μ , of 0.60 and 0.4. The pore fluid pressure gradient is assumed to be 10 MPa/km in the nominal state and is varied to understand the influence of an increase in pore pressure on predicted failure of the materials.

$$S_{hmin} = \left(\frac{\nu}{1 - \nu} \right) (S_V - Pp) + Pp \quad (6)$$

We show geomechanical models of fault failure tendency contoured with the dilation tendency (the tendency of a fracture to open as a mode 1 fractures). We conclude that in all cases modeled for cohesionless faults, rocks with a coefficient of internal friction of $\mu = 0.4$ are predicted to be in failure and additional fault orientations are predicted to fail as pore pressure increases (Figure 56). Model results show that with increasing depth, no failure is predicted based on a constant pore pressure and $\mu = 0.6$ (Figures 56a and b). As pore pressure is increased and depth is held constant, failure is predicted in about half of the fault orientations with an increase in pore pressure of 2 MPa/km. As pore pressure is increased to 15 MPa/km, equal to the minimum horizontal stress, the majority of fractures are predicted to fail (Figure 56d). The second model is produced for a material cohesion of 5 MPa predicts no failure at pore pressures up to 12 MPa/km for rocks with $\mu = 0.4$ or 0.6 (Figures 57a and b). As pore pressure is increased

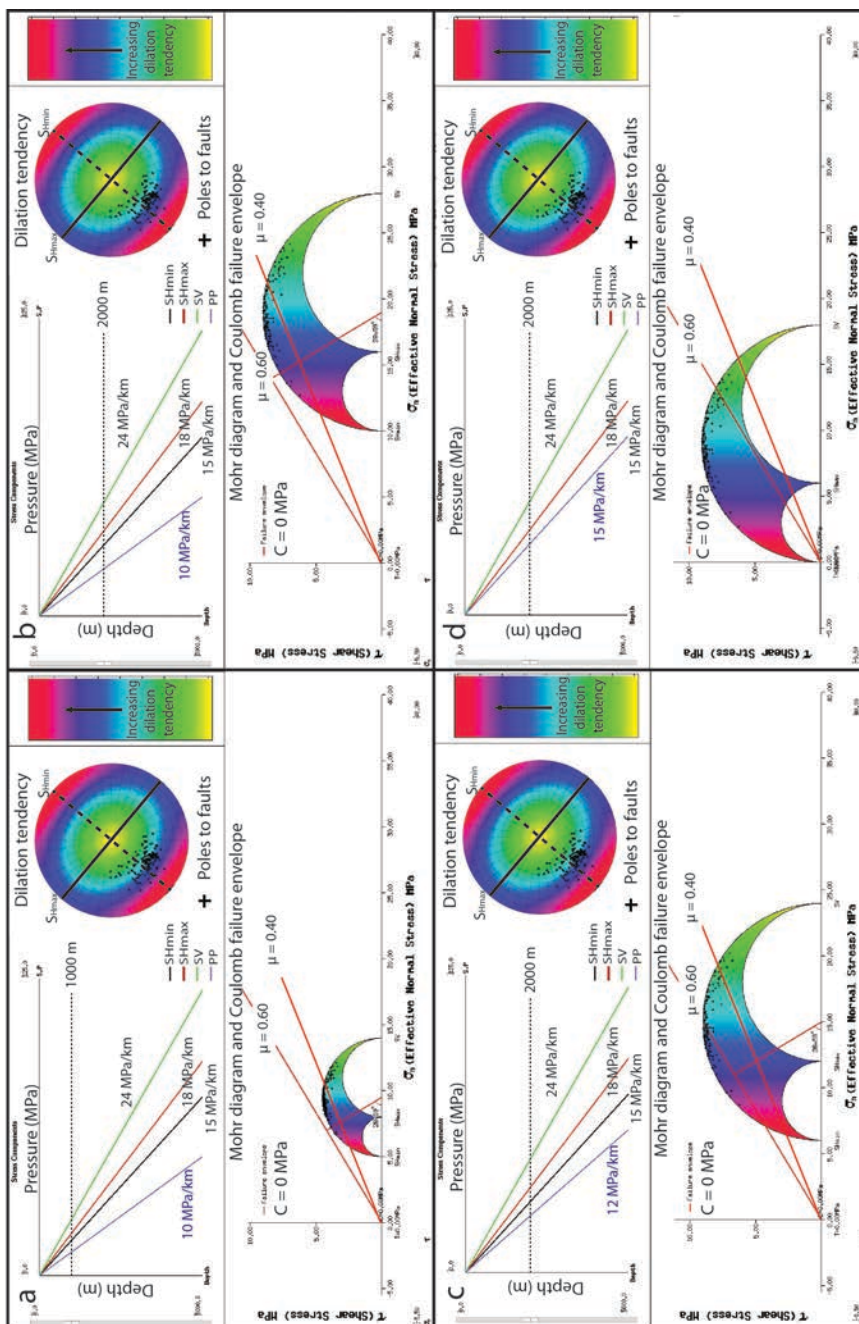


Figure 56. Geomechanical plots with components used in predicting fault failure along the Iron Wash fault for cohesionless faults. Plots each display the principal stresses and pore fluid pressure plotted with depth, stereonet with poles to faults and horizontal stresses, and Mohr-Coulomb failure diagrams. Models are for a cohesionless material with an internal coefficient of friction of $\mu = 0.6$ and $\mu = 0.4$. Color contours are dilatation tendency. a) 1000 m depth and 10 MPa/km pore pressure gradient, b) 2000 m depth and 10 MPa/km pore pressure gradient, c) 2000 m depth and 12 MPa/km pore pressure gradient, and d) 2000 m depth and 15 MPa/km pore pressure gradient. See text for discussion.

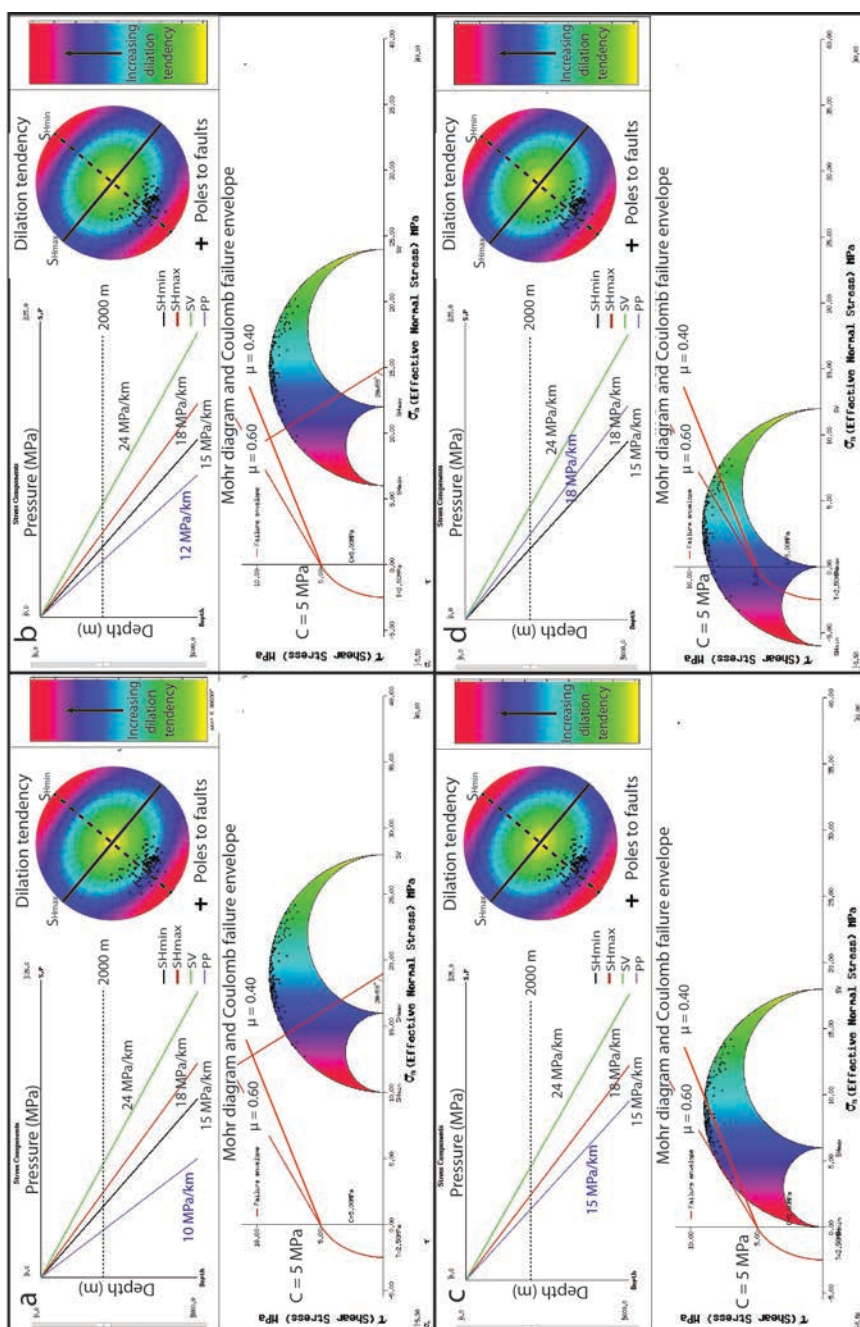


Figure 57. Geomechanical plots with components used in predicting fault failure along the Iron Wash fault for faults with cohesion of 5 MPa. Plots each display the principal stresses and pore fluid pressure plotted with depth, stereonet with poles to faults and horizontal stresses, and Mohr-Coulomb failure diagrams. Models are for a material with a cohesion of 5 MPa and with an internal coefficient of friction of $\mu = 0.6$ and $\mu = 0.4$. Color contours are dilation tendency. a) 2000 m depth and 10 MPa/km pore pressure gradient, b) 2000 m depth and 12 MPa/km pore pressure gradient, c) 2000 m depth and 15 MPa/km pore pressure gradient, d) 2000 m depth and 18 MPa/km pore pressure gradient. See text for discussion.

to 15 MPa/km, rocks with $\mu = 0.4$ are predicted to fail and rocks with $\mu = 0.6$ approach the failure envelope but are not predicted to fail. With a pore pressure of 18 MPa/km, equal to the maximum horizontal principal stress, failure is predicted in most of the fault orientations for all values of μ .

DISCUSSION

The Iron Wash fault study area is an exposed analog to potentially targeted CO₂ injection reservoirs and top-seals where faults are present and faults may represent potential leakage and migration pathways for fluids. Our case study is an exposed analog of faulted reservoir-caprock systems in the form of structural intersection, fault relays, fault-related folds, fault lenses and internal fault architecture. The goal of this project was to study a natural analog of a potential injection target for geologic storage of CO₂ in the subsurface. The project focused on analogous reservoir-seal units that are present within the Nequoia Arch and adjacent to the larger San Rafael monocline, both of which are analogous to typical structural targets for production of hydrocarbons and injection of CO₂ when found in the subsurface. The study focused around the Iron Wash fault, a ~25 km long normal fault with ~120 m of throw that has faulted along the axis of the Nequoia Arch and intersects the flank of the San Rafael monocline. The fault represent a potential seal bypass mechanism for both the lateral and vertical migration of fluids out of the Nequoia Arch and the San Rafael monocline.

We combine field observations and exploration drill hole wireline data in a model the fault geometry, sealing behavior and frictional strength to undertake a comprehensive analysis of the Iron Wash fault zone. These results are discussed in the context of an

exposed and modeled analog to faults that could potentially (and will most likely) be encountered during the planning and characterization stages of a potential CO₂ sequestration project. First we discuss field data and observations on the geometry and architecture of the Iron Wash fault zone. Evidence shows that this is a segmented fault zone surrounded by a volume of deformed rock described as inner and outer damage zones. The fault provides evidence for the migration of fluids along the fault and fractures and we discuss types of fluid movement and implications for multiple phases of fluid movement. The focus is on architectural components of the fault zone including fault relays and lenses as potential leakage points in the fault zone. By combining field data with subsurface data from drill holes in the area, we have undertaken geometric reconstructions of the fault zone and use this model in predictions about fault zone behavior and in discussions of fault sealing ability for fluids injected within a reservoir containing a fault. Finally, we discuss results from our modeling of the geomechanical implications of injection of fluids and changing pressure conditions surrounding a fault zone.

Fault Architecture, Facies and Damage Zone

The Iron Wash fault zone shows examples of both hard-linked and soft-linked fault relay structures. These structures are generally more common in the northwestern segments of the Iron Wash fault (Figure 58). Both the hard and soft-linked relay zones are unique in their geometry, orientation, linkage style and internal deformation (Figure 59). The fault and fracture development in the soft-linked relay zone appears to be controlled by a localized three dimensional strain field resulting from the stress influence

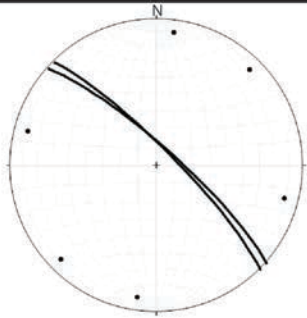
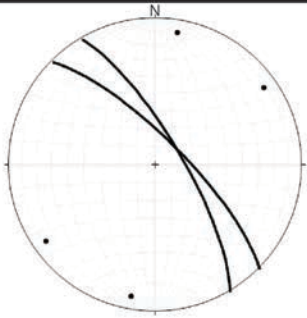
	Hard-linked Relay	Soft-linked Relay
Dominant Fault and Fracture Orientations	 / Faults ● Poles to Fractures	 / Faults ● Poles to Fractures
Fault Intersection Angle	3°	18°
Fault Overlap Distance	750 m	560 m
Fault Separation	205 m	120 m
# Faults Within Relay (Throw > 50 cm)	5	1
Relay Width (center)	205 m	120 m

Figure 59. Summary of the two fault relay systems studied at the Iron Wash fault zone.

of each of the primary slip surfaces surrounding the relay zone (Figure 59). Fracture orientations within the relay zones differ from those found outside of relay zones in the damage zone of the Iron Wash fault (Figure 59). Increased fracture intensities and different orientations is qualitatively believed to open better potential pathways for fluids to migrate through relay zones and fault lenses and is supported by observed fluid-related features co-located with structural complexities of the fault zone (Figure 58). Because the faults each have no measureable offset away from the relay zone, we would predict no

fault seal beyond the fault tips and therefore no fault seal across the soft-linked relay laterally. Contrary, in the case of the hard-linked relay which has direct linkage of the faults, we would expect at least some degree of fault seal.

Results from this study support the idea that fault damage zones are asymmetric, being wider in the hanging wall than in the footwall, but demonstrate that this is not always the case, as seen in wider damage zones in the footwall near fault tips and within relay zones. The implications for wider damage zones on one side of the fault are that during CO₂ injection projects, a higher risk factor for leakage of fluids upwards along the fault zone could be assigned to fluids encountering a fault zone from the hanging wall side. We would expect that upwards migration along fracture networks or caprock failure due to fracturing may be more likely in the hanging wall than when compared to the footwall. This may also be helpful when planning injection sites or monitoring locations as planners would likely need to avoid these features and would need to allow for a wider stand-off spacing on the hanging wall of a fault than the footwall.

Alteration, mineralization and preservation of oil staining within fractures and joints in the fault zone have been used as indicate past migration of fluids (e.g. CO₂, brine, hydrocarbons) through fault and fracture networks. Observations about the size and intensity of the damage zone of the Iron Wash fault help to constrain the distribution of fracture networks associated with the fault. More detailed investigations of relay zones and fault lenses has yielded insight into formation of isolated fracture networks unique to areas with relay zones as well as concentration of mineralization and alteration within these areas.

The displacement-thickness ratios measured for the Iron Wash fault zone conform well with previously established relationships (Figure 19; Robertson, 1983; Hull, 1988; Evans, 1990; Shipton et al., 2006; Childs et al., 2009). Fault cores may indeed thicken with displacement (e.g. Evans, 1990; Shipton et al., 2006), but overall fault zone thickness is a function of the number of fractures and fault and is therefore dependent on where it is measured along the fault zone in relationship to the nature of the fault (i.e. at relay zones or near dip changes in the bedding being faulted) (Evans, 1990; Shipton et al., 2006). We suggest that the D:T ratio for specific regions of the Iron Wash fault lies on the upper end of the observed data from previous studies, meaning that the fault zone has greater thickness than expected based on displacement. This is observed in two areas of the fault zone: 1) at the intersection of the Iron Wash fault and the San Rafael monocline and 2) at fault tips located near relay zones (Figure 19). We suggest that these zones of decreased D:T ratio are present due to increased structural complexity and the distribution of strain as the fault loses throw, respectively. Our results support previous conclusions that when D:T relationships are used as tools to predict fault thickness based solely on fault displacement, significant uncertainty in accurate prediction of the geometry and thickness of the damage zone still remains. This study suggests that this uncertainty is magnified when additional structural complexities are present, such as the at fault tips and/or within fault relay zones.

Fault facies are interpreted to be the result of different expressions of local structural setting, mechanical characteristics of the hanging wall and footwall, the amount of slip, and the proportion of strain accommodated by the fault core and fault zone (Braathen et al., 2009). Fault facies have implications on the sealing nature of the fault

and can be used to identify potential leakage points for fluids in the fault (e.g. Antonellini and Aydin, 1994; Shipton and Cowie, 2001; Shipton et al., 2004). Fault cores that are composed of coalesced deformation bands are common where the fault juxtaposes porous sandstones where cataclastic grain crushing and deformation band slip are the dominant deformation mechanisms. These deformation bands reduce the permeability of the sandstone drastically (e.g. Antonellini and Aydin, 1994; Shipton et al., 2002; Fossen et al. 2007; Rotevatn et al., 2013) and therefore a well developed and laterally continuous fault core may behave as a baffle or barrier to fluid migration (Antonellini and Aydin, 1994; Shipton et al., 2002; Fossen et al. 2007; Rotevatn et al., 2013; Torabi et al., 2013). Areas where the fault core contains a well-developed fault gouge and clay smear are where the fault is likely to be a seal to fluid migration (e.g. Jennings, 1987; Watts, 1987; Lindsey et al., 1993; Skerlec, 1996; Yielding et al., 1997; Manzocchi et al., 1999; Bretan et al., 2003).

We describe 8 fault facies along the Iron Wash fault zone and estimate percentage of shale content based on field sampling and examination, petrographic and XRD analysis (Figure 60). Fault facies in the field are linked to the model results of shale-gouge development along the fault zone and then ranked in terms of their potential seal effectiveness using cutoffs for SGR described in previous sections (Figure 60). We define shale gouge ratio and relate it to facies observed in the field to use as a guideline to understanding and relating modeling results to field observations. We do not take into account the amount of throw for each of these facies as the purpose of this exercise was to simply relate fault facies observed in the field to modeled values for SGR and seal effectiveness.

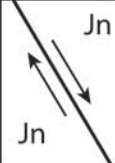

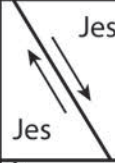

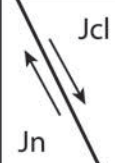



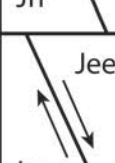

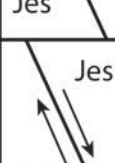





Hanging-wall Footwall	% Shale (estimated)		Fault Core Field Examples	Fault Core Facies Description	Shale Gouge Ratio (interpreted)	Relative Seal Effectiveness
	FW	HW				
	<30%	<30%		<ul style="list-style-type: none"> - Coalesced deformation bands - Sandstone lenses 	<20%	LOW
	<30%	<30%		<ul style="list-style-type: none"> - Coalesced deformation bands - Sandstone lenses - Oil stained cataclasite - Minor breccia 	<20%	LOW
	<30%	>50%		<ul style="list-style-type: none"> - Deformation bands - Fault breccia - Sandstone clasts - Cataclastic matrix 	<20%	LOW
	<30%	>50%		<ul style="list-style-type: none"> - Deformation bands - Fault breccia - Sandstone lenses - Cataclastic matrix - Sand gouge 	20% - 40%	MEDIUM
	<30%	>50%		<ul style="list-style-type: none"> - Highly fractured - Shale gouge - Fault breccia - Sandstone clasts - Sandstone lenses - Sand gouge 	20% - 40%	MEDIUM
	>50%	<30%		<ul style="list-style-type: none"> - Highly fractured - Shale gouge - Sandstone lenses - Sand gouge - Semi-laterally continuous 	20% - 40%	MEDIUM
	>50%	>50%		<ul style="list-style-type: none"> - Moderately developed shale gouge - Siltstone lenses - Highly fractured - Semi-laterally continuous 	>40%	HIGH
	>50%	>70%		<ul style="list-style-type: none"> - Well developed shale gouge - Shale membranes - Siltstone lenses - Laterally continuous 	>40%	HIGH

Figure 60. Summary of fault facies observed along the Iron Wash fault zone with interpreted shale gouge ratio and seal effectiveness (see text for discussion and description of shale gouge ratio calculations).

Fault and fracture networks, including those associated with fault damage zones, represent the locations of potential leakage and fluid migration pathways through top-seals intended to contain injected fluids within target reservoirs. Because these features are difficult to predict in the subsurface in terms of both their geometry and their hydraulic properties, it is difficult to plan for how these may impact any injection projects. Damage zones are typically below the ability of modern seismic reflection profiling images to detect. Therefore field analogs are critical to characterize hydraulic structure, fault facies, and the geometry, intensity and thickness of damage zones. The numerous small-throw faults (<5 m) contained within relay zones and adjacent to the principal slip surface have an associated damage zone and therefore is a potential leakage pathway.

Our data show that fault relays and fault lenses are another pathway for leakage of fluids across or along fault zones. Fault relay zones, specifically ones that are soft-linked and where there is no through-going fault represent a major risk when assessing seal behavior for a fault zone. Each of the individual faults on a relay system may behave as a seal, however, because there is a lateral ramp connecting the hanging wall and footwall, no fault sealing mechanisms are in place such as shale gouge. We show along with others (Peacock and Sanderson, 1994; Walsh et al., 1999; Bastesen and Rotevatn, 2012; Fachri et al., 2013) that relay zones are areas of increased faulting and fracturing, which may further enhance the lateral permeability of any sealing rocks in the relay and allow for leakage of fluids through what would otherwise be a lateral seal. Similarly, fault cores with very wide zones of fracturing, rotated fault blocks, or fault lenses are more likely to leak due to increased potential leakage pathways within and surrounding the fault zone.

Flow could however also be baffled by deformation bands specifically in porous sandstones (Rotevatn et al., 2013).

Strain Analysis

One possible interpretation of the strain analysis is that the eastern segments of the fault (Figure 6, Areas C and D) formed in the Colorado Plateau stress field and the western segments (Figure 6, Areas A and B) of the fault have formed in the transitional stress zone between the Basin & Range stress field and the Colorado Plateau stress field (Figures 55 and 58; Patton and Zandt, 1991; Flesch and Kreemer, 2010). Another possible interpretation is that the difference in strain field along strike is a result of the structural intersection of the northwest-striking Iron Wash fault with the north-northeast trending San Rafael monocline.

We believe that the fault reflects the complexities of having formed in multiple strain fields in its structure and geometry (Reches, 1978; Aydin and Reches, 1982; Krantz, 1988, 1989). Structural components of the fault zone were compiled for the trace of the fault along strike (Figure 58) and show that as the fault begins to lie within the Colorado Plateau stress field the relative increased structural complexity of the fault increases (Figure 58; Patton and Zandt, 1991; Flesch and Kreemer, 2010). Conversely, in the eastern segments of the fault there is lower relative structural complexity of the fault zone (Figure 58). Fluid-related aspects of the fault zone such as mineralization, bleaching and alteration of faults and fractures were compiled for the trace of the fault along strike (Figure 58) and show very similar relationships between the complexity of the fluid-related structures and the position relative to the stress field. Many of the structural

components of the fault zone coincide with fluid-related components, indicating that as fault complexity increases the fault is less likely to act as a seal and that this will be observed as evidence for fluids and mineralization in the fault zone (Figure 58).

Implications for CO₂ Injection

As CO₂ is injected into subsurface reservoirs as a supercritical fluid it behaves as a buoyant fluid and migrates laterally and upwards until it encounters a top seal, lateral seal or permeability change (Figure 61; White et al., 2003; Arts et al., 2008). Top-seals are a low-permeability and high capillary entry pressure cap rock above the injection target. Lateral seals can be faults and stratigraphic pinch-outs and permeability anisotropies are lateral or vertical changes in the permeability structure from sedimentary facies changes, or altered or mineralized intervals in the reservoir. These lateral seals have been modeled for the injection of CO₂ into a reservoir containing a modeled fault for both a high-permeability fault and a low-permeability fault and has been shown to produce very different results based on the characteristics of the fault (Figure 62; Chang and Bryant, 2007).

We present model results on the predicted development of fault seal membranes with standard practices to calculate shale gouge ratio and shale smear factor (Figures 50 and 51). We use these modeled fault properties to predict the permeability of the fault zone (Figure 52) and then to calculate the capillary entry pressure of the fault zone (Figure 53). These values are used to model the maximum CO₂ column height that can be supported by the fault (Figure 54). As the modeled fault throw increases towards the center of the fault and decreases up and down dip (Figure 63) the fault juxtaposes varying

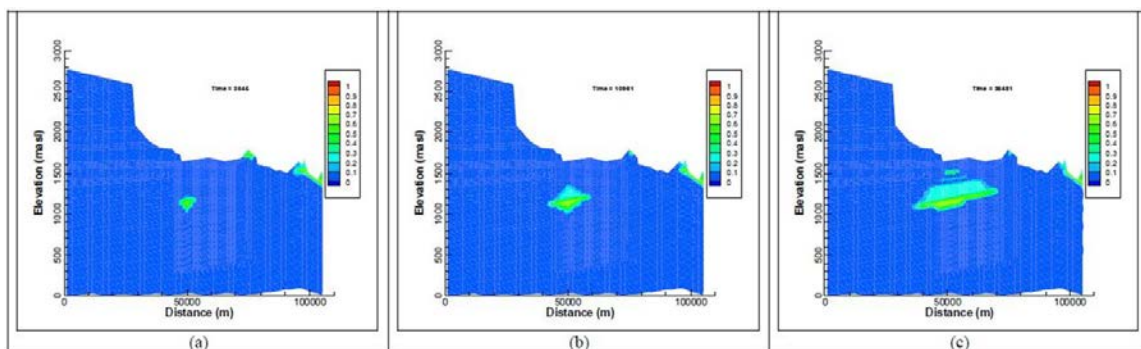


Figure 61. Modeling results showing gas saturation from injected CO₂ into the White Rim Sandstone. Model is displayed in time intervals of a) 10 years, b) 30 years, and c) 100 years (modified from White et al., 2003).

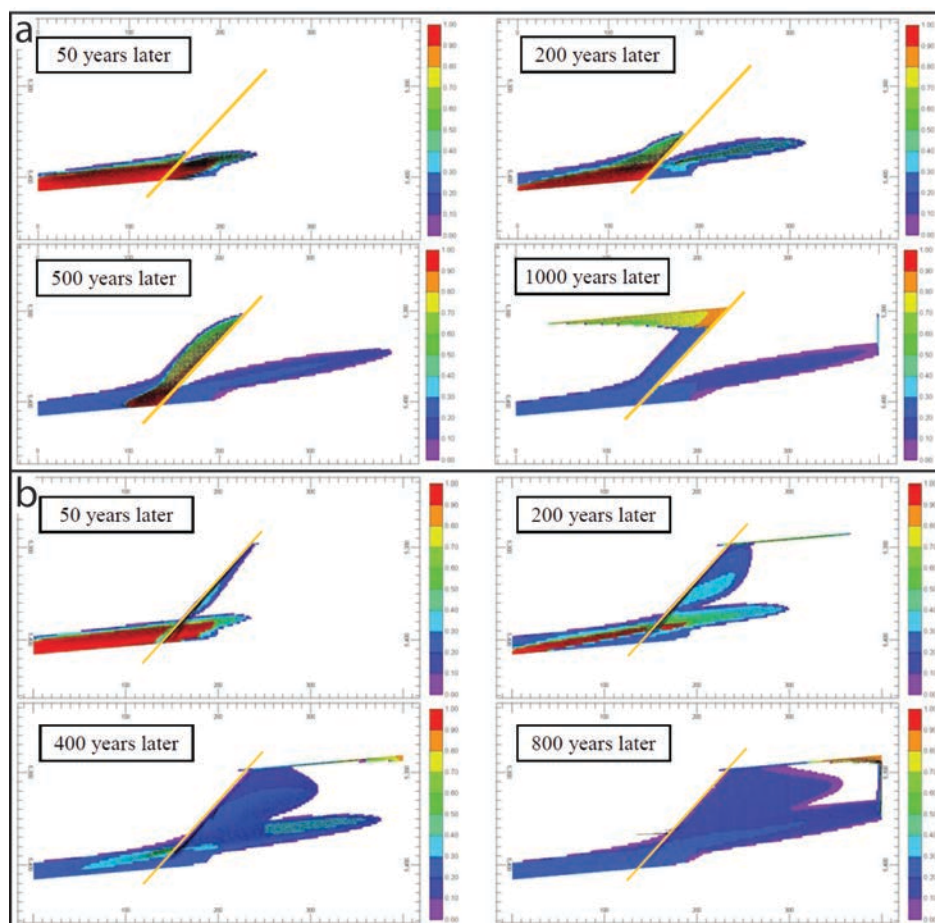


Figure 62. Modeling results showing gas saturation from injected CO₂ interacting with a fault. Fault is represented by yellow line and is modeled as a) a low-permeability fault and b) a high-permeability fault with time intervals noted for each case (modified from Chang et al., 2007).

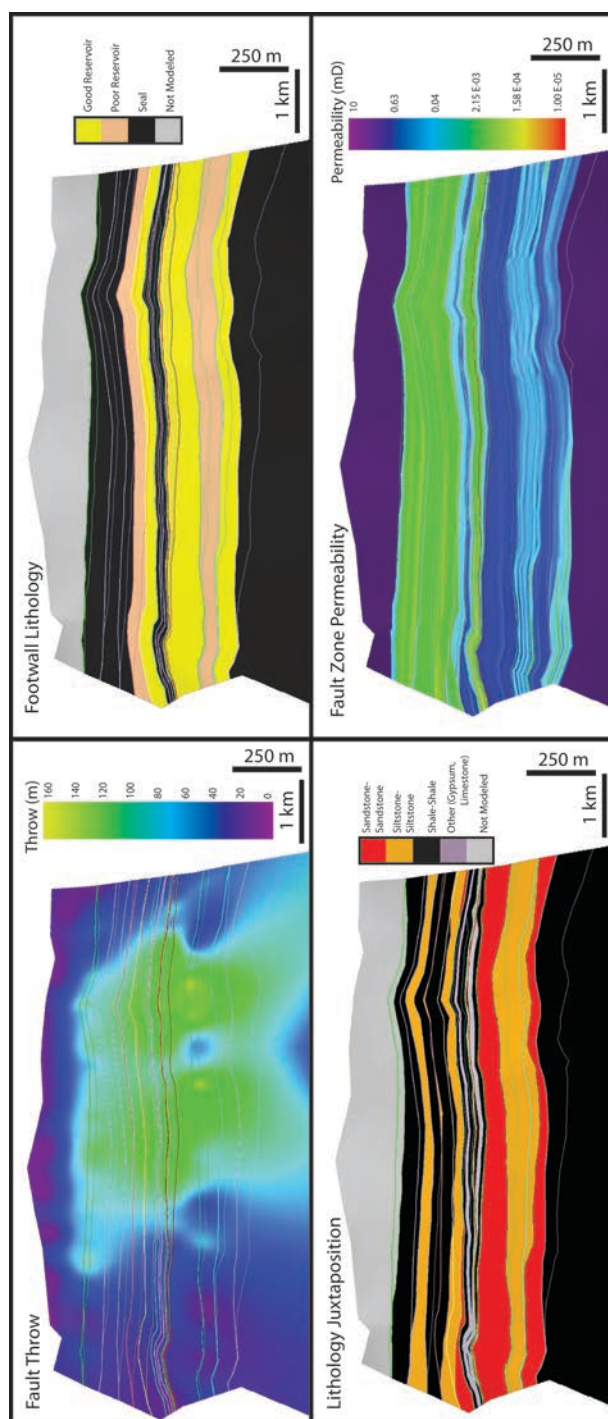


Figure 63. Perspective view of modeled fault surface of the Iron Wash fault contoured with fault zone characteristics. Surfaces are contoured with a) fault throw calculated from stratigraphic offset, b) footwall lithology calculated from V_{shale} curve (see Figure 49 and text for description), c) juxtaposition diagram of hangingwall lithologies, d) fault zone permeability calculated from shale gouge ratio (see Figure 52 and text for description). See text for description and method.

lithologies in the hanging wall and footwall (Figure 63). Modeled shale gouge ratio and shale smear factor contoured on the fault plane show that the fault has a well-developed shale membrane shallow in the fault and poorly-developed shale membrane in the sandstone dominated sections of the fault zone (Figure 64). Modeled fault zone capillary entry pressure and fault zone permeability show that the fault would likely behave as a seal in areas of the fault where there is dominantly shale in both the hanging wall and footwall or where throw is sufficient to develop gouge membranes (Figure 64). There are many parts of the fault have very low capillary entry pressure (<4 MPa) with many areas close to 0 MPa (Figure 64). The fault plane is contoured with the predicted maximum CO₂ column height that can be supported by the fault and see that where fault cuts the Navajo Formation the fault zone that would support a CO₂ column of only ~10-20 m (Figure 64), and the Slickrock Member of the Entrada Formation would support a CO₂ column height of ~25-35 m near the maximum throw on the fault (Figure 64).

There are several implications of this research for site characterization for potential injection targets for CO₂. Because small-throw faults (<100 m throw) are relatively common in most geologic settings, extensive work must be done to characterize the orientation and intensity of faults in any potential injection locality. Fault characterization is common practice in any major project involving injection of fluids into the subsurface. The National Energy Technology Laboratory (2010) best practices guide states that initial site characterization for potential localities should "identify faults and fractures". No guidelines have been put forth to define a threshold value of fault throw, distance, length, or type for which these site characterizations must occur. For example, no framework defines that all faults with throw greater than a specified value

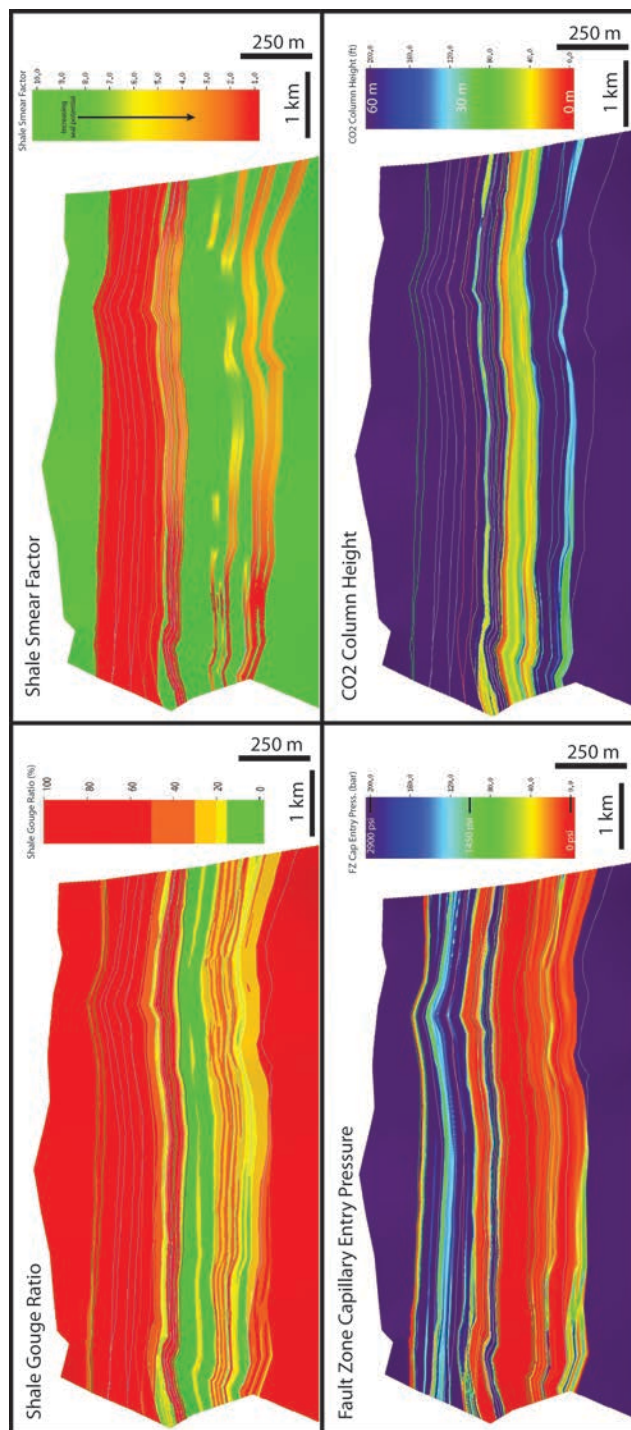


Figure 64. Perspective view of modeled fault surface of the Iron Wash fault contoured with fault zone characteristics. Surfaces are contoured with a) shale gouge ratio (see Figure 50 and text for description), b) shale smear factor (see Figure 51 and text for description), c) fault zone capillary entry pressure (see Figure 53 and text for description), d) predicted maximum CO₂ column height (see Figure 54 and text for description). See text for description and method.

must be characterized, presumably because there is not enough data on the risk of faults in CO₂ injection projects to assign such a threshold.

The National Energy Technology Laboratory (2010) also describes that a site characterization will include acquiring 2D, 3D and possibly 4D seismic data which is used along with any well or borehole data to characterize faults in the subsurface. We propose in this study that many of the features we have observed including fault-related folds, fault relay zones and fault lenses would not be resolved on 2D seismic surveys and would be difficult to resolve on terrestrial 3D seismic surveys without exceptional resolution in the data. In neither case would fracture networks, damage zones, small fault lenses (<5 m wide) and small-throw faults (<5 m) be resolved. These features represent potential leakage and migration pathways and therefore present a challenge for many potential site characterization projects.

The National Energy Technology Laboratory (2010) also describes that a site characterization will "determine the existing stress state and assess the impact of changes in pore pressure on stress". We propose that injection of fluids into the subsurface can potentially induce failure of faults that are optimally oriented to the stress field. Based on our previous assertion that there is significant difficulty in identification of all structural components in the subsurface, including faults, it would be difficult to predict failure on all possible faults in the subsurface. The uncertainty associated with fault-seal analysis in CO₂ injection projects means that further work is required in the response of faults of a wide range of throws to increased reservoir pressure and on across fault pressure difference.

Our model results that indicate based on the geometry and characteristics of the rocks of the Iron Wash fault zone, the fault does not behave as a good fault seal to fluids in the subsurface. Because the Iron Wash fault throw is small relative to the total thickness of sandstone in the Triassic to Jurassic part of the sedimentary package, our model predicts the fault to fail as a seal. We would propose that standard methodology for fault seal analysis and risking used in the petroleum industry for assigning risk to faults and populations of faults be applied to CO₂ site characterization projects. A similar approach was taken to adapt petroleum industry best practices by the National Energy Technology Laboratory (2010) for the classification of prospective storage capacity in a CO₂ site, and we propose a similar model for fault seal analysis.

CONCLUSIONS

If large-scale carbon capture and storage is implemented as a technology to address anthropogenic CO₂ emissions, there are significant challenges to overcome in the planning and characterization stages. We propose that small to medium-throw faults (>100 m throw) represent significant risk factors for proposed injection locations. We propose that faults can act as conduits for fluids for both upwards and lateral migration of fluids. Upward migrating CO₂ along a fault zone could potentially leak from the injection reservoir to the surface, or, could leak along a fault into an overlying reservoir. In both cases, CO₂ would be leaving the system that it was intended to remain in and therefore the storage project would be compromised.

Faults have been identified as one mechanism by which reservoir compartmentalization occurs (Tveranger et al., 2005; Keranen et al., 2013).

Compartmentalized reservoirs could have a significant impact on reservoir management plans for injection due to the dependence of pressure management on reservoir volume. Faults, if not properly identified and characterized could have significant impacts on reservoir pressure management because they may act as lateral seals, baffles or conduits for fluids (Braathen et al., 2009). Because faults may not be identified, migrating CO₂ plumes within a reservoir could undergo unintended pressure increases adjacent to these faults. Unintended pressure increases within reservoirs could result in the forced shutdown of injection activities, induced seismicity on faults, or even abandonment of injection sites due to lack of injectivity. Any of these results could result in the failure of CO₂ injection sites and potentially loss of large investment capital in the construction of these projects.

Induced seismicity resulting from the injection of fluids is a significant risk factor for any current or future projects (Zoback and Gorelick, 2012; Keranen et al., 2013). Earthquakes that are linked to fluid injection that are large enough magnitude to be felt by people at the surface or to cause damage to structures at the surface have been observed recently (Zoback and Gorelick, 2012; Keranen et al., 2013). Our work has shown that critically stressed faults (Barton et al., 1995; Zoback and Gorelick, 2012) that are favorably oriented in the current stress field (i.e. in the optimal orientation for failure to occur) are the most likely faults to be at risk for failure during injection activities. We have shown that in some cases, when faults are favorably oriented, that small perturbations in reservoir pressure (~2 MPa) could induce failure even on relatively strong faults with coefficients of friction of $\mu = 0.6$ and are more likely to fail assuming weak faults with $\mu = 0.4$. Unidentified or misidentified faults within potential injection

sites represent the largest risk factor for induced seismicity because either no planning has been done to prevent failure on these faults or the planning may be done under false assumptions about the nature of the faults.

We provide insight into fault-related phenomena such as deformation related to structural interaction, fault relay and linkage structures, fault related folding, and fault architecture. Results from this study have implications on the linkage and development of fault zones as discrete faults interact and link in various configurations. Additionally, fault-seal analysis depends on an understanding of the nature, geometry and architecture of faults. Understanding relationships between faults and the damage zones they create with respect to the structural location along a fault or relative to other structures will help better constrain models and predictions about these features and their occurrence in the subsurface.

Strain analysis of the Iron Wash fault zone along strike has provided support for the hypothesis that the Iron Wash fault has formed in two distinct stress regimes. The eastern segments of the fault zone have undergone pure north-northeast extension consistent with the Colorado Plateau stress field and the western segments approaching the San Rafael monocline have experienced three-dimensional strain consistent with the transition zone stress field between the Colorado Plateau and the Basin & Range stress fields (Reches, 1978; Aydin and Reches, 1982; Krantz, 1988; Patton and Zandt, 1991; Flesch and Kreemer, 2010). This change in stress field and the formation of part of the fault in a three-dimensional strain field is interpreted to be spatially related to more structurally complex areas of the fault zone and more concentrated mineralization and alteration associated with fluid migration (Figure 58). We propose that three dimensional

strain fields within potential injection sites increase the risk of faults that are favorable oriented to the stress field and therefore increase the risk of induced seismicity during injection. We would suggest that potential injection sites where possible three-dimensional strain fields are present either be abandoned or require additional characterization of faults in the area due to the elevated risk of induced seismicity.

Geometric reconstruction of the fault zone integrated with properties of the faulted rocks derived from wireline log data have been used in producing predictive models or properties of the fault. These models predict that the Iron Wash fault did not act as a seal to fluids injected on one side of the fault and that lateral migration of fluids across the fault would occur with relatively low capillary entry pressures (generally <3 MPa) where the fault produces sand-on-sand juxtaposition. The models have predicted that the fault is capable of supporting a CO₂ column height of ~10-20 m in areas of the fault where fault leakage is most likely. Geomechanical models have based on the orientations of stresses in the Colorado Plateau (Patton and Zandt, 1991; Flesch and Kreemer, 2010), stress magnitudes estimated from established relationships and mechanical properties of rocks defined by empirical relationships. These models show that as fluid pressures are increased along fault zones and fractures it is possible to reactivate these structures in either shear or tensile failure by modest increases of pore pressure.

Economics of large-scale carbon capture and storage is a final consideration in this thesis. Although our work did not focus on this subject, it would obviously be a driving force in the decision making process before moving forward with any projects. Many of the technical challenges we have identified would have implications on the

economics of storage locations, for example, leaking faults would reduce storage effectiveness and therefore would increase cost as more injection would be necessary to accomplish the same storage. Our work on induced seismicity similarly has large implications on economics as projects would likely be shut-down for long periods of time or cancelled and abandoned following any significant seismicity was detected.

Recommendations

For carbon capture and storage to be a viable mechanism for reducing global green house gas emissions, potential underground CO₂ storage sites must be characterized extensively for reservoir potential, seal integrity and possible leakage pathways. Leakage of CO₂ along faults and fracture networks in the subsurface is a major concern when characterizing the storage capacity of CO₂ storage sites and must be considered when designing injection plans. As CO₂ is injected into the subsurface, reservoir pressure increases as the plume of CO₂ migrates through the reservoir and displaces formation waters. The increasing pressure build-up from injection of fluid into deep aquifers has been attributed to the reactivation of faults within the target injection sites (Zoback and Gorelick, 2012). Earthquakes of up to magnitude 5.7 have been recently attributed to the injection of wastewater in Oklahoma (Keranen et al., 2013). Additional seismicity has been reported around the country in places like Ohio, Colorado, and New Mexico (Wessen and Nicholson, 1987; Nicholson et al., 1988; Horton, 2012; Rubenstein et al., 2013; Virgas et al., 2013) Robust data on the in-situ stresses and proper identification of faults in the subsurface prior to the injection of fluids into storage reservoirs must be a pre-requisite to any injection activity.

Detailed analysis of fault zones within potential injection sites should also include characterization of fault zone internal structure to the extent possible. We show that fault relay zones and fault lenses are potential zones of increased faulting and fracturing as well as being fault bypass systems in some cases. Since faults and fractures are the dominate seal bypass mechanisms in potential injection sites a detailed characterization of these features is crucial to the successful prediction of their sealing ability.

We propose that an ideal injection site for CO₂ sequestration would have the following characteristics:

1. Close to point sources for CO₂ emissions to reduce costs associated with transporting large volumes of CO₂
2. Devoid of any faulting or fracturing whatsoever
3. Have four-way structural closure over a large areal extent
4. Multiple, stacked reservoir seal pairs overlain by thick (as thick as possible) and laterally continuous impermeable caprock
5. Thick, high porosity/permeability reservoir intervals with excellent injectivity
6. Within a tectonically stable sedimentary basin preferably with little to no salt
7. In a region with no three-dimensional strain field
8. Low initial reservoir pressure in the injection target

Sites meeting even one of can be difficult to find; when all eight criteria are considered, it could be potentially very difficult to nearly impossible to find injection locations. However, we propose that there likely exists many injection locations that are "good enough" to act as geologic storage sites. Additional work to understand what the total potential storage volume of sites of varying degrees of quality throughout the world

will help constrain the viability of the large-scale feasibility of carbon capture and storage.

Future work relating to this project might include: 1) additional field studies to characterize fault damage zones in a wider array of settings and fault settings, 2) additional field studies to better characterize how fault geometry might be influenced by changing stress field along strike, 3) additional work on producing a wide range of models to help predict fault and fracture orientations that are likely to be reactivated as a result of injection of fluids, 4) analysis of 3-D seismic data to better understand the seismic expression of fault relays and fault lenses that can then be correlated to field observations such as in this study, 5) compiling data on active injection wells that are believed to have produced seismicity to understand how field and subsurface studies can better identify potential risks associated with injection.

REFERENCES

- Allis, R., Chidsey, T., Gwynn, W., Morgan, C., White, S., Adams, M., and Moore, J., 2001, Natural CO₂ reservoirs on the Colorado Plateau and southern Rocky Mountains: Candidates for CO₂ sequestration, *in* Proceedings of the First National Conference on Carbon Sequestration, p. 14–17.
- Allis, R.G., Chidsey, T.C., Morgan, C., Moore, J., and White, S.P., 2003, CO₂ sequestration potential beneath large power plants in the Colorado Plateau-Southern Rocky Mountain region, USA., *in* Proceedings, 2nd Annual Conferences on Carbon Sequestration, Alexandria, Virginia, May, p. 5–8.
- Allmendinger, R.W., Hauge, T.A., Hauser, E.C., Potter, C.J., Klemperer, S.L., Nelson, K.D., Knuepfer, P., and Oliver, J., 1987, Overview of the COCORP 40°N Transect, western United States: The fabric of an orogenic belt: Geological Society of America Bulletin, v. 98, p. 308, doi: 10.1130/0016-7606(1987)98<308:OOTCNT>2.0.CO;2.
- Anderson, E.M., 1951, The dynamics of faulting, Edinburgh, Oliver and Boyd, 206 p.

- Antonellini, M., Aydin, A., 1994, Effects of faulting on fluid flow in porous sandstones: petrophysical properties: *AAPG Bulletin*, v. 78, p. 355-377.
- Arts, R., Chadwick, A., Eiken, O., Thibeau, S., and Nooner, S., 2008, Ten years' experience of monitoring CO₂ injection in the Utsira Sand at Sleipner, offshore Norway: *First Break*, v. 26, p. 29-36.
- Aydin, A., 2000, Fractures, faults, and hydrocarbon entrapment, migration and flow: *Marine and Petroleum Geology*, v. 17, p. 797-814.
- Aydin, A., and Johnson, A.M., 1983, Analysis of faulting in porous sandstones: *Journal of Structural Geology*, v. 5, p. 19-31.
- Aydin, A., and Reches, Z., 1982, Number and orientation of fault sets in the field and in experiments: *Geology*, v. 10, p. 107-112.
- Baars, D.L., 1989, Shelf carbonates of the Paradox Basin San Juan River field trip: *American Geophysical Union Field Trip Guidbook*, v. T124.
- Barton, D.C., 2011, Determining CO₂ Storage Potential: Characterization of Seal Integrity and Reservoir Failure in Exposed Analogs: M.S. Thesis, Department of Geology, Utah State University.
- Barton, C.A., Zoback, M.D., and Moos, D., 1995, Fluid flow along potentially active faults in crystalline rock: *Geology*, v. 23, p. 683-686.
- Bastesen, E., and Rotevatn, A., 2012, Evolution and structural style of relay zones in layered limestone-shale sequences: insights from the Hammam Faraun Fault Block, Suez rift, Egypt: *Journal of the Geological Society*, v. 169, p. 477-488, doi: 10.1144/0016-76492011-100.
- Berg, S.S., and Skar, T., 2005, Controls on damage zone asymmetry of a normal fault zone: outcrop analyses of a segment of the Moab fault, SE Utah: *Journal of Structural Geology*, v. 27, p. 1803-1822, doi: 10.1016/j.jsg.2005.04.012.
- Berglund, H.T., Sheehan, A.F., Murray, M.H., Roy, M., Lowry, A.R., Nerem, R.S., and Blume, F., 2012, Distributed deformation across the Rio Grande Rift, Great Plains, and Colorado Plateau: *Geology*, v. 40, p. 23-26.
- Bird, P., 1984, Laramide crustal thickening event in the Rocky Mountain foreland and Great Plains: *Tectonics*, v. 3, p. 741-758.
- Bird, P., 1998, Kinematic history of the Laramide orogeny in latitudes 35°-49°N, western United States: *Tectonics*, v. 17, p. 780-801, doi: 10.1029/98TC02698.

- Bird, P., 2002, Stress direction history of the western United States and Mexico since 85 Ma: *Tectonics*, v. 21, no. 3, p. 1014, doi: 10.1029/2001TC001319.
- Braathen, A., Tveranger, J., Fossen, H., Skar, T., Cardozo, N., Semshaug, S.E., Bastesen, E., and Sverdrup, E., 2009, Fault facies and its application to sandstone reservoirs: *AAPG Bulletin*, v. 93, p. 891–917, doi: 10.1306/03230908116.
- Bretan, P., Yielding, G., and Jones, H., 2003, Using calibrated shale gouge ratio to estimate hydrocarbon column heights: *AAPG Bulletin*, v. 87, p. 397–413, doi: 10.1306/08010201128.
- Bretan, P., Yielding, G., Mathiassen, O.M., and Thorsnes, T., 2011, Fault-seal analysis for CO₂ storage: an example from the Troll area, Norwegian Continental Shelf: *Petroleum Geoscience*, v. 17, p. 181–192, doi: 10.1144/1354-079310-025.
- Bump, A.P., and Davis, G.H., 2003, Late Cretaceous–early Tertiary Laramide deformation of the northern Colorado Plateau, Utah and Colorado: *Journal of Structural Geology*, v. 25, p. 421–440.
- Caine, J.S., Bruhn, R.L., and Forster, C.B., 2010, Internal structure, fault rocks, and inferences regarding deformation, fluid flow, and mineralization in the seismogenic Stillwater normal fault, Dixie Valley, Nevada: *Journal of Structural Geology*, v. 32, p. 1576–1589, doi: 10.1016/j.jsg.2010.03.004.
- Caine, J.S., Evans, J.P., and Forster, C.B., 1996, Fault zone architecture and permeability structure: *Geology*, v. 24, p. 1025–1028.
- Chan, M.A., Parry, W.T., and Bowman, J.R., 2000, Diagenetic hematite and manganese oxides and fault-related fluid flow in Jurassic sandstones, southeastern Utah: *AAPG bulletin*, v. 84, p. 1281–1310.
- Chan, M.A., Parry, W.T., Petersen, E.U., and Hall, C.M., 2001, ⁴⁰Ar/³⁹Ar age and chemistry of manganese mineralization in the Moab and Lisbon fault systems, southeastern Utah: *Geology*, v. 29, p. 331–334.
- Chang, K.W., and Bryant, S.L., 2007, Dynamics of CO₂ plumes encountering a fault in a reservoir: 6th Annual Conference on Carbon Capture and Sequestration, DOE/NETL, Pittsburgh, PA.
- Chester, F.M., and Logan, J.M., 1986, Implications for mechanical properties of brittle faults from observations of the Punchbowl fault zone, California: *Pure and Applied Geophysics*, v. 124, p. 79–106.
- Childs, C., Manzocchi, T., Walsh, J.J., Bonson, C.G., Nicol, A., and Schöpfer, M.P.J., 2009, A geometric model of fault zone and fault rock thickness variations: *Journal of Structural Geology*, v. 31, p. 117–127, doi: 10.1016/j.jsg.2008.08.009.

- Childs, C., Sylta, O., Moriya, S., Walsh, J. J. and Manzocchi, T., 2002, A method for including the capillary properties of faults in hydrocarbon migration models, in A. G. Koestler and R. Hunsdale, editors, Hydrocarbon seal quantification: Amsterdam, Elsevier, Norwegian Petroleum Society (NPF) Special Publication 11, p. 127–139.
- Carbon Mitigation Initiative, 2013, Princeton University Carbon Mitigation Initiative: www.cmi.princeton.edu (accessed May 2013).
- Currie, B.S., 1997, Sequence stratigraphy of nonmarine Jurassic–Cretaceous rocks, central Cordilleran foreland-basin system: Geological Society of America Bulletin, v. 109, p. 1206–1222, doi: 10.1130/0016-7606(1997)109<1206:SSONJC>2.3.CO;2.
- Davatzes, N.C., 2003, Fault architecture as a function of deformation mechanism in clastic rocks with an emphasis on sandstone: Ph.D. Dissertation, Stanford University Department of Geological and Environmental Science, 185 p.
- Davatzes, N.C., Aydin, A., and Eichhubl, P., 2003, Overprinting faulting mechanisms during the development of multiple fault sets in sandstone, Chimney Rock fault array, Utah, USA: Tectonophysics, v. 363, p. 1–18, doi: 10.1016/S0040-1951(02)00647-9.
- Davatzes, N.C., Eichhubl, P., and Aydin, A., 2005, Structural evolution of fault zones in sandstone by multiple deformation mechanisms: Moab fault, southeast Utah: Geological Society of America Bulletin, v. 117, p. 135, doi: 10.1130/B25473.1.
- DeCelles, P.G., 2004, Late Jurassic to Eocene evolution of the Cordilleran thrust belt and foreland basin system, western USA: American Journal of Science, v. 304, p. 105–168.
- Dickinson, W.R., 2004, Evolution of the North American Cordillera: Annual Review of Earth and Planetary Sciences, v. 32, p. 13–45, doi: 10.1146/annurev.earth.32.101802.120257.
- Dickinson, W.R., Klute, M.A., Hayes, M.J., Janecke, S.U., Lundin, E.R., McKittrick, M.A., and Olivares, M.D., 1988, Paleogeographic and paleotectonic setting of Laramide sedimentary basins in the central Rocky Mountain region: Geological Society of America Bulletin, v. 100, p. 1023–1039, doi: 10.1130/0016-7606(1988)100<1023:PAPSOL>2.3.CO;2.
- Dockrill, B., and Shipton, Z.K., 2010, Structural controls on leakage from a natural CO₂ geologic storage site: Central Utah, U.S.A.: Journal of Structural Geology, v. 32, p. 1768–1782, doi: 10.1016/j.jsg.2010.01.007.

- Doelling, H.H., 1988, Geology of Salt Valley Anticline and Arches National Park, Grand County, Utah, in, Doelling, H.H., Oviatt, C.G., Huntoon, P.W. (editors), Salt Deformation in the Paradox Region Bulletin, 122. Utah Geological and Mineral Survey, Salt Lake City, UT, p. 1–58.
- Doelling, H.H., 2002, Interim geologic map of the San Rafael Desert 30' x 60' quadrangle, Emery and Grand Counties, Utah: Utah Geological Survey Open-file report 404, scale 1:100,000.
- Doelling, H.H., Kuehne, P.A., Willis, G.C., Ehler, J.B., in review, Geologic map of the San Rafael Desert 30' x 60' quadrangle, Emery and Grand Counties, Utah: Utah Geological Survey, scale 1:100,000.
- Evans, J.P., 1990, Thickness-displacement relationships for fault zones: *Journal of Structural Geology*, v. 12, p. 1061–1065.
- Evans, J.P., Forster, C.B., and Goddard, J.V., 1997, Permeability of fault-related rocks, and implications for hydraulic structure of fault zones: *Journal of Structural Geology*, v. 19, p. 1393–1404.
- Evans, J.P., Heath, J., Shipton, Z.K., Kolesar, P.T., Dockrill, B., Williams, A., Kirchner, D., Lachmar, T.E., and Nelson, S.T., 2004, Natural leaking CO₂-charged systems as analogs for geologic sequestration sites, *in* Third Annual Conference on Carbon Capture and Sequestration, Alexandria, VA.
- Fachri, M., Tveranger, J., Braathen, A., and Schueller, S., 2013, Sensitivity of fluid flow to deformation-band damage zone heterogeneities: A study using fault facies and truncated Gaussian simulation: *Journal of Structural Geology*, v. 52, p. 60–79, doi: 10.1016/j.jsg.2013.04.005.
- Faulkner, D.R., Jackson, C.A.L., Lunn, R.J., Schlische, R.W., Shipton, Z.K., Wibberley, C.A.J., and Withjack, M.O., 2010, A review of recent developments concerning the structure, mechanics and fluid flow properties of fault zones: *Journal of Structural Geology*, v. 32, p. 1557–1575, doi: 10.1016/j.jsg.2010.06.009.
- Faulkner, D.R., Mitchell, T.M., Jensen, E., and Cembrano, J., 2011, Scaling of fault damage zones with displacement and the implications for fault growth processes: *Journal of Geophysical Research*, v. 116, doi: 10.1029/2010JB007788.
- Fisher, Q.J., Harris, S.D., McAllister, E., Knipe, R.J., and Bolton, A.J., 2001, Hydrocarbon flow across faults by capillary leakage revisited: *Marine and Petroleum Geology*, v. 18, p. 251–257.
- Flesch, L.M., and Kreemer, C., 2010, Gravitational potential energy and regional stress and strain rate fields for continental plateaus: Examples from the central Andes

- and Colorado Plateau: Tectonophysics, v. 482, p. 182–192, doi: 10.1016/j.tecto.2009.07.014.
- Fossen, H., and Hesthammer, J., 1997, Geometric analysis and scaling relations of deformation bands in porous sandstone: *Journal of Structural Geology*, v. 19, p. 1479–1493.
- Fossen, H., Schultz, R.A., Shipton, Z.K., and Mair, K., 2007, Deformation bands in sandstone: a review: *Journal of the Geological Society*, v. 164, p. 1–15.
- Foxford, K. A., Garden, I. R., Guscott, S. C., Burley, S. D., Lewis, J. J. M., Walsh, J. J., and Watterson, J., 1996, The field geology of the Moab fault, in A. C. Huffman, Jr., W. R. Lund, and L. H. Godwin, editors., *Geology and resources of the Paradox basin: Utah Geological Association Guidebook 25*, p. 265–283.
- Fredman, N., Tveranger, J., Semshaug, S.E., Braathen, A., and Sverdrup, E., 2007, Sensitivity of fluid flow to fault core architecture and petrophysical properties of fault rocks in siliciclastic reservoirs: a synthetic fault model study: *Petroleum Geoscience*, v. 13, p. 305–320.
- Friedman, J.D., Case, J.E., and Simpson, S.L., 1994, Tectonic trends of the northern part of the Paradox Basin, southeastern Utah and southwestern Colorado, as derived from Landsat multispectral scanner imaging and geophysical and geologic mapping.: *U.S. Geological Survey Bulletin 2000-C*, 33 p.
- Ganerød, G.V., Braathen, A., and Willemoes-Wissing, B., 2008, Predictive permeability model of extensional faults in crystalline and metamorphic rocks; verification by pre-grouting in two sub-sea tunnels, Norway: *Journal of Structural Geology*, v. 30, p. 993–1004, doi: 10.1016/j.jsg.2008.04.001.
- Gudmundsson, A., 2001, Fluid overpressure and flow in fault zones: field measurements and models: *Tectonophysics*, v. 336, p. 183–197.
- Gudmundsson, A., Berg, S.S., Lyslo, K.B., and Skurtveit, E., 2001, Fracture networks and fluid transport in active fault zones: *Journal of Structural Geology*, v. 23, p. 343–353.
- Ha-Duong, M., and Keith, D.W., 2003, Carbon storage: the economic efficiency of storing CO₂ in leaky reservoirs: *Clean Technologies and Environmental Policy*, v. 5, p. 181–189, doi: 10.1007/s10098-003-0213-z.
- Hammond, K.J., and Evans, J.P., 2003, Geochemistry, mineralization, structure, and permeability of a normal fault zone, Casino mine, Alligator Ridge district, north central Nevada: *Journal of Structural Geology*, v. 25, p. 717–736.

- Hawley, C.C., Robeck, R.C., and Dyer, H.B., 1968, Geology, altered rocks and ore deposits of the San Rafael Swell, Emery County, Utah: Geological Survey Bulletin 1239.
- Hesthammer, J., and Fossen, H., 2000, Uncertainties associated with fault sealing analysis: *Petroleum Geoscience*, v. 6, p. 37–45.
- Hestir, K., Martel, S.J., Yang, J., Evans, J.P., Long, J.C.S., D’Onfro, P., and Rizer, W.D., 2001, Use of conditional simulation, mechanical theory, and fault observations to characterize the structure of faults and fracture networks: *Geophysical Monograph Series*, v. 42, p. 61–73.
- Heylman, E.B., 1964, Shallow oil and gas possibilities in east and south-central Utah: *Utah Geological and Mineralogical Survey Special Studies*, v. 8.
- Hickman, S., Sibson, R.H., and Bruhn, R.L., 1995, Introduction to special section: Mechanical involvement of fluids in faulting: *Journal of Geophysical Research*, v. 100, p. 12,831–12,840.
- Hintze, L.F. and Kowallis, B.J., 2009, *Geologic History of Utah: Brigham Young University Geology Studies Special Publication 9*, 225 p.
- Hintze, L.F., 1993, *Geologic history of Utah: Brigham Young University Geology Studies Special Publication 7*, 202 p.
- Hintze, L.F., Willis, G.C., Laes, D.Y.M., Sprinkel, D.A., and Brown, K.D., 2000, *Digital Geologic Map of Utah: Utah Geological Survey Digital State Map*, scale 1:500000.
- Holloway, S., 2001, Storage of fossil fuel-derived carbon dioxide beneath the surface of the earth: *Annual reviews of energy and the environment*, v. 26, p. 145–166.
- Horton, S., 2012, Disposal of hydrofracking waste water fluid by injection into subsurface aquifers triggers earthquake swarm in Central Arkansas with potential for damaging earthquake: *Seismological Research Letters* 83, p. 250–260.
- Hull, J., 1988, Thickness-displacement relationships for deformation zones: *Journal of Structural Geology*, v. 10, p. 431–435.
- Huntoon, J. E., Hansley, P. L., and Naeser, N. D., 1999, The search for a source rock for the giant tar sand triangle accumulation, southeastern Utah: *AAPG Bulletin*, v. 83, p. 467–495.
- Huntoon, P.W., and Sears, J.W., 1975, Bright angel and eminence faults, eastern Grand Canyon, Arizona: *Geological Society of America Bulletin*, v. 86, p. 465–472.

- International Energy Agency, 2012, International Energy Agency Statistics: 2012 Edition: CO₂ Emissions from Fuel Combustion, 138 p.
- Intergovernmental Panel on Climate Change, 1990, Climate Change: The IPCC Scientific Assessment: Houghton, J.T., Jenkins G.J., and Ephraums, J.J. (editors), Cambridge University Press, Cambridge United Kingdom and New York, NY, USA, 414 p.
- Intergovernmental Panel on Climate Change, 1992, Climate Change 1992: The Supplementary Report to the IPCC Scientific Assessment: Houghton, J.T., Callander, B.A. and Varney, S.K. (editors), Cambridge University Press, Cambridge United Kingdom and New York, NY, USA, 106 p.
- Intergovernmental Panel on Climate Change, 2001, Climate Change 2001: The Scientific Basis: Contribution of Working Group I to the Third Assessment Report of the Intergovernmental Panel on Climate Change: Houghton, J.T., Ding, Y., Griggs, D.J., Noguer, M., van der Linden, P.J., Dal, X., Maskell, K., Johnson, C.A., (editors): Cambridge University Press, Cambridge, United Kingdom and New York, NY, USA, 94 p.
- Intergovernmental Panel on Climate Change, 2005, International Panel on Climate Change Special Report on Carbon Dioxide Capture and Storage. Prepared by Working Group III of the Intergovernmental Panel on Climate Change, Metz, B., O., Davidson, H. C. de Coninck, M. Loos, and L. A. Meyer (editors): Cambridge University Press, Cambridge, United Kingdom and New York, NY, USA, 442 p.
- Janecke, S.U., Vandenburg, C.J., and Blankenau, J.J., 1998, Geometry, mechanisms and significance of extensional folds from examples in the Rocky Mountain Basin and Range province, U.S.A.: *Journal of Structural Geology*, v. 20, p. 841–856, doi: 10.1016/S0191-8141(98)00016-9.
- Jennings, J.B., 1987, Capillary Pressure Techniques: Application to Exploration and Development Geology: *AAPG Bulletin*, v. 71, p. 1196–1209.
- Jones, C.H., Farmer, G.L., Sageman, B., and Zhong, S., 2011, Hydrodynamic mechanism for the Laramide orogeny: *Geosphere*, v. 7, p. 183–201.
- Jones, C.H., Sonder, L.J., and Unruh, J.R., 1998, Lithospheric gravitational potential energy and past orogenesis: Implications for conditions of initial Basin and Range and Laramide deformation: *Geology*, v. 26, p. 639–642.
- Kelly, V.C., 1955, Tectonics of the Four Corners region, *in* Four Corners Geological Society Guidebook, First Field Conference, p. 108-117.

- Keranen, K.M., Savage, H.M., Abers, G.A., and Cochran, E.S., 2013, Potentially induced earthquakes in Oklahoma, USA: Links between wastewater injection and the 2011 Mw 5.7 earthquake sequence: *Geology*, v. 41, p. 699–702.
- Kim, Y.-S., and Sanderson, D.J., 2005, The relationship between displacement and length of faults: a review: *Earth-Science Reviews*, v. 68, p. 317–334, doi: 10.1016/j.earscirev.2004.06.003.
- Kim, Y.-S., Peacock, D.C., and Sanderson, D.J., 2004, Fault damage zones: *Journal of Structural Geology*, v. 26, p. 503–517, doi: 10.1016/j.jsg.2003.08.002.
- Kocurek, G., 2003, Limits on extreme eolian systems: Sahara of Mauritania and Jurassic Navajo Sandstone examples, in Chan, M. A., and Archer, A. W., editors., *Extreme depositional environments: Mega end members in geologic time: Geological Society of America Special Paper 370: Boulder, CO, Geological Society of America*, p. 44-53.
- Kocurek, G.A., and Dott, R.H., 1983, Jurassic paleogeography and paleoclimate of the central and southern Rocky Mountains region, in Reynolds, M.W., and Dolly, E.D., editors., *Mesozoic paleogeography of west-central United States: Society of Economic Paleontologists and Mineralogists (Rocky Mountain Section)*, p. 101-113.
- Krantz, R.W., 1988, Multiple fault sets and three-dimensional strain: theory and application: *Journal of Structural Geology*, v. 10, p. 225–237.
- Krantz, R.W., 1989, Orthorhombic fault patterns: the odd axis model and slip vector orientations: *Tectonics*, v. 8, p. 483–495.
- Ligtenberg, J.H., 2005, Detection of fluid migration pathways in seismic data: implications for fault seal analysis: *Basin Research*, v. 17, p. 141–153, doi: 10.1111/j.1365-2117.2005.00258.x.
- Lindsay, N. G., Murphy, F. C., Walsh, J. J. and Watterson, J., 1993, Outcrop studies of shale smear on fault surfaces: *International Association of Sedimentologists Special Publication 15*, p. 113–123.
- Maerten, L., Pollard, D.D., and Maerten, F., 2001, Digital mapping of three-dimensional structures of the Chimney Rock fault system, central Utah: *Journal of Structural Geology*, v. 23, p. 585–592.
- Manzocchi, T., Childs, C., and Walsh, J.J., 2010, Faults and fault properties in hydrocarbon flow models: *Geofluids*, doi: 10.1111/j.1468-8123.2010.00283.x.
- Manzocchi, T., Walsh, J.J., Nell, P., and Yielding, G., 1999, Fault transmissibility multiplies for flow simulation models: *Petroleum Geoscience*, v. 5, p. 53–63.

- McGrath, A.G., and Davison, I., 1995, Damage zone geometry around fault tips: *Journal of Structural Geology*, v. 17, p. 1011–1024.
- McPherson, B. J. and R. Grigg, 2010, Gordon Creek Site Proposal: Southwest Regional Partnership on Carbon Sequestration Project Management Plan.
- Micarelli, L., Moretti, I., and Daniel, J.M., 2003, Structural properties of rift-related normal faults: the case study of the Gulf of Corinth, Greece: *Journal of Geodynamics*, v. 36, p. 275–303, doi: 10.1016/S0264-3707(03)00051-6.
- Moretti, I., 1998, The role of faults in hydrocarbon migration: *Petroleum Geosciences*, v. 4, p. 81-94.
- Nelson, R. A., 1985, in *Geological analysis of naturally fractured reservoirs*. Houston, TX: Gulf Publishing 320 p.
- National Energy Technology Laboratory, 2010, Site screening, selection, and initial characterization for storage of CO₂ in deep geologic formations: United States Department of Energy National Energy Technology Laboratory, 118 p.
- National Energy Technology Laboratory, 2012, United States Department of Energy National Energy Technology Laboratory Carbon storage program research and development needs workshop report, 2012. Leonardo Technologies, Inc, (editors), 70 p.
- Nicholson, C., Roeloffs, E., and Wesson, R. L., 1988, The northeastern Ohio earthquake of 31 January 1986: Was it induced?: *Bulletin of the Seismological Society of America*, v. 78, 188-217.
- Nuccio, V.F., and Condon, S.M., 1996, Burial and thermal history of the Paradox Basin, Utah and Colorado, and petroleum potential of the Middle Pennsylvanian Paradox Formation: *U.S. Geological Survey Bulletin 2000-C*, 47 p.
- Ogilvie, S.R., and Glover, P.W.J., 2001, The petrophysical properties of deformation bands in relation to their microstructure: *Earth and Planetary Science Letters*, v. 193, p. 129–142.
- Ostenna, D., 2012, Blue Castle Licensing Project UQFPWG Update, *in Proceedings, Utah Quaternary Fault Parameters Working Group, 8th*, Salt Lake City, Utah, Utah Geological Survey.
- Oviatt, C.G., 1988, Evidence for quaternary deformation in the Salt Valley Anticline, southeastern Utah, in, Doelling, H.H., Oviatt, C.G., Huntoon, P.W. (editors), *Salt Deformation in the Paradox Region Bulletin*, 122. Utah Geological and Mineral Survey, Salt Lake City, UT, p. 61–76.

- Patton, H.J. and Zandt, G., 1991, Seismic moment tensors of western United States earthquakes and implications for the tectonic stress-field: *Journal of Geophysical Research*, v. 96, p. 245-259.
- Peacock, D.C.P., 2002, Propagation, interaction and linkage in normal fault systems: *Earth-Science Reviews*, v. 58, p. 121–142.
- Peacock, D.C.P., Knipe, R.J., and Sanderson, D.J., 2000, Glossary of normal faults: *Journal of Structural Geology*, v. 22, p. 291–305.
- Peacock, D.C.P., and Sanderson, D.J., 1991, Displacements, segment linkage and relay ramps in normal fault zones: *Journal of Structural Geology*, v. 13, p. 721–733.
- Petrie, E.S. and Evans, J.P., in review, Failure of caprock seals as determined from mechanical stratigraphy, stress history and tensile failure analysis of exhumed analogs: *American Association of Petroleum Geologists Bulletin*.
- Pevear, D. R., Vrolijk, P. J., and Longstaffe, F. J., 1997, Timing of Moab fault displacement and fluid movement integrated with burial history using radiogenic and stable isotopes, in J. Hendry, P. Carey, J. Parnell, A. Ruffell, and R. Worden, eds., *Migration and interaction in sedimentary basins and orogenic belts: Second International Conference on Fluid Evolution*, Belfast, Northern Ireland, p. 42–45.
- Philipp, S.L., 2012, Fluid overpressure estimates from the aspect ratios of mineral veins: *Tectonophysics*, v. 581, p. 35–47, doi: 10.1016/j.tecto.2012.01.015.
- Pipiringos, G.N., and O'Sullivan, R.B., 1978, Principal unconformities in Triassic and Jurassic rocks, Western Interior United States--A preliminary survey: U.S. Geological Survey Professional Paper 1035-A, p. 29.
- Poole, F.G., and Sandberg, C.A., 1991, Mississippian paleogeography and conodont biostratigraphy of the Western United States, in Cooper, J.D., and Stevens, C.H., editors., *Paleozoic Paleogeography of the Western United States—II: Pacific Section*, Society of Economic Paleontologists and Mineralogists Book 67, v. 1, p. 107-136.
- Poole, F.G., Stewart, J.H., Palmer, A.R., Sandberg, C.A., Madrid, R.J., Ross, R.J., Jr., Hintze, L.F., Miller, M.M., and Wrucke, C.T., 1992, Latest Precambrian to latest Devonian time; development of a continental margin, in Burchfiel, B.C., Lipman, P.W., and Zoback, M.L., editors., *The Cordilleran Orogen, Conterminous U.S.:* Geological Society of America, *The Geology of North America*, v. G-3, p. 9-56.
- Rawling, G.C., Goodwin, L.B., and Wilson, J.L., 2001, Internal architecture, permeability structure, and hydrologic significance of contrasting fault-zone types: *Geology*, v. 29, p. 43, doi: 10.1130/0091-7613(2001)029<0043:IAPSAH>2.0.CO;2.

- Reches, Z., 1978, Analysis of faulting in three-dimensional strain field: *Tectonophysics*, v. 47, p. 109–129.
- Roberts, G.P., 1996, Variation in fault-slip directions along active and segmented normal fault systems: *Journal of Structural Geology*, v. 18, p. 835–845.
- Robertson, E.C., 1983, Relationship of fault displacement to gouge and breccia thickness: *Society of Mining Engineers, American Institute of Mining Engineers Transactions*, v. 274, p. 1426-1432.
- Rotevatn, A., Sandve, T.H., Keilegavlen, E., Kolyukhin, D., and Fossen, H., 2013, Deformation bands and their impact on fluid flow in sandstone reservoirs: the role of natural thickness variations: *Geofluids*, doi: 10.1111/gfl.12030.
- Rotevatn, A., Torabi, A., Fossen, H., and Braathen, A., 2008, Slipped deformation bands: A new type of cataclastic deformation bands in Western Sinai, Suez rift, Egypt: *Journal of Structural Geology*, v. 30, p. 1317–1331, doi: 10.1016/j.jsg.2008.06.010.
- Roy, M., Jordan, T.H., and Pederson, J., 2009, Colorado Plateau magmatism and uplift by warming of heterogeneous lithosphere: *Nature*, v. 459, p. 978–982, doi: 10.1038/nature08052.
- Rubenstein., J. L., Ellsworth, W. L., and McGarr, A., 2013, The 2001 – present triggered seismicity sequence in the Raton Basin of Southern Colorado/Northern New Mexico, *Seismological Research Letters*, v. 84, p. 374.
- Saleeby, J., 2003, Segmentation of the Laramide slab—Evidence from the southern Sierra Nevada region: *Geological Society of America Bulletin*, v. 115, p. 655–668.
- Sammis, C.G., and Ben-Zion, Y., 2008, Mechanics of grain-size reduction in fault zones: *Journal of Geophysical Research*, v. 113, doi: 10.1029/2006JB004892.
- Savage, H.M., and Brodsky, E.E., 2011, Collateral damage: Evolution with displacement of fracture distribution and secondary fault strands in fault damage zones: *Journal of Geophysical Research*, v. 116, doi: 10.1029/2010JB007665.
- Schlische, R.W., 1995, Geometry and origin of fault-related folds in extensional settings: *Aapg Bulletin-American Association of Petroleum Geologists*, v. 79, p. 1661–1678.
- Scholz, C.H., 1987, Wear and gouge formation in brittle faulting: *Geology*, v. 15, p. 493, doi: 10.1130/0091-7613(1987)15<493:WAGFIB>2.0.CO;2.

- Schueller, S., Braathen, A., Fossen, H., and Tveranger, J., 2013, Spatial distribution of deformation bands in damage zones of extensional faults in porous sandstones: Statistical analysis of field data: *Journal of Structural Geology*, doi: 10.1016/j.jsg.2013.03.013.
- Schultz, R.A., and Fossen, H., 2008, Terminology for structural discontinuities: *AAPG Bulletin*, v. 92, p. 853–867, doi: 10.1306/02200807065.
- Shipton, Z.K., and Cowie, P.A., 2001, Damage zone and slip-surface evolution over μm to km scales in high-porosity Navajo sandstone, Utah: *Journal of Structural Geology*, v. 23, p. 1825–1844.
- Shipton, Z.K., and Cowie, P.A., 2003, Erratum to: A conceptual model for the origin of fault damage zone structures in high-porosity sandstone: *Journal of Structural Geology*, v. 25, p. 1343–1345, doi: 10.1016/S0191-8141(03)00060-9.
- Shipton, Z.K., Evans, J.P., Kirschner, D., Kolesar, P.T., Williams, A.P., and Heath, J., 2004, Analysis of CO₂ leakage through “low-permeability” faults from natural reservoirs in the Colorado Plateau, east-central Utah: Geological Society, London, Special Publications, v. 233, p. 43–58.
- Shipton, Z.K., Evans, J.P., Robeson, K.R., Forster, C.B., and Snelgrove, S., 2002, Structural heterogeneity and permeability in faulted eolian sandstone: Implications for subsurface modeling of faults: *AAPG bulletin*, v. 86, p. 863–883.
- Shipton, Z.K., Soden, A.M., Kirkpatrick, J.D., Bright, A.M., and Lunn, R.J., 2006, How thick is a fault? Fault displacement-thickness scaling revisited: *Geophysical Monograph Series*, v. 170, p. 193–198.
- Sibson, R.H., 1977, Fault rocks and fault mechanisms: *Journal of the Geological Society*, v. 133, p. 191–213.
- Sibson, R.H., 1996, Structural permeability of fluid-driven fault-fracture meshes: *Journal of Structural Geology*, v. 18, p. 1031–1042.
- Skerlec, G.M., 1996, Risking fault seal in the Gulf Coast (abs.): *AAPG Annual Convention Program and Abstracts*, v. 5, p. A131.
- Solum, J.G., van der Pluijm, B.A., and Peacor, D.R., 2005, Neocrystallization, fabrics and age of clay minerals from an exposure of the Moab Fault, Utah: *Journal of Structural Geology*, v. 27, p. 1563–1576, doi: 10.1016/j.jsg.2005.05.002.
- Sonder, L.J., and Jones, C.H., 1999, Western United States extension: How the west was widened: *Annual Review of Earth and Planetary Sciences*, v. 27, p. 417–462.

- Sprinkel, D.A., 1994, Stratigraphic and Time-stratigraphic Cross Sections, a North-south Transect from Near the Uinta Mountain Axis Across the Basin and Range Transition Zone to the Western Margin of the San Rafael Swell, Utah: US Geological Survey.
- Sprinkel, D.A., Doelling, H.H., Kowallis, B.J., Waanders, G., and Kuehne, P.A., 2011, Early results of a study of Middle Jurassic strata in the Sevier fold and thrust belt, Utah: Sprinkel, DA, Yonkee, WA, and Thomas C. Chidsey, J., editors, Sevier thrust belt: northern and central Utah and adjacent area: Utah Geological Association Publication, v. 40, p. 151–172.
- Steen, O., and Anderson, A., 1999, Effects of lithology on geometry and scaling of small faults in Triassic sandstones, East Greenland: *Journal of Structural Geology*, v. 21, p. 1351–1368.
- Stewart, J.H., Poole, F.G., and Wilson, R.F., 1972, Stratigraphy and origin of the Triassic Moenkopi Formation and related strata in the Colorado Plateau region: U.S. Geological Survey Professional Paper 691, 195 p.
- Stockli, D.F., Linn, J.K., Walker, J.D., and Dumitru, T.A., 2001, Miocene unroofing of the Canyon Range during extension along the Sevier Desert Detachment, west central Utah: *Tectonics*, v. 20, p. 289–307.
- Tearpock, D.J. and Bischke, 2003, Applied subsurface geological mapping (2nd edition): New Jersey, Pearson Educations, Inc., 822 p.
- Torabi, A., Fossen, H., and Braathen, A., 2013, Insight into petrophysical properties of deformed sandstone reservoirs: *AAPG Bulletin*, v. 97, p. 619–637, doi: 10.1306/10031212040.
- Tueckmantel, C., Fisher, Q.J., Knipe, R.J., Lickorish, H., and Khalil, S.M., 2010, Fault seal prediction of seismic-scale normal faults in porous sandstone: A case study from the eastern Gulf of Suez rift, Egypt: *Marine and Petroleum Geology*, v. 27, p. 334–350, doi: 10.1016/j.marpetgeo.2009.10.008.
- Tveranger, J., Braathen, A., Skar, T., and Skauge, A., 2005, Centre for Integrated Petroleum Research—Research activities with emphasis on fluid flow in fault zones: *Norwegian Journal of Geology*, v. 85, p. 63–71.
- USGS, 2012, United States Geological Survey quaternary fault and fold database for the United States, accessed Feb 1, 2012, <http://earthquake.usgs.gov/regional/qfaults/>.
- Verlander, J.E., 1995, The Navajo Sandstone: *Geology Today*, v. 11, p. 143–146.
- Virgas, G., Urbanicic, T., and Baig, A., 2013, Stress-strain conditions associated with induced earthquakes, *Seismological Research Letters*, v. 84, p. 375.

- Vrolijk, P., and van der Pluijm, B.A., 1999, Clay gouge: *Journal of Structural Geology*, v. 21, p. 1039–1048.
- Walsh, J.J., and Watterson, J., 1988, Analysis of the relationship between displacements and dimensions of faults: *Journal of Structural Geology*, v. 10, p. 239–247.
- Walsh, J.J., Watterson, J., Bailey, W.R., and Childs, C., 1999, Fault relays, bends and branch-lines: *Journal of Structural Geology*, v. 21, p. 1019–1026.
- Watson, R.T., Meira Filho, L.G., Sanhueza, E., and Janetos, A., 1992, Greenhouse gases: sources and sinks: *Climate Change*, p. 25–46.
- Watts, N.L., 1987, Theoretical aspects of cap-rock and fault seals for single-and two-phase hydrocarbon columns: *Marine and Petroleum Geology*, v. 4, p. 274–307.
- Wesson, R. L., and Nicholson, C., 1987, Earthquake hazard associated with deep well injection: a report to the US Environmental Protection Agency: U.S. Geological Survey.
- White, C.M., Strazisar, B.R., Granite, E.J., Hoffman, J.S., and Pennline, H.W., 2003, Separation and Capture of CO₂ from Large Stationary Sources and Sequestration in Geological Formations—Coalbeds and Deep Saline Aquifers: *Journal of the Air & Waste Management Association*, v. 53, p. 645–715, doi: 10.1080/10473289.2003.10466206.
- Wibberley, C.A.J., Yielding, G., and Di Toro, G., 2008, Recent advances in the understanding of fault zone internal structure: a review: *Geological Society, London, Special Publications*, v. 299, p. 5–33, doi: 10.1144/SP299.2.
- Wilkins, S.J., Gross, M.R., Wacker, M., Eyal, Y., and Engelder, T., 2001, Faulted joints: kinematics, displacement-length scaling relations and criteria for their identification: *Journal of Structural Geology*, v. 23, p. 315–327.
- Wong, I.G., and Humphrey, J.R., 1989, Contemporary seismicity, faulting, and the state of stress in the Colorado Plateau: *Geological Society of America Bulletin*, v. 101, p. 1127–1146.
- Yielding, G., Freeman, B., and Needham, D.T., 1997, Quantitative fault seal prediction: *AAPG bulletin*, v. 81, p. 897–917.
- Zhang, Y., Oldenburg, C.M., and Finsterle, S., 2009, Percolation-theory and fuzzy rule-based probability estimation of fault leakage at geologic carbon sequestration sites: *Environmental Earth Sciences*, v. 59, p. 1447–1459, doi: 10.1007/s12665-009-0131-4.

Zhou, Q., Birkholzer, J.T., Mehnert, E., Lin, Y.-F., and Zhang, K., 2009, Modeling Basin- and Plume-Scale Processes of CO₂ Storage for Full-Scale Deployment: Ground Water, v. 48, p. 494–514, doi: 10.1111/j.1745-6584.2009.00657.x.

Zoback, M.D., and Gorelick, S.M., 2012, Earthquake triggering and large-scale geologic storage of carbon dioxide: Proceedings of the National Academy of Sciences, v. 109, p. 10164–10168, doi: 10.1073/pnas.1202473109.

APPENDICES

Appendix A: Borehole Data

Select borehole data compiled and organized from Utah Division Oil, Gas and Mining (www.oilgas.ogm.utah.gov) are available via the Utah State University Digital Commons website within the Selected Works of David J. Richey (http://works.bepress.com/david_richey/).

The data found here include API well numbers, names of all wells used, well datum as defined by the elevation above sea level measured at the Kelly Bushing on the drilling floor, and the depth to various formation tops encountered during drilling measured in drilling depth.

Appendix B: Geophysical Data

Select geophysical data collected and processed during this thesis are available via the Utah State University Digital Commons website within the Selected Works of David J. Richey (http://works.bepress.com/david_richey/).

A description of the geophysical methods used, the results and raw data, and some interpretations are provided in this appendix.